185(2), 2021

COMBUSTION ENGINES

INSTYTUT TECHNICZNY WOJSK LOTNICZYCH

ul. Księcia Bolesława 6, 01-494 Warszawa, skr. poczt. 96
tel.: 261 851 300; faks: 261 851 313
www.itwl.pl e-mail: poczta@itwl.pl

SYSTEM DIAGNOSTYKI TRIBOLOGICZNEJ

Pobieranie próbek oleju z silników, przekładni, skrzynek napędu, instalacji hydraulicznych	**Badania**	**Przekazanie informacji diagnostycznej**	
Użytkownik	Akredytowane laboratorium w ITWL	ITWL	Użytkownik

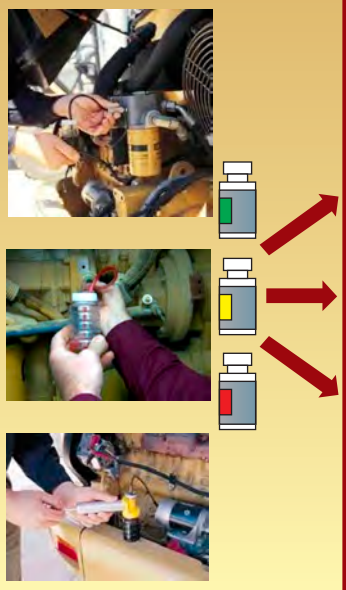

Analiza danych

Baza danych

Diagnoza

System Diagnostyki Tribologicznej (SDT), opracowany w Instytucie Technicznym Wojsk Lotniczych, przeznaczony jest do wspierania eksploatacji obiektów technicznych.

Na podstawie wyników badań próbek oleju pobranych z układów tribologicznych prowadzi się ocenę i prognozowanie stanu technicznego obiektów technicznych (statki powietrzne, pojazdy mechaniczne, statki wodne, maszyny robocze i inne).

PCA Polskie Centrum Akredytacji BADANIA AB 138

Akredytacja OiB JB 9/MON/2017

INSTYTUT TECHNICZNY WOJSK LOTNICZYCH
ZAKŁAD SILNIKÓW LOTNICZYCH
Akredytowane laboratorium:
Laboratorium Diagnostyki Systemów Tribologicznych

PTNSS Supporting Members
Członkowie wspierający PTNSS

BOSMAL Automotive Research and Development Institute Ltd
Instytut Badań i Rozwoju Motoryzacji BOSMAL Sp. z o.o

Motor Transport Institute
Instytut Transportu Samochodowego

Institute of Aviation
Sieć Badawcza Łukasiewicz – Instytut Lotnictwa

Automotive Industry Institute
Sieć Badawcza Łukasiewicz – Przemysłowy Instytut Motoryzacji

The Rail Vehicles Institute TABOR
Sieć Badawcza Łukasiewicz – Instytut Pojazdów Szynowych TABOR

Industrial Institute of Agricultural Engineering
Sieć Badawcza Łukasiewicz – Przemysłowy Instytut Maszyn Rolniczych

AVL List GmbH

Solaris Bus & Coach S.A.

Air Force Institute of Technology
Instytut Techniczny Wojsk Lotniczych

Military Institute of Armoured & Automotive Technology
Wojskowy Instytut Techniki Pancernej i Samochodowej

Toyota Motor Poland Ltd. Sp. z o.o.

RADWAG Balances and Scales
RADWAG Wagi Elektroniczne

COMBUSTION ENGINES

A Scientific Magazine

2021, 185(2)

Year LX

PL ISSN 2300-9896
PL eISSN 2658-1442

Editor:

Polish Scientific Society of Combustion Engines
60-965 Poznan, pl. M. Skłodowskiej-Curie 5, Poland
tel.: +48 61 6475966, fax: +48 61 6652204
E-mail: sekretariat@ptnss.pl
WebSite: http://www.ptnss.pl
Papers available on-line: http://combustion-engines.eu

Contents

Declaration of the original version
The original version of the Combustion Engines journal is the printed version.

Editorial:
Institute of Combustion Engines and Powertrains
Poznan University of Technology
60-965 Poznan, Piotrowo 3 Street
tel.: +48 61 2244505, +48 61 2244502
E-mail: papers@ptnss.pl

Editor
Polish Scientific Society of Combustion Engines
60-965 Poznan, pl. M. Sklodowskiej-Curie 5, Poland
tel.: +48 61 6475966, fax: +48 61 6652204
E-mail: sekretariat@ptnss.pl
WebSite: http://www.ptnss.pl

Subscriptions
Send subscription requests to the Publisher's address.
Cost of a single issue PLN 40.

Preparation for print
ARS NOVA Publishing House
60-782 Poznan, ul. Grunwaldzka 17/10A

Circulation: 120 copies

Printing and binding

Zakład Poligraficzny Moś i Łuczak, sp. j.,
Poznań, ul. Piwna 1

The journal is registered in the Polish technical journals content database – **BAZTECH** www.baztech.icm.edu.pl

The journal is listed in the international database **IC Journal Master List** – **Index Copernicus** www.indexcopernicus.com

Papers published in the ***Combustion Engines*** quarterly receive 20 points as stated by the Notification of the Minister of Science and Higher Education dated 31 July 2019.

Cover
I – Jaguar F-PACE SVR 5.0 Liter V8 Engine
(*fot. media.jaguar.com*); background (abstract-cool-orange-texture – *www.123freevectors.com*)
IV – McLaren Artura axial flux electric motor
(*fot. www.apex.one*)

Article citation info:
WOODBURN, J. Emissions of reactive nitrogen compounds (RNCs) from two vehicles with turbocharged spark ignition engines over cold start driving cycles. *Combustion Engines*. 2021, **185**(2), 3-9. https://doi.org/10.19206/CE-135811

Joseph WOODBURN

Emissions of reactive nitrogen compounds (RNCs) from two vehicles with turbocharged spark ignition engines over cold start driving cycles

This paper reviews the emissions of reactive nitrogen compounds (RNCs) from modern vehicles fitted with spark ignition engines and three-way catalysts. Specific aspects of the pollutants involved – and their formation – are discussed. Cold start driving cycles are scenarios under which emissions of all four RNCs can be significant; the mechanisms behind emissions trends are explored. Experimental data obtained from two vehicles tested over two different cold start driving cycles are presented and analysed. The use of gravimetric and molar metrics are explored. Ammonia, a species which is currently not regulated for passenger cars in any automotive market, is identified as forming the majority of the RNC emissions over the entire driving cycle. While ammonia emissions are strongly linked to aftertreatment system warmup and periods of high load, significant ammonia emissions were also measured under certain hot-running, low load conditions, and even at idle. For the majority of the duration of the test procedures employed, the RNC profile was dominated by ammonia, which accounted for between 69% and 86% of measured RNCs in the exhaust gas. Emissions are compared to the available legislative precedents (i.e. emissions limits currently in force in various jurisdictions). Finally, possibilities for control of exhaust emissions of currently unregulated RNCs are briefly discussed.

Key words: *exhaust emissions, reactive nitrogen compounds, NO_x, ammonia, nitrous oxide*

1. Introduction

The formation of pollutants is an inevitable consequence of combustion, with the relevant parameters being which pollutants are formed and at what levels. Linked to the working cycle, fuel type, etc, spark ignition engines have significant levels of gaseous pollutants in their exhaust gas, a fact which has led to the imposition of emissions limits for the most problematic pollutant types. While a range of measures has been taken to reduce emissions from vehicular powertrains featuring such engines, the single most important solution for emissions control in this context is the three-way catalyst (TWC). This device, use of which was first forced in the 1970s in the USA, remains in near-universal use, including in some SI engines used in sectors other than light duty road transport (passenger cars). Designs and specifications have undergone continuous revision over the past few decades, but the basic concept and functionality remains unchanged. See [14] for a summary of the history of TWCs and a technical overview of their functionalities.

The appellation 'three-way' results from the functionality which consists of oxidation of both hydrocarbons and carbon monoxide, as well as reduction of NO_x ($NO + NO_2$), which in the case of SI engines consists mostly of NO [3], [14], thus simplifying to:

$$2\ NO \rightarrow N_2 + O_2 \tag{1}$$

Note that reaction (1) is empirical in nature and somewhat idealised; significantly, it does not involve hydrogen (nor water), whereas those species play an active and complex role in TWC functionality. Interactions between CO and NO are also mentioned in the literature, but such details are beyond the scope of this paper.

Unsurprisingly, the efficacy of reactions to eliminate pollutants (including (1)) is strongly dependent not only on the temperature, but also on the composition of the exhaust gas including the oxygen level. Since exhaust gas results from the interaction between dosed fuel and ambient air, the overall composition changes as the oxygen level changes – as the oxygen level falls, the level of CO increases. The ratio between CO and H_2 is normally rather static (at least for a given fuel type), taking an approximate ratio of 3:1. As the aforementioned parameters are strongly controlled by the ratio of air to fuel, that parameter is used to describe the composition of the exhaust gas, most conveniently normalised to stoichiometry for the fuel type (lambda; λ).

Under certain conditions, a TWC can catalytically facilitate reactions which appear to have the same effect as (1) – in such reactions, the concentration of NO_x is significantly reduced across the TWC, but the final nitrogenous product exiting the TWC is not (entirely) N_2. The two main reactions of this type are:

$$NO + 5/2\ H_2 \rightarrow NH_3 + H_2O \tag{2}$$

and

$$2\ NO + H_2 \rightarrow N_2O + H_2O \tag{3}$$

With the latter obviously having a lower stoichiometric requirement per mole of NO (i.e. requiring less hydrogen).

In addition to the availability of reagents, temperature exerts a strong influence on the catalytic promotion of reactions occurring in a TWC, particularly in the case of reactions (1)–(3).

2. Background

The combustion process generates significant NO_x, which, as mentioned previously, is dominated by NO. Other RNCs are present only at trace levels in the exhaust gas leaving the cylinder [3]. The behaviour and ultimate fate of these NO molecules is complex. For every molecule of NO entering the TWC, there are 6 potential fates:

1. Not engaging in any reaction, exiting the TWC as NO_x (this definition would include the conversion of NO to NO_2, or vice-versa)
2. Undergoing reaction (1), forming N_2
3. Undergoing reaction (2), forming NH_3
4. Undergoing reaction (3), forming N_2O
5. Undergoing some other reaction, producing a minor nitrogen-containing product (such as HNCO)

Received 29 March 2021; Received in revised form 11 April 2021; Accepted 15 April 2021
Available online 22 April 2021

6. Undergoing some other process, involving intermediate steps and species, but which has the same ultimate effect as one of points 1–5 (above)

For the sake of simplicity, points 5 and 6 may be ignored in most contexts. The probability of points 1, 2, 3 or 4 occurring varies strongly with TWC operating conditions, especially λ and temperature (and therefore with powertrain operating conditions) [3]. The degree to which a given product dominates the output is known as the selectivity. Obviously, the most desirable outcome is for NO to be entirely converted to N_2 (process 2; reaction (1)); however, post-TWC exhaust gas contains non-negligible quantities of reactive nitrogen (non-N_2) [3]. As the engine-out concentration of NO is generally high for SI engines under the majority of operating conditions, especially those without EGR (concentration often on the order of $1–3\times10^3$ ppm), even low selectivity towards a given process/species (e.g. 10%) can lead to significant post-TWC concentrations of nitrogen in forms other than N_2, i.e. reactive nitrogen compounds (RNCs).

Nitrogen is self-evidently not harmful and is not measured in automotive contexts. Of the RNCs NO, NO_2, NH_3 and N_2O, only the first two compounds are regulated in the European Union (together, as NO_x). NH_3 is regulated for heavy-duty vehicles in the EU and South Korea (using a very simple mean concentration-based limit); N_2O, being a potent greenhouse gas, is regulated in the USA and China, but not in the EU. Growing interest in automotive emissions of NH_3, N_2O and even NO_2 have led to calls for those compounds to be included as regulated pollutants in the next round of EU emissions legislation, with gravimetric limits likely to apply to both light- and heavy-duty road vehicles, regardless of engine or fuel type.

In this context, simultaneous quantification of emissions of the four RNCs is an important aspect of research into exhaust emissions. Such a measurement can be achieved by two main classes of analyser: a laser-based RNC analyser, or Fourier transform infra-red (FTIR) analysis. As described in [1], BOSMAL's exhaust emissions laboratory no. 2 is equipped with the former, permitting such measurements to be made.

3. Experimental

3.1. Test vehicles and test conditions for laboratory characterisation of RNC emissions

Two vehicles representing the latest technology for non-hybrid SI powertrains were tested. Details of the vehicles and their powertrains are given in Table 1.

Table 1. Key characteristics of the test vehicles

Aspect	Vehicle 1	Vehicle 2
Vehicle type	Passenger car	
Engine type	Turbocharged, direct-injection, spark-ignition	
Approx. engine displacement	1.0–1.5 dm^3	
Number of cylinders	4	
Approx. vehicle power:mass ratio	75 W/kg	
Aftertreatment system type	Integrated TWC on GPF (so-called 4-way catalyst), close-coupled mounting position	
Emissions standard	Euro 6d-TEMP	
Approx. mileage at start of testing	60,000 km	

The test vehicles both featured the same downsized turbocharged engine. As the engines were identical, it was assumed that the composition of the TWCs were also identical. Vehicle 1's bodywork gave it a slightly higher mass than vehicle 2 (although the difference was only some 5%). The power:mass ratio was thus slightly higher for vehicle 2. Both vehicles met the Euro 6d-TEMP standard, were in sound mechanical condition and showed no OBD errors before (or after) testing. Testing was conducted on the two vehicles at the same nominal mileage stage, corresponding to 37.5% of the mileage required for demonstration of durability of emissions control systems in EU legislation (160,000 km). During the aforementioned mileage accumulation, which occurred prior to testing and was not subject to emissions measurements, the usage profiles (driving conditions) of the two vehicles were not identical, but generally similar, consisting of both urban and extra-urban driving occurring under real-world conditions.

The vehicles were tested on a chassis dynamometer in an exhaust emissions laboratory meeting the demands of the latest EU legislation [1, 2]. As mentioned previously, a dedicated, laser-based RNC analyser was used for simultaneous measurement of concentrations of NO, NO_2, NH_3 and N_2O in the raw (undiluted) exhaust gas. Quantification from raw exhaust gas is essential for NH_3 measurements. Gravimetric emissions were calculated based on these concentrations and the flow rate corrected for the instantaneous dilution ratio.

The well-known WLTP and NEDC test procedures were used for testing. In all cases, two tests of each type were performed on each vehicle (n = 2), with the mean value obtained taken for further analysis. The WLTP is the legislative procedure (and indeed driving cycle – WLTC) applicable to the test vehicles, while the NEDC is the previous EU legislative cycle. The appropriate road load for the test vehicles was applied, according to the legislative procedures associated with the two cycles. In the case of WLTP testing, the procedure leads to a significantly higher inertia than for the NEDC, as well as increased road load. Commentary on the differences (and similarities) in the two test procedures and the resulting impact on regulated emissions and fuel consumption are available elsewhere [4, 11]. For the purposes of this paper, it suffices to highlight two similarities:

- both cycles commence from a cold start, with the first acceleration from rest occurring approximately 10 seconds after engine start-up,
- the first phase of each cycle consists of urban type driving and the distance covered by the first phase of each cycle is reasonably similar (WLTC Low = 3.1 km / NEDC UDC = 4 km);

and to identify three key differences:

- total distance covered – WLTC = 23.3 km / NEDC = 11 km, i.e. a difference of 212%;
- the distance-specific energy demand for the two cycles, which in the case of the vehicles used in this study was some 25% higher in the case of the WLTC;
- the NEDC mandates fixed gear usage, according to a one-size-fits-all approach, whereas for the WLTP gear usage must be calculated based on required power at the

wheel and available engine power, which has the overall effect of generally specifying higher gears for a given level of demanded wheel power, thereby somewhat reducing engine speeds and increasing engine load (compared to the NEDC). The period of cruise at 50 km/h in 3rd gear which occurs 4 times during the NEDC is a prime example of this.

Standard, market-available EU petrol was used for testing – the same fuel for both vehicles, for all tests. The fuel was certified to meet the demands of European Norm EN228, was of nominal RON 95, had a nominal ethanol content of 5% (verified value: 4.9%) and a sulphur content of 4.5 mg/kg.

3.2. Results and discussion

Regulated exhaust emissions applicable to the vehicle engine type (THC, NMHC, CO, NO_x, particulates) were measured according to the EU legislative method. Results are not presented here, but were used to assess test-to-test repeatability. All applicable emissions limits (Euro 6) were met, in all cases. The correlation between the legislative (bag) NO_x result and the 'virtual NO_x' (i.e. NO + NO_2) result obtained from the RNC analyser was generally good and judged to be acceptable for all tests. RNC test results from the two vehicles are presented and discussed below. Results from vehicle 1 during the WLTC are shown in Fig. 1, by the 4 phases that make up the cycle (Low, Medium, High, Extra-High, which occur in that order) and for the entire cycle.

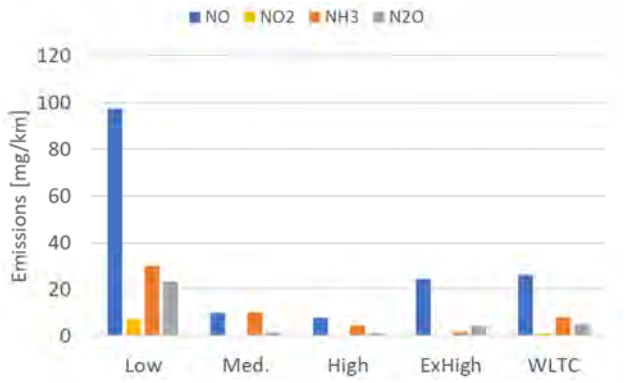

Fig. 1. RNC emissions from vehicle 1, tested over the WLTC, by phase and for the entire cycle

As is evident from Figure 1, over the entire cycle NO emissions dominate for this vehicle, followed by NH_3, N_2O and finally NO_2. The mass of NO emitted is the highest of all RNCs for all phases, except for the 2nd phase (Medium), where emissions of NO and NH_3 are essentially identical. As the range of values is very wide (covering over 2 orders of magnitude), the same data are presented in Fig. 2, on a scale which excludes values > 15 mg/km.

For all four RNCs, emissions were highest during the Low phase. Results from vehicle 1 during the NEDC are shown in Fig. 3, by the two phases that make up the cycle (UDC, EUDC, which occur in that order) and for the entire cycle.

Here emissions were generally numerically lower than over the WLTC. NO dominated during the UDC and NH_3 dominated during the EUDC (the only species with emissions > 5 mg/km); for results from the entire cycle, NO and NH_3 were at essentially identical levels, followed by N_2O and finally NO_2.

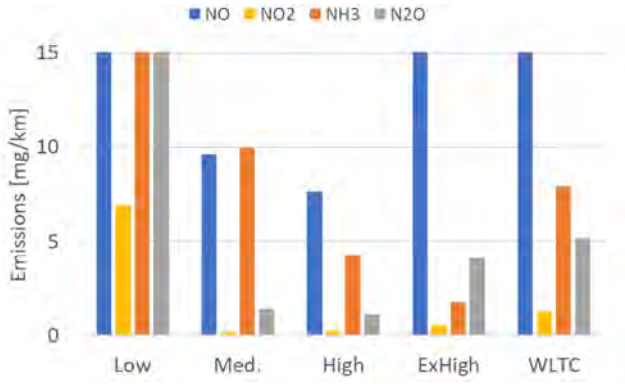

Fig. 2. Lower range of RNC emissions (< 15 mg/km) from vehicle 1, tested over the WLTC, by phase and for the entire cycle

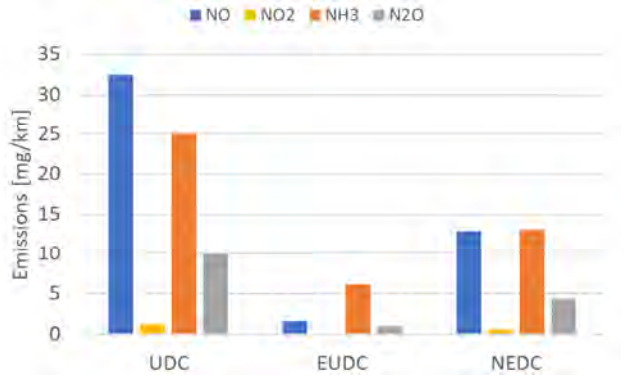

Fig. 3. RNC emissions from vehicle 1, tested over the NEDC, by phase and for the entire cycle

As with results from the WLTC, the initial (cold start, urban speed range) phase was associated with the highest distance-specific emissions, for all four species. Results from vehicle 2 during the WLTC are shown in Fig. 4.

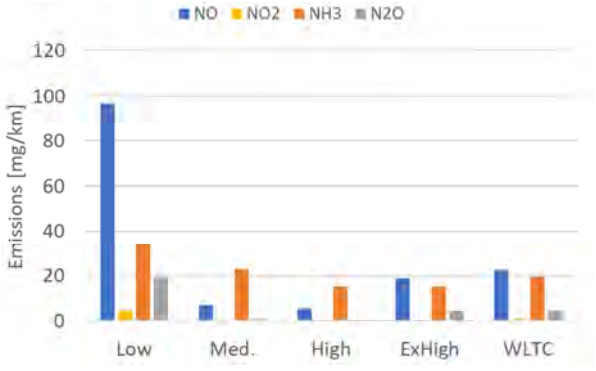

Fig. 4. RNC emissions from vehicle 2, tested over the WLTC, by phase and for the entire cycle

Emissions were similar to those from vehicle 1, with the notable exception that NH_3 was at a level much closer to emissions of NO over the entire cycle, with NH_3 > NO during the 2nd and 3rd phases. Emissions of all compounds were highest during the 1st phase.

Results from vehicle 2 during the NEDC are shown in Fig. 5.

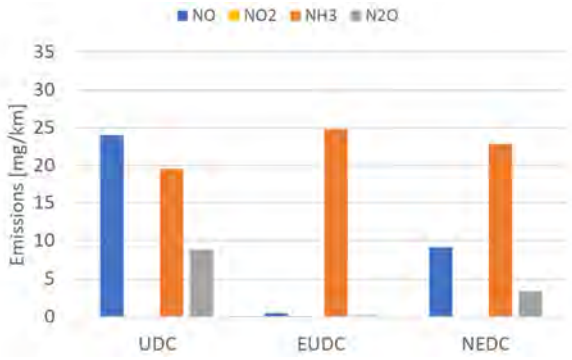

Fig. 5. RNC emissions from vehicle 2, tested over the NEDC, by phase and for the entire cycle

As is immediately apparent from Fig. 5, the behaviour in this case was quantitatively and qualitatively different from the other results (Figs 1–4). Over the entire cycle, emissions of NH_3 were highest, being more than twice those of NO. Emissions of NO_2 were extremely low (barely detectable) during either phase, with emissions over the entire cycle taking a value < 1 mg/km. During the EUDC phase, emissions of NO, NO_2 and N_2O were all extremely low, with the RNC profile consisting almost exclusively of NH_3; emissions of that compound were at a slightly higher level than during the UDC phase, in strong contrast to results from vehicle 1 and in contrast to results from vehicle 2 obtained over the WLTC (Fig. 4).

The overall magnitude of NH_3 emissions generally agreed with other studies conducted on Euro 5/6 vehicles [15, 16]. The overall level of N_2O emissions was in line with most reported emissions factors obtained under laboratory conditions (see [10]), although the fact that results from vehicle 1 (WLTC) were so close to the US limit is perhaps somewhat surprising, given the displacement of the engine (< 1.5 dm^3) and the reasonably modest driving energy demand resulting from the vehicle's mass (< 1500 kg). Agreement between the results obtained from the two test vehicles were generally reasonably good, but could be further investigated. In particular, the NH_3 emissions occurring over the EUDC phase of the NEDC stood out as showing poor agreement (and were surprisingly high in the case of vehicle 2) a point which could be further investigated. Similarly, further testing of vehicles of this type at higher mileages (e.g. 120,000–160,000 km) is recommended.

Instantaneous concentration traces are available for measurements of this type, for which a continuous stream of exhaust gas is sampled, in contrast to batch analysis (i.e. bag samples – the light-duty legislative test method). Figure 6 shows the RNC concentrations for vehicle 1, tested over the WLTC; NO_2 is omitted for the sake of clarity, which is justifiable due to the very low measured concentrations of that species.

The very high values taken by NO at the beginning of the cold start test result from that species, which is generated in-cylinder in large quantities, simply passing through the TWC. Figure 7 shows the same data in the range 0–600 seconds and excluding concentrations > 400 ppm.

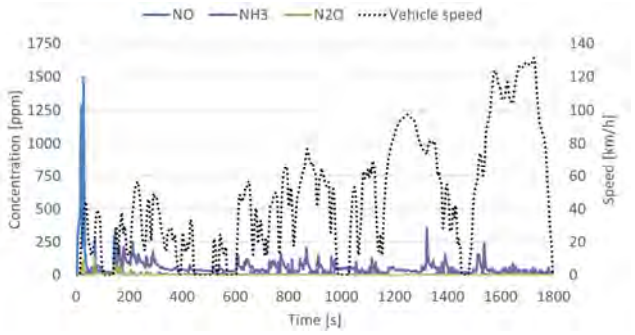

Fig. 6. RNC concentrations from vehicle 1, tested over the WLTC (NO_2 not shown)

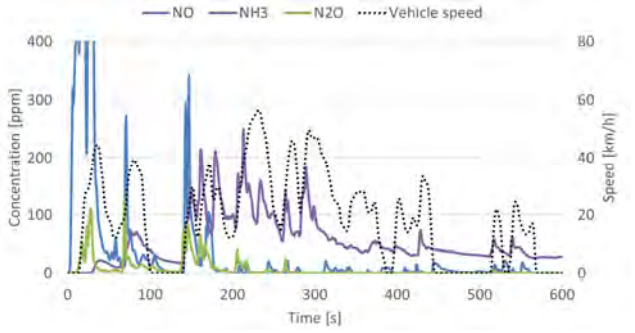

Fig. 7. RNC concentrations from vehicle 1, shown for the first 600 s of the WLTC (NO_2 not shown; NO concentrations > 400 ppm not shown)

As Figures 6 and 7 show, following the initial surge of NO, values begin to fall as the TWC approaches its light off temperature and begins to convert NO. For this vehicle, during the 0–200 second period of the cycle the N_2O concentration trace corresponded quite closely to that of NO (but taking lower values). Production (and release) of N_2O appeared to start early, at around 15 seconds (during the first acceleration from rest), but took very low values from around 250 seconds onwards. NH_3 began to appear at around 30 seconds, but took low values until around 150 seconds, that being the point where NO and N_2O values fell sharply. For the entire period 160–600 seconds, NH_3 was the dominant RNC in the exhaust. Following almost 10 minutes' engine operation (approaching 600 seconds), brief surges of NO and N_2O continued to occur sporadically, as a result of the dynamics of the speed trace (Fig. 8). As shown in Fig. 8, the quasi-stabilised (almost flat) concentration trace for the period 570–600 seconds (during idling) was at a level of around 28 ppm; during that period all other RNCs had concentrations < 1 ppm.

As can be seen in Figs 7 and 8, the NH_3 (and, to a much lower extent, N_2O) concentrations increase during accelerations, an effect reported in virtually every study on NH_3 emissions from vehicles of this type. This is largely due to the use of a somewhat richer air-fuel mixture (with lower λ values), which is well known to increase the efficiency of the elimination of NO_x [14]. However, such surges of NH_3 emission are limited somewhat by gear changes, which cause a decrease in NH_3/N_2O and a momentary increase in NO. The behaviour of the turbocharger may also be a relevant parameter here, especially if scavenging is used, which is known to be linked to NO_x breakthrough in certain cases. Despite this, once NH_3 production has started in earnest

(from around 150 s in this example – most probably linked to the onset of the water-gas shift reaction, which plays a very important role in NH_3 formation [16]), NH_3 remains at significant levels during deceleration events and indeed at idle. During fuel cut-off, NH_3 production should obviously be very limited (among other reasons, NH_3 formation is strongly inhibited by O_2); yet NH_3 concentrations are not observed to fall to zero (or even near-zero) levels (see Fig. 8), unlike for NO and N_2O, concentrations of which rather rapidly return to near-zero values as the conditions within the TWC no longer favour their emission. The response time of the RNC analyser used conforms to the EU heavy duty type approval requirement (analyser rise time < 5 s [19]). Assuming that the impact of response time of the analyser is limited, at least some of the observed behaviour may be attributed to outgassing of NH_3 from metal surfaces which act as temporary NH_3 storage reservoirs and from liquid water which condenses in the exhaust line following a cold start. Ammonia is frequently described as a 'sticky' molecule which readily forms a surface layer of adsorbed molecules on metals such as stainless steel; this is not the case for NO, NO_2, or N_2O. The aforementioned process can accumulate appreciable quantities of adsorbed NH_3, but it is emphatically reversable. As the temperature of the exhaust line increases, the favourability of NH_3 release from condensed water and metal surfaces increases. After some time, no liquid water will remain in the exhaust line; this effect is determined not only by the temperature of the exhaust gas, but also by the exhaust gas flow rate, with a small influence also exerted by the manner in which the vehicle is cooled in the laboratory (wind speed fan characteristics) and overall powertrain design. Ambient temperature is a further factor of obvious relevance, but was not a variable in this study. The aforementioned processes and resulting effects are by nature chaotic and unpredictable (even for a given vehicle subjected to a given test procedure at a given temperature) and account for a significant proportion of the inherent variability and generally low repeatability of NH_3 measurements.

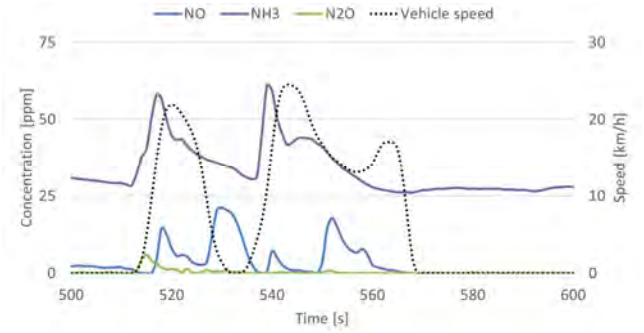

Fig. 8. RNC concentrations from vehicle 1, shown for the period 500–600 s of the WLTC (NO_2 excluded for clarity and due to very low concentrations)

The only RNCs subject to legislative limits in the EU are NO and NO_2 (limited together as NO_x, limit for light-duty vehicles with SI engines: 60 mg/km). This limit was met it all cases, by a wide margin: emissions from both vehicles were < 50% of the limit over the WLTC and < 25% over the NEDC. The contribution of NO_2 was near-negligible (very low in all cases); the fact that NO_2 takes low values (sometimes statistically indistinguishable from zero for hot running driving cycle phases) makes the NO:NO_2 ratio highly variable and of limited interest. While the cold start phases of both driving cycles were dominated by emissions of NO (and therefore NO_x) in all cases, over the entire test cycles employed, emissions of NH_3 were greater than (or broadly equivalent to) emissions of NO in three out of the four cases examined – only in the case of vehicle 1 on the WLTC cycle was the RNC profile dominated by NO, with NH_3 a distant second. The US N_2O limit of 6.2 mg/km was met in all cases, although emissions from vehicle 1 over the WLTC were very close to this level (5.9 mg/km). The other reference point for N_2O, the Chinese limit (20 mg/km) was thus obviously met by a wide margin. For NH_3, the only direct legislative precedent is the mean concentration-based limit applicable to heavy-duty vehicles. This mean concentration of 10 ppm was exceeded in all tests, by a large margin: the lowest mean NH_3 concentration measured during any test was some 35 ppm; instantaneous NH_3 concentrations took maximum values of several hundred ppm. Despite the very different processes behind emissions of the various RNCs, the cold start phase clearly caused the highest distance-specific emissions. Only in a single case were emissions of any RNC greater over a hot running phase of the driving cycle: NH_3 during the EUDC phase of the NEDC, for vehicle 2.

As the density of NH_3 is low in comparison to the density of NO (76% difference), a given mass of NH_3 contains significantly more molecules than the same mass of NO. Thus, on a molar basis NH_3 often dominates the RNC profile, even where gravimetric emissions of NO are substantially higher than NH_3. Table 2 shows the proportion of RNCs occurring as NH_3 over the entire test cycles, on a molar basis.

Table 2. Molar NH_3:RNC ratio – proportion of RNCs occurring as NH_3, on a molar basis

Vehicle, test cycle	Molar NH_3/RNC ratio [-]
1, WLTC	0.69
1, NEDC	0.86
2, WLTC	0.78
2, NEDC	0.83

As all the values in Table 2 significantly exceed a value of 0.50, it can be stated that NH_3 dominated the RNC profile on a molar basis, in all four cases. This is also evident from a plot of the real-time value of the NH_3:RNC proportion during a given test, as shown in Fig. 9. The finding that NH_3 emissions could be equivalent to – or even greater than – NO, especially on a non-gravimetric (i.e. molar) basis, has been reported previously [18] and supports the general observation that in the case of vehicles meeting stringent NO_x emissions limits, NH_3 is the dominant RNC in the exhaust gas during hot running operation (see [17] and references therein).

After around 100 seconds' engine operation following cold start, the parameter begins to take values > 0.5; it thereafter mostly remains at higher values (> 0.6), with some exceptions, where it very briefly falls to values as low as 0.2. These low values are caused by periods of elevated NO emissions, mainly associated with the sudden transition in engine load caused by gear changes. However, the rela-

tionship between NH_3:RNC and vehicle speed and demand for engine power is complex and multi-faceted – consider, for example, the two periods marked with the dotted red line in Figure 9. These periods consist of broadly similar hot running driving conditions, albeit with a higher speed in the case of the second period, yet are characterised by very different behaviour for the value of NH_3:RNC. As higher speed (and thus load) should be associated with somewhat lower λ values (and thus increased NH_3 production should be expected) this apparent contradiction might be at least somewhat attributable to the temperature [5] and space velocity of the exhaust gas within the TWC.

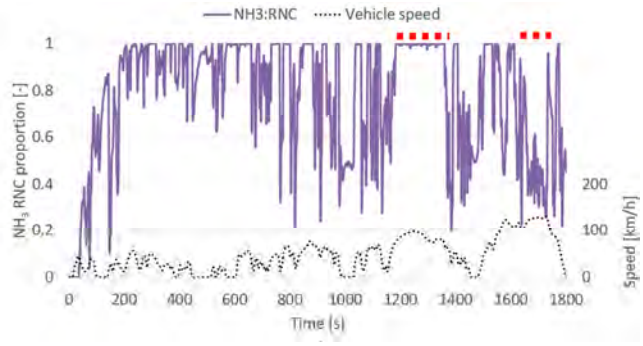

Fig. 9. NH_3:RNC ratio for vehicle 2, tested over the WLTC. Refer to the text for an explanation of the significance of the dotted red lines

4. Summary and overall conclusions

Characterisation of the RNC emissions of two vehicles with downsized, turbocharged SI engines was carried out under laboratory conditions, using two cold start driving cycles with differing characteristics. RNC emissions behaviour was, for the most part, quite similar for the two vehicles and emissions were broadly in line with the findings of other, similar studies. The EU NO_x limit was easily met; the US N_2O limit was met in all cases, but the EU NH_3 concentration limit (not applicable to this vehicle type) was exceeded in all cases. The RNC profile was dominated by two of the four species: NO and NH_3. Gravimetric NH_3 emissions can be at a higher level than gravimetric NO emissions, but are for the most part broadly comparable. However, gravimetric emissions are also a function of the density of the compound, which is relatively low in the case of NH_3. On a molar basis, NH_3 clearly dominates the RNC profile for the majority of the test, as reflected in the value of NH_3:RNC – which took values between 0.69 and 0.86 of measured RNCs in the exhaust gas. Cold start urban operation is associated with significant RNC emissions – firstly NO dominates, then NO and N_2O co-exist (but with significantly more of the former), then the commencement of NH_3 production causes that species to dominate (overall and generally speaking). This fact has significant implications for urban air quality, especially in light of the short distances often covered in passenger cars, a concern also reviewed in other studies (see [7] for a recent example). Hot running driving is, in most (but not all) cases, associated with lower distance-specific RNC emissions. While the NEDC features an undemanding speed trace leading to lower intrinsic RNC emissions, this is counteracted to a degree by the lower number of kilometres covered, meaning that distance-specific RNC emissions are in some cases comparable to those obtained from the WLTC.

The tendency to form NH_3 under a range of driving conditions (including periods of low power demand and even idle) is a disadvantage of certain powertrain designs and TWC configurations. While NH_3 (and indeed N_2O) remain unregulated in the EU, there is little incentive for manufacturers to optimise emissions control systems (and indeed entire powertrains) to limit their formation and release into the environment. Potential options to limit the formation of NH_3 include limiting use of enrichment (i.e. adopting 'flat' λ1, or even partially lean combustion (λ > 1) [12]), as well as the addition of an aftertreatment system component to deal with NH_3, concepts for which are shown in Figures 10 and 11.

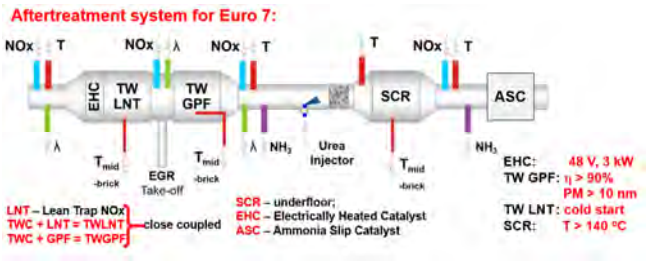

Fig. 10. Aftertreatment system concept to meet future emissions standards (Euro 7), including an ASC for NH_3 control [12]

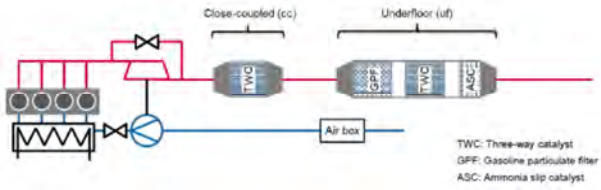

Fig. 11. Aftertreatment system concept to meet future emissions standards (Euro 7), including an ASC for NH_3 control [6]

Ammonia slip catalysts (ASC) suitable for use with the exhaust generated by λ1 SI engines are undergoing testing and development [6]. Passive SCR systems allowing storage of NH_3 for later use in reactions eliminating post-TWC NO_x have also been mentioned as options for simultaneous NO_x/NH_3 reductions [9, 13]. It is believed that no equivalent options exist for direct, targeted control of N_2O; the fact that new light duty vehicles sold in the USA must meet a limit of 6.2 mg/km shows that optimisation of TWCs is able to reduce emissions to below that level. For species associated with cold start and the gradual warmup of the TWC, electrical catalyst heating [8, 12], might prove a solution with many advantages regarding control of RNCs (and pollutants in general [8]).

Nomenclature

λ	lambda; the normalised air:fuel ratio
ASC	ammonia slip catalyst
CO	carbon monoxide
CC	close-coupled

EGR	exhaust gas recirculation
EHC	electrically heated catalyst
EU	European Union
EUDC	extra-urban driving cycle (part of the NEDC)
GPF	gasoline particulate filter
H_2	hydrogen (diatomic molecule)
HNCO	isocyanic acid
LNT	lean NO_x trap
N_2O	nitrous oxide
NEDC	New European Driving Cycle
N_2	nitrogen (diatomic molecule)
NH_3	ammonia
NMHC	non-methane hydrocarbons
NO	nitrogen monoxide
NO_2	nitrogen dioxide
NO_x	oxides of nitrogen (NO + NO_2)
O_2	oxygen (diatomic molecule)
OBD	on-board diagnostics
RNC	reactive nitrogen compounds (NO, NO_2, NH_3, N_2O)
RON	research octane number
SCR	selective catalytic reduction
SI	spark ignition
T	temperature
THC	total hydrocarbons
TWC	three-way catalyst
TWGPF	three-way gasoline particulate filter
TWLNT	three-way lean NO_x trap
UDC	urban driving cycle (part of the NEDC)
UF	under-floor
US(A)	United States (of America)
WLTC	Worldwide Harmonised Light Vehicles Test Cycles
WLTP	Worldwide Harmonised Light Vehicles Test Procedure

Bibliography

1. BIELACZYC, P., KLIMKIEWICZ, D., WOODBURN, J. et al. Exhaust emission testing methods – BOSMAL's legislative and development emission testing laboratories. *Combustion Engines.* 2019, **178**(3), 88-98. https://doi.org/10.19206/CE-2019-316
2. BIELACZYC, P., SZCZOTKA, A., PAJDOWSKI, P. et al. Development of automotive emissions testing equipment and test methods in response to legislative, technical and commercial requirements. *Combustion Engines.* 2013, **152**(1).
3. BIELACZYC, P., SZCZOTKA, A., WOODBURN, J. An overview of emissions of reactive nitrogen compounds from modern light duty vehicles featuring SI engines. *Combustion Engines.* 2014, **159**(4), 48-53.
4. BIELACZYC, P., WOODBURN, J., SZCZOTKA, A. Exhaust emissions of gaseous and solid pollutants measured over the NEDC, FTP-75 and WLTC chassis dynamometer driving cycles. *SAE Technical Paper* 2016-01-1008. 2016. https://doi.org/10.4271/2016-01-1008
5. BOND, G.C., WEBB, G., HARRISON, B. et al. Catalysis of reactions involving the reduction of decomposition of nitrogen oxides. *Catalysis.* 1982, **5**. https://doi.org/10.1039/9781847553171-00127
6. DEMUYNCK, J. AECC demonstration projects and AECC position on Euro 7. *AGVES meeting,* 26 November 2020, https://www.aecc.eu/wp-content/uploads/2020/11/201126-AECC-presentation-AGVES-1.pdf
7. ELSER, M., EL-HADDAD, I., MAASIKMETS, M. et al. High contributions of vehicular emissions to ammonia in three European cities derived from mobile measurements. *Atmospheric Environment.* 2018, **175**, 210-220. https://doi.org/10.1016/j.atmosenv.2017.11.030
8. FEV Magazine, Zero-Impact – Combustion Engine, 2020. https://magazine.fev.com/en/zero-impact-combustion-engine/
9. GURALP, O., QI, G., LI, W. et al. Experimental study of NO_x reduction by passive ammonia-SCR for stoichiometric SIDI engines. *SAE Technical Paper* 2011-01-0307. 2011. https://doi.org/10.4271/2011-01-0307
10. HOEKMAN, S. Review of nitrous oxide (N_2O) emissions from motor vehicles. *SAE International Journal of Fuels and Lubricants.* 2020, **13**(1):79-98. https://doi.org/10.4271/04-13-01-0005
11. MAROTTA, A., PAVLOVIC, J., CIUFFO, B. et al. Gaseous emissions from light-duty vehicles: moving from NEDC to the new WLTP test procedure. *Environmental Science & Technology.* 2015, **49**(14), 8315-8322, https://doi.org/10.1021/acs.est.5b01364
12. OSBORNE, R., LANE, A., TURNER, N. et al. A new-generation lean gasoline engine for reduced CO_2 in an electrified world. *Vienna Motor Symposium* 2019, 15-17 May 2019. Vienna, Austria.
13. PRADHAN, S. Development of an ammonia reduction aftertreatment systems for stoichiometric natural gas engines for stoichiometric natural gas engines. *Graduate Theses. Dissertations, and Problem Reports.* 2017, **6447**, https://researchrepository.wvu.edu/etd/6447
14. STRZELEC, A., KASAB, J. Automotive emissions regulations and exhaust aftertreatment systems. SAE International, USA, 2020.
15. SUAREZ-BERTOA, R., ASTORGA, C. Isocyanic acid and ammonia in vehicle emissions, *Transportation Research Part D: Transport and Environment.* 2016, **49**, 259-270. https://doi.org/10.1016/j.trd.2016.08.039
16. SUAREZ-BERTOA, R., MENDOZA-VILLAFUERTE, P., RICCOBONO, F. et al. On-road measurement of NH_3 emissions from gasoline and diesel passenger cars during real world driving conditions. *Atmospheric Environment.* 2017, **166**, 488-497. https://doi.org/10.1016/j.atmosenv.2017.07.056
17. SUAREZ-BERTOA, R., ZARDINI, A., ASTORGA, C. Ammonia exhaust emissions from spark ignition vehicles over the New European Driving Cycle. *Atmospheric Environment.* 2014, **97**, 43-53. https://doi.org/10.1016/j.atmosenv.2014.07.050
18. The ICCT. Beyond NO_x: emissions of unregulated pollutants from a modern gasoline car. 2019. https://theicct.org/sites/default/files/publications/NOx_Pollutants_LDV_FV_20190503_0.pdf
19. UNECE Regulation No. 49. https://eur-lex.europa.eu/legal-content/EN/ALL/?uri=CELEX:42013X0624(01)

Joseph Woodburn, MSci – Exhaust Emission Laboratory, BOSMAL Automotive Research and Development Institute Ltd in Bielsko-Biała, Poland
e-mail: *joseph.woodburn@bosmal.com.pl*

Article citation info:
ABRAMEK, K.F., OSIPOWICZ, T., MOZGA, Ł. The use of neural network algorithms for modeling injection doses of modern fuel injectors. *Combustion Engines*. 2021, **185**(2), 10-14. https://doi.org/10.19206/CE-137959

Karol Franciszek ABRAMEK
Tomasz OSIPOWICZ
Łukasz MOZGA

The use of neural network algorithms for modeling injection doses of modern fuel injectors

The article presents the possibilities of using artificial intelligence methods to model the injection doses of a modern Common Rail (CR) fuel injector. The presented neural network solution belongs to the experimental models known as black boxes in mechatronics. The backpropagation algorithm and its Levenberg-Marquardt expansion were used for the simulation. The analysis showed that there is a good match between the measurements and the computational model. The proposed solution can be used in the processes of diagnosing not only elements of the injection equipment, but also the internal combustion engine.

Key words: *fuel injector, CI engine, Common Rail system, neural network, engine diagnosing*

1. Introduction

The fuel injector is a device whose task is to distribute and spray fuel in the combustion chamber of the engine. The operating conditions in which it operates are extreme due to the pressures and temperatures inside the engine. The problems related to its deficiencies should be considered in terms of destructive processes coming from the outside (working conditions) and from inside (quality and pollution from the fuel). The output operating parameters of the fuel injector are the injection dose amount and the fuel injection delay. These parameters directly affect the characteristics of the internal combustion engine. As a result of the operation of the vehicle, the operating parameters of the fuel injector change. The process of diagnosis consists in analyzing them and assessing whether they are normal or not. However, standard diagnostics include individual points on the overall operating characteristics of the fuel injector. The research of the authors of the paper has shown that in some cases the analysis of individual points may be insufficient to diagnose a fuel injector. This applies in particular piezo injectors.

In [1], the authors presented a problem with the diagnosis of a vehicle with Continental VDO Siemens piezoelectric injectors installed. The engine ran unevenly at the speed of 1300–1800 rpm. The analysis showed that one of the fuel injectors generated too high injection dose in the pressure range of 40–90 MPa at the control time of 200 µs. The diagnosis of this fault took a long time because the tested injector was working properly during the standard test. In the paper [2], the authors proposed a method of diagnosing modern fuel injectors by analyzing the temperature of its body [3]. As a result of the leakage, the overflow dose increases, the liquid flow velocity inside the injector increases, which results in an increase in the areas of increased temperature leakage. The research on the diagnosis of CR injectors with the use of overflows has been described in [4]. By modifying the test procedure, it is possible to shorten the diagnosis time of the fuel injectors, achieving its very high accuracy by using artificial intelligence algorithms and implementing it into the test bench. The task of this process is to improve the methods of diagnosing elements of injection equipment by analyzing dosing areas omitted by the standard research process.

In the paper, the authors proposed the use of a neural network to model the injection doses of the selected research object. The proposed computational model can be compared to the experimental black box method [5] used in mechatronics. According to the authors of the above monograph, the input and output parameters of the research object as well as its structure and operation are known in the black box models (experimental), but the internal dimensions are not known. This method can be implemented to model injection doses of modern fuel injectors (Fig. 1).

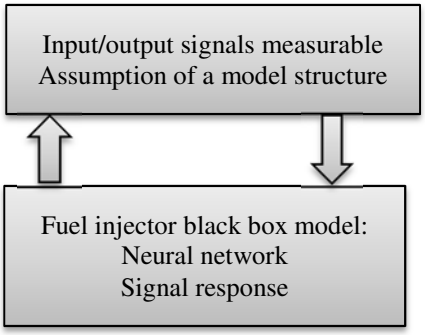

Fig. 1. Black box experimental model [2]

The antagonistic theoretical modeling method in mechatronics is the white box method. To use this method, it is necessary to know the internal dimensions and dependencies in the operation of the tested object. By analyzing the structure and operation of the kinematic associations of modern fuel injectors, it can be concluded that the preparation of the theoretical model called the white box requires precise measurements of the elements of precise pairs, diameters and lengths of the channels in the atomizer and the body. This process is difficult to implement, it is individual for each fuel injector and requires specialized measuring equipment [6].

By analyzing the literature on the considerations of the artificial intelligence method were used to study internal combustion engines. In the work [7], the Bayesian and back propagation algorithms were used to diagnose a compression-ignition engine. The engine was tested at various rotational speeds. The results of the analysis showed that the

Received 05 March 2021; Received in revised form 8 April 2021; Accepted 21 May 2021
Available online 25 May 2021

back propagation algorithm simulates the engine operating parameters more accurately than the Bayesian network. By analyzing the results of the experiment, it can be concluded that it is possible to use artificial intelligence methods to supervise the operation of internal combustion engines. The authors of the paper [8] implemented a neural network to predict combustion characteristics for an engine powered by a vegetable fuel. Artificial intelligence prediction was compared with the AVL simulation model. The results of the experiment were similar. To monitor the technical condition of a compression ignition engine, a neural network with the Random Convolutional Neural Network (RCNN) structure was implemented and described in [9]. Based on engine vibration during operation, artificial intelligence assessed its degree of wear. In order to detect early ignitions and knocking as a result, the authors of [10] developed an algorithm implementing artificial intelligence. The task of the neural network is to diagnose the combustion process in the engine during operation on the basis of data collected from the controller. The research presented in the paper [11] describes the diagnostic possibilities with the use of neural networks on the basis of engine noise. Based on the changes in engine noise during operation, the artificial intelligence algorithm assessed its technical condition.

It is possible to use artificial intelligence when diagnosing modern fuel injectors and assessing their output parameters. The authors of the paper developed an algorithm that models the size of injection doses using mechatronics methods on the basis of black box modeling.

2. Presentation of the selected algorithm

The process of learning neurons consists in calculating the sum of the values of the input products and the corresponding weights. The obtained value is subjected to the action of an appropriately defined activation function to obtain the output neuron. Having reference characteristics, it is possible to define an error at the output of the neuron. A similar method is used for determining the errors for the last layer in the case of multilayer networks. The problem is defining the error value for hidden layers, because without a pattern, the algorithm is not able to determine the size of the neurons for these areas. The error back propagation method should be used to solve this problem. In order to derive this algorithm, the error measure should be defined, which is the function Q(w). In this function, the variables are all weights of the multilayer neural network. The training of the network consists in finding the minimum of the function Q with respect to the vector w. Then the function should be expanded into the Taylor series in the closest vicinity of the known current solution w along the p direction, relation (1) [2].

$$Q(w+p) = Q(w) + |g(w)|^{T}p + 0{,}5p^{T}H(w)p + \cdots \ldots, \quad (1)$$

where g(w) is the gradient vector and H(w) is a matrix of second derivatives.

In general, the algorithm of the back propagation error method is written as follows (2)–(5) [9]:

$$y_i^{(k)}(t) = f\left(s_i^{(k)}(t)\right), s_i^{(k)}(t) = \sum_{j=0}^{N_{k-1}} w_{ij}^{(k)}(t)x_j^{(k)}(t) \quad (2)$$

$$Q_i^{(k)}(t) = \begin{cases} d_i^{(L)}(t) - y_i^{(L)}(t) \text{dlak} = L \\ \sum_{m=1}^{N_{k+1}} \delta_m^{(k+1)}(t) w_{mi}^{(k+1)(t)} \text{ dlak} = 1, \ldots, L-1 \end{cases} \quad (3)$$

$$\delta_i^{(k)}(t) = \varepsilon_i^{(k)}(t) f'(s_i^{(k)}(t)) \quad (4)$$

$$w_{ij}^{(k)}(t+1) = w_{ij}^{(k)}(t) + 2\eta\delta_i^{(k)}(t)x_j^{(k)}(t) \quad (5)$$

The operation of the algorithm starts at the moment of providing the training pattern to the network input. First, it is processed by the neurons of the first layer which determine the output signal. The signals obtained in this way are inputs for the neurons of the next layer. This cycle continues until the last layer. Having known the output signal of the last layer and the reference signal from the training sequence, it is possible to calculate the error at the network output from the dependence (2). Then, the weights of the last layer neurons are modified using the dependencies (2)–(4). The output error is propagated backwards according to the connections of neurons between the layers and taking into account their dependency activation function (2), (3). The second algorithm on the basis of which the neural network presented in the article was generated is the Levenberg-Marquardt algorithm. It uses the expansion of the function Q(w) expressed by the formula (1) to the third component [5].

3. Presentation of the results of measurements and simulations

Laboratory tests were performed using a test bench for testing injection pumps and STPiW3 fuel injectors. The research object was an electromagnetic fuel injector from Bosch, serial number 0445110083, generation 1.0.

The standard operating characteristics of the tested fuel injector were made on the test bench (Fig. 2).

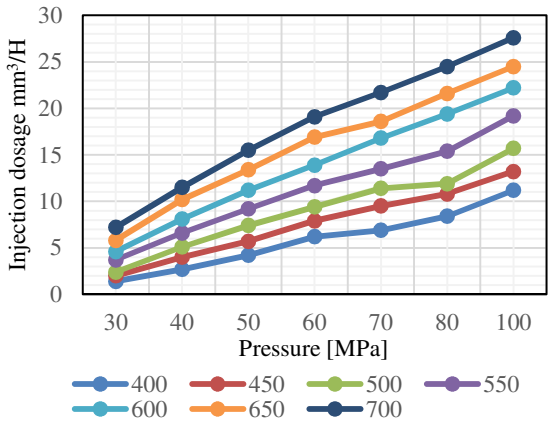

Fig. 2. Standard operating characteristics of the tested fuel injector – parameters measured on the test bench

Then, the second operating characteristic was performed, but with the injector control times changed (Fig. 3).

Based on the parameters from the standard operating characteristics of the fuel injector (Fig. 2), the neural network modeled the injection doses for the characteristic with changed control times (Fig. 4).

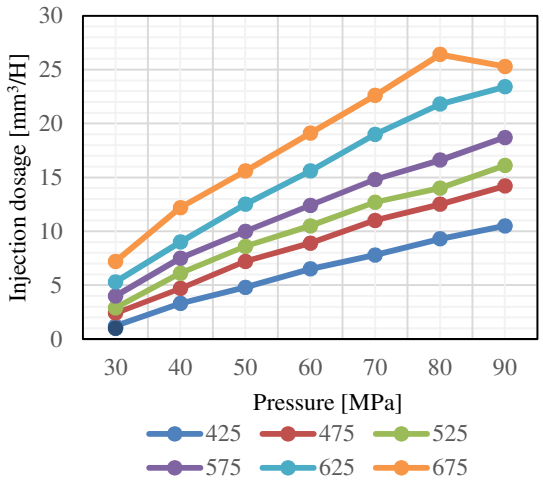

Fig. 3. Performance characteristics of the tested fuel injector – parameters measured on the test bench

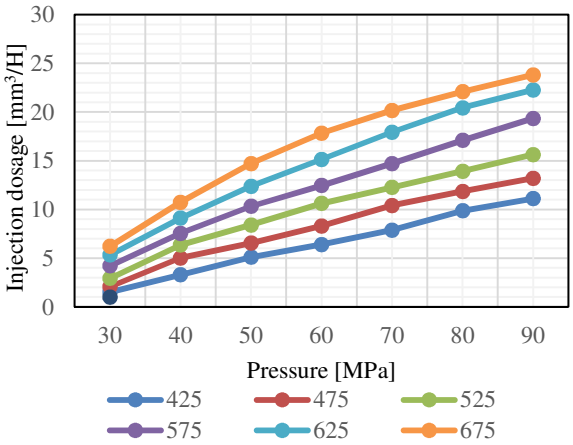

Fig. 4. Operating characteristics of the tested fuel injector – parameters modeled by the neural network

Figures 5, 6 and 7 show the parameters for selected fuel injector control times. In Figures 5 and 6, the fit of the model is very high, while in 7, slight differences occur for pressures of 70 and 80 MPa.

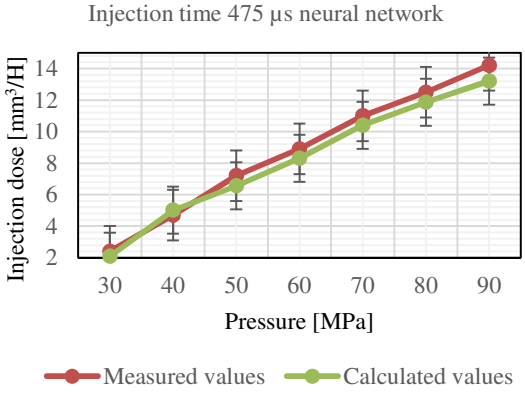

Fig. 5. Comparison of measured and calculated parameters for the injector control time of 475 µs

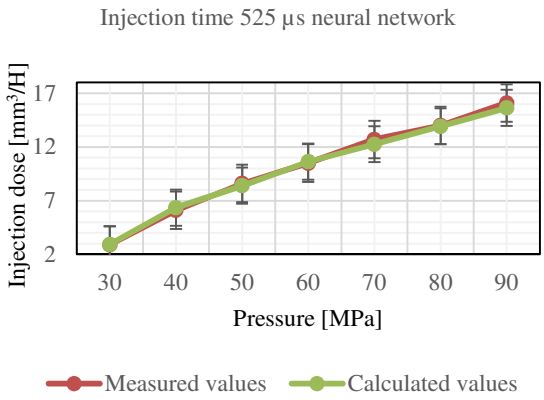

Fig. 6. Comparison of measured and calculated parameters for the injector control time of 525 µs

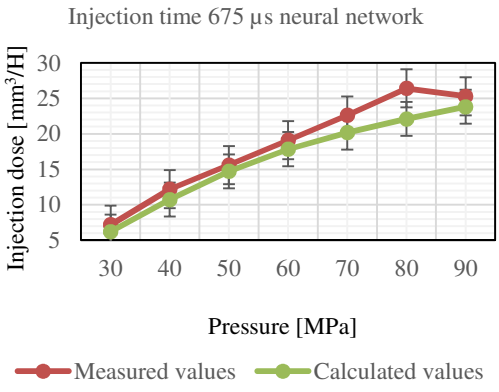

Fig. 7. Comparison of measured and calculated parameters for the injector control time of 675 µs

4. Discussion of research results

The model of the neural network proposed by the authors consists of two inputs (pressure in the system and fuel injection time) and one output: injection dose size. This network consists of three hidden layers, of which the first and the third layer have five neurons each, and the second layer contains four neurons. The last layer is the output layer, which consists of one neuron. The number of layers depends on the complexity of the model (variables). A single neuron divides the plane into two parts. Two layers can represent simplexes, i.e. convex areas limited by hyperplanes. The three-layer network is able to define any area, therefore a network model with three hidden layers was chosen. The selection of the number of neurons in a given layer was selected according to Kolmogorov theorem: the number of neurons in a layer should be 2n + 1 where n is the number of inputs. So our network should have 5 neurons in each hidden network. However, during the tests it was noticed that the combination of 5–5–5 does not reflect the model perfectly. Then, the algorithm of back propagation of errors was selected, which is to select appropriate weights for individual neurons during their training, and its modification, the Levenberg-Marquardt algorithm. A neural network model with five neurons in each hidden layer is not an optimal solution. For the purposes of the research, an algorithm aimed at creating a neural net-

work and training it was modified, which consisted in finding the best structure, i.e. selecting such a number of neurons in each of the three layers that the mean absolute error was as small as possible, determined by the relationship (6):

$$sbb = (\sum(|Xi| - |Yi|))/n \quad (6)$$

where: sbb – mean absolute error, Xi – injector dose obtained during measurements on the test bench, Yi – injector dose determined from the test bench, n – number of doses tested.

With three layers of five neurons each, the authors created an algorithm that checked 125 possible combinations, assuming the number of neurons in each layer from one to five. In addition, each network structure was trained five times and their mean absolute error was calculated to reduce the impact of the randomness of selecting weights at the beginning of learning a given structure. Our tests and analyzes show that building a neural network with a structure of 5–5–5 is suboptimal and burdened with high risk, and that the network used will be inaccurate.

Table 1. Results of the mean absolute error of the neural network 5–5–5

	1	2	3	4
621	0.9180	5	5	5
622	1.622	5	5	5
623	2.5320	5	5	5
624	0.8839	5	5	5
625	0.7564	5	5	5

Table 1 shows the values of the mean absolute errors for a particular network training attempt. In the best case, the error was 0.07564 and in the worst one it was four times higher. This structure is not very stable. Finally, the mean of all errors is 1.2505. It is far too high. Our criterion was that the error should not exceed 1. Table 2 shows the structure of the network 5–4–5 chosen as the most optimal.

Table 2. Results of the mean absolute error of the neural network 5–4–5

	1	2	3	4
596	0.7973	5	4	5
597	0.8165	5	4	5
598	0.7605	5	4	5
599	0.9139	5	4	5
600	0.9960	5	4	5

The smallest error is 0.7605 and the largest one is 0.9960, the maximum difference is 0.2355. The error values are very close with each learning attempt. Additionally, their value does not exceed 1. Out of all 125 combinations this network structure, i.e. 5–4–5, is the most optimal for our tests.

The analysis of the research carried out on the various combinations presents:

– the best structures of a neural network, in which the error is as small as possible, are obtained in networks in which at least one hidden layer has 5 neurons,
– the structure 5–5–5 is not very stable because during each learning the mean absolute error may differ several times from the previous learning,
– Kolmogorov's statement is not accurate and may serve as a guideline for the selection of the shape of the neural network.

After selecting the appropriate structure of the neural network, the process of its training began in order to achieve the lowest possible error. Structural science studies have shown that the lowest absolute error was achieved at the level of 0.6682.

Table 3 shows the error values between the output parameters measured and calculated for each input data.

Table 3. The size of the error between the parameters measured on the test bench and the model of the neural network structure

	30	40	50	60	70	80	90
425	–0.32	0.01	–0.30	0.09	–0.08	–0.56	–0.61
475	0.32	–0.31	0.65	0.59	0.60	0.64	0.99
525	–0.02	–0.26	0.20	–0.13	0.44	0.07	0.47
575	–0.21	–0.05	–0.33	–0.06	0.09	–0.49	–0.64
625	–0.03	–0.10	0.12	0.45	1.06	1.37	1.12
675	0.97	1.47	0.88	1.26	2.42	4.30	1.49
725	–0.15	0.53	0.67	1.63	1.24	0.68	1.27

Analyzing the above results, the average error is 0.48 mm^3/H, the maximum error is 4.30 mm^3/H and the minimum one is –0.64 mm^3/H.

There are known computational methods for analyzing the amount of injection doses using polynomials. The disadvantage of these methods is that the input quantities are limited (only two data can be used). When using artificial intelligence methods, any number of inputs can be used, which is very important in diagnostic processes.

5. Summary

The analysis of simulation tests showed that it is possible to use artificial intelligence (AI) methods to model the size of injection doses of modern fuel injectors. The implementation of the artificial intelligence algorithm is characterized by a high fit, therefore the results of mathematical modeling are similar to the experimental ones. The aim of the simulation was to investigate whether it is possible to model the output parameters of a modern fuel injector without knowing its internal dimensions on the basis of modeling a standard operating characteristic. The Neural Network add-on of the Matlab environment was used to make the model.

Further work carried out by the authors of the paper is aimed at improving the artificial intelligence algorithm by introducing additional input variables. The modification will consist in indicating to the algorithm how individual elements of the fuel injector affect the size of injection doses in individual areas of its operating characteristics. Additionally, the algorithm will be implemented in the test bench controller. The proposed algorithm can be used in the diagnostics of other engine components and the analysis of its current parameters during operation. The analytical methods proposed by the authors represent an innovative approach to prediction of injection doses of a selected fuel injector.

Nomenclature

CI	compression ignition
CR	common rail
sbb	mean absolute error
Xi	injector dose obtained from measurements on the test bench
Yi	injector dose modeled from the test bench
N	number of samples
NN	Neural Network

Bibliography

[1] OSIPOWICZ, T., ABRAMEK, K.F. Diagnosing methods common rail fuel injectors. *Combustion Engines*. 2017, **168**(1), 56-61. https://doi.org/10.19206/CE-2017-109

[2] OSIPOWICZ, T., ABRAMEK, K.F. The analysis of temperature disintegration on the body of fuel injector during research on test bench. *Combustion Engines*. 2017, **168**(1), 172-177. https://doi.org/10.19206/CE-2017-128

[3] ELIASZ, J., OSIPOWICZ, T., ABRAMEK, K.F., MOZGA, Ł. Model issues regarding modification of fuel injector components to improve the injection parameters of a modern compression ignition engine powered by biofuel. *Applied Sciences*. 2019, **9**(24), 5479. https://doi.org/10.3390/app9245479

[4] KNEFEL, T. Ocena techniczna wtryskiwaczy Common Rail na podstawie doświadczalnych badań przelewów. *Eksploatacja i Niezawodnosc – Maintenance and Reliability*. 2012, **14**(1), 42-53.

[5] RUTKOWSKI, L. Metody i techniki sztucznej inteligencji. *Wydawnictwo Naukowe PWN*. Warszawa 2012.

[6] MARCIC, S., MARCIC, M., PRAUNSEIS Z. Mathematical model for the injector of a common rail fuel – injection system. *Engineering*. 2015, **7**(6). https://doi.org/10.4236/eng.2015.76027

[7] CAI, B., SUN, X., WANG, J. et al. Fault detection and diagnostic method of diesel engine by combining rule – based algorithm and BNs/BPNNs. *Journal of Manufacturing Systems*. 2020, **57**(7), 148-157. https://doi.org/10.1016/j.jmsy.2020.09.001

[8] KARAMI, R., RASUL, M.G., MASUD, M. et al. Experimental and computational analysis of combustion characteristics of a diesel engine fueled with diesel-tomato seed oil biodiesel blends. *Fuel*. 2021, **285**, 119243. https://doi.org/10.1016/j.fuel.2020.119243

[9] WANG, R., CHEN, H., GUAN, C. Random convolutional neural network structure: An intelligent health monitoring scheme for diesel engines. *Measurement*. 2021, **171**, 108786. https://doi.org/10.1016/j.measurement.2020.108786

[10] KUZHAGALIYEVA, N., THABET, A., SINGH, E. et al. Using deep neural networks to diagnose engine pre-ignition. *Proceedings of the Combustion Institute*. 2020, 38(4), 5915-5922. https://doi.org/10.1016/j.proci.2020.10.001

[11] WANG, Y., LIU, N.N., GUO, H. et al. An engine-fault-diagnosis system based on sound intensity analysis and wavelet packet pre-processing neural network. *Engineering Applications of Artificial Intelligence*. 2020, **94**, 103765. https://doi.org/10.1016/j.engappai.2020.103765

Karol F. Abramek, DSc., DEng. – Faculty of Mechanical Engineering and Mechatronics at West Pomeranian University of Technology.
e-mail: *karol.abramek@zut.edu.pl*

Łukasz Mozga, MSc. – Faculty of Mechanical Engineering and Mechatronics at West Pomeranian University of Technology.
e-mail: *lukasz.mozga@zut.edu.pl*

Tomasz Osipowicz, DEng. – Faculty of Mechanical Engineering and Mechatronics at West Pomeranian University of Technology.
e-mail: *tosipowicz@zut.edu.pl*

Article citation info:
IDZIOR, M. Aging of engine oils and their influence on the wear of an internal combustion engine. *Combustion Engines*. 2021, **185**(2), 15-20. https://doi.org/10.19206/CE-138033

Marek IDZIOR

Aging of engine oils and their influence on the wear of an internal combustion engine

New designs of internal combustion engines require the use of engine oils that can cope with more demanding conditions, primarily with greater loads and higher temperatures. The requirements of recent years have led to a wider use of modern base oils and specially designed additive packages. This avoids the formation of impurities and changes in viscosity as a result of shearing of the viscosity additives under high loads. The article discusses the important problem of oil aging during operation and the impact of this phenomenon on the operation of internal combustion engines. The influence of oil service life and its replacement on the emission of toxic exhaust gas components was discussed, and the results of research on the effect of oil service life on changes in their viscosity were presented.

Key words: *combustion engines, engine oils, aging of engine oils, viscosity, selection*

1. Introduction

The rapid development of the modern automotive industry in recent years implies the creation of new car designs, including, in particular, new, revolutionary drive systems. Suffice it to say that the number of cars in the world already in 2010 exceeded a billion, while at that time about 7.2 billion people. And in the not so distant year 1970, the number of vehicles in Poland was about 0.5 million – thus about 80 compatriots per 1 car. Today, around 7 people in the world are related to one vehicle. The huge supply of cars makes car concerns outdo each other in meeting the expectations of car buyers to attract customers, who choose a model not only based on the price, brand and color as it used to be in the past, but also engine power, fuel consumption and driving comfort. And in the engine there are extremely unfavorable operating conditions: combustion temperatures reaching even above 2000°C, rotational speeds in a normal engine of 6000 rpm, i.e. 100 rpm. At these revolutions, the piston must cover the distance between the so-called cylinder blind spots 100 times per second! Its movement speed reaches 20 m/s.

An engine without proper lubrication breaks down very quickly or even gets destroyed. Therefore, for many years, oil companies have been working on the development of engine oil technology that will protect the engine against wear so that it can withstand hundreds of thousands of kilometers of mileage and years of operation. It will be possible if the oil fulfills the tasks set for it.

New designs of internal combustion engines require the use of engine oils that can cope with more demanding conditions, primarily with greater loads and higher temperatures. The manufacturers' strategy requires, among other things, an increase in boost pressure and advanced control of the combustion process and exhaust gas cleaning. This in turn causes the engine accessories to become highly complex and subjected to extremely high loads. All this affects the reliability and durability [2, 15]. This creates more difficult conditions for engine oils. The requirements of recent years have led to a wider use of modern base oils and specially designed additive packages. The use of oil bases with a higher viscosity index makes it possible to reduce the content of viscose-depressants. This avoids the formation of impurities and changes in viscosity as a result of shearing of the viscosity additives under high loads. The most important changes in newly produced engine oils are the selection of shear-resistant viscosifying compounds and lubricating additives, compatible with exhaust gas treatment systems and at the same time fulfilling their functions in conditions of high pressure and high temperature [1, 6].

Additionally, the gears mechanically account for approx. 7% of total fuel consumption. In rolling bearings, new types of seals and special plastic greases are used to reduce energy losses. Achieved savings are from 30 to 50% resistance to motion. In the case of mechanisms that work together without rolling bearings, the solution is to use gear or engine oils of correspondingly lower viscosity. Less common synthetic oils are also used in gearboxes, and carbon fibers instead of molybdenum and light metal alloys are more and more often used for the friction surfaces of synchronizers, which on the one hand reduce the weight of the mechanism, but on the other – are more susceptible to the transmission of vibrations.

2. Aging of oils during exploitation

The constant aging of the used oil is caused by the action of the oxygen contained in the air, which reacts relatively easily with the hydrocarbons. As a result of their oxidation, compounds with the structure of alcohols, aldehydes and organic acids are formed, resin products undergoing secondary condensation reactions in the form of hard-to-remove lacquers, deposited on the internal surfaces of the engine. This is accompanied by the simultaneous detachment of hydrogen atoms from hydrocarbon chains, which causes the formation of double bonds in them, which are the cause of parallel polymerization processes. After very long runs, the oil turns into thick, black tar, unable to lubricate anything, and in extreme cases – even into a solid. The oxidation process is accelerated by high temperature, as it causes thermal decomposition of base oil hydrocarbons, viscosity modifiers and some improvers [4, 5].

The operating conditions of engine oil determine its quantitative and qualitative consumption (especially the operating temperature affects the intensity of physicochemical changes, e.g. oxidation). The quality, composition, and physicochemical properties of engine oil are important engine operating factors that can largely affect the composition and emissions of toxic components formed in the en-

Received 18 March 2021; Received in revised form 21 May 2021; Accepted 23 May 2021
Available online 24 May 2021

gine's operating process. The effect of oil on these indicators is a complex and not fully understood phenomenon.

The influence of engine oil on the emission of toxic exhaust gas components also takes place by influencing the efficiency of catalytic exhaust gas treatment systems. The parameters of engine oils during the operation of the engine are not uniform and they change depending on the operating conditions, number of kilometers traveled, operating time, technical condition of the engine and its cooperating components. Any changes in the properties of lubricating oils that go beyond the lower and upper limit ranges adopted for them have negative effects in the form of possible damage and an increase in the emission of toxic exhaust components. Fig. 1 shows changes in oil properties during exploitation.

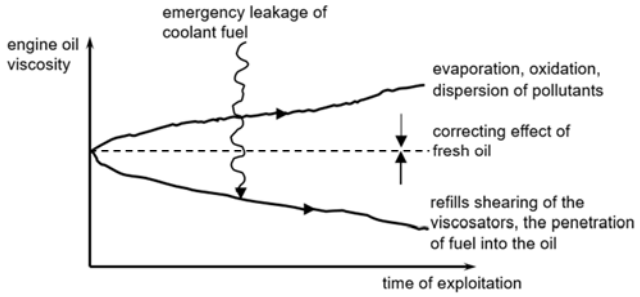

Fig. 1. Changes in oil properties during exploitation

The effects of improper oil durability or improperly set oil change cycles become visible later, during engine repair. When viewing its disassembled pistons, it is easy to determine the ease of formation and the type of contamination deposited thereon (Fig. 2).

Fig. 2. Used oil in the engine

Therefore, it is extremely important to regularly replace used engine oil with fresh oil, which initially cleans the entire lubrication system, and then protects it for the rest of its operation. The oil filter must be changed at the same time, as it is only designed for a certain mileage. Then, although it does not block the circulation, it ceases to participate in it due to the so-called shunting. The extended mileage between oil changes recommended by various manufacturers is often not due to technical needs (defined as a standard around 15,000 km), but for marketing reasons. American car makers, by no means obsolete, are even stricter in this regard, requiring a 4,000 to 6,000 mile (7,200 to 9,600 km) replacement of their engine oil, in part due to the widespread use of more easily degraded cars in American mineral oils.

3. Influence of oil exploitation time and oil change on the emission of toxic exhaust gas components

Many studies on the impact of engine operation time with specific oils on their quality wear, i.e. oil aging, indicate their impact on the amount of toxic exhaust components emitted. The graphs (Figs. 3–5) show the results of the research [7] on the influence of the engine oil operation time on the emission of individual exhaust gas components and fuel consumption, as well as on how the amounts of the emitted components change after replacing with new oil. Oil aging, i.e. deterioration of its properties over time, but also, for example, engine operation conditions, the quality of the fuel being filled, the quality of the oil itself, the amount of contaminants in the engine, affect the time interval in which the engine oil is changed.

The graphs (Fig. 3–5) show two engine exploitation modes [7]:
– condition 1 – low load,
– condition 2 – medium load.

The horizontal axis of all graphs shows the engine again time and the oil again time. The graphs show fuel:
a – oil A, lower quality oil,
b – oil B, better quality oil.

The tests were carried out for a diesel engine with a capacity of 2.5 dm^3, turbocharged 92 kW and oils: A – mineral 15W-40, viscosity coefficient 135, B – synthetic 0W-40, viscosity coefficient 183.

Figure 3 shows the influence of oil operating time on fuel consumption in the engine; it can be seen that oil B has narrower ranges of fuel consumption values, regardless of whether it is low or medium load operation. Both oils have a negative effect on fuel consumption and you can see that fuel consumption is on an upward trend, and when changing to a new oil, it returns to its initial state.

Figure 4 shows the effect of oil operation time on the emission of particulate matter – there is a large range of values of particles in the oil of lower quality at low load, while with B oil, these values are low and have little differentiation. After replacing the oil with a new one, the values for oil A slightly increase, while for oil B they even decreased. Figure 5 shows NO_x emissions – nitrogen oxides at higher loads show higher values due to higher combustion temperature, while oil A at low load after working for 126 hours has quite a sudden increase in emissions, this may be due to poorer oil quality and the accumulation of pollutants,

this means oil aging greatly affects the emission of nitrogen oxides.

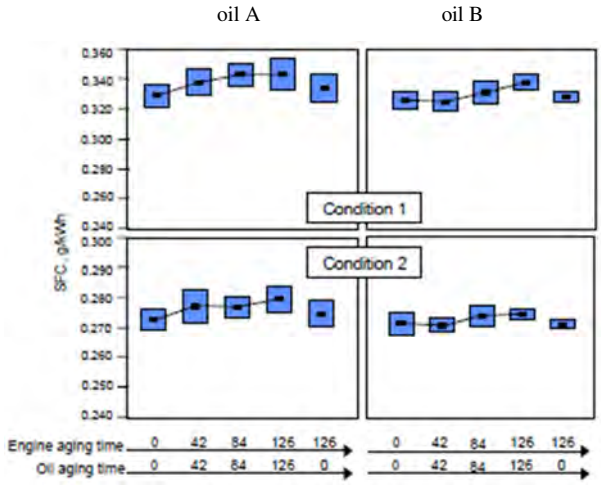

Fig. 3. Influence of oil operation time on fuel consumption

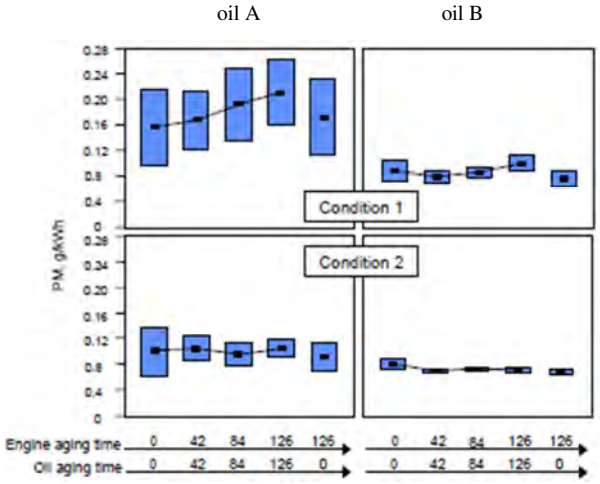

Fig. 4. Influence of oil operation time on the emission of solid particles

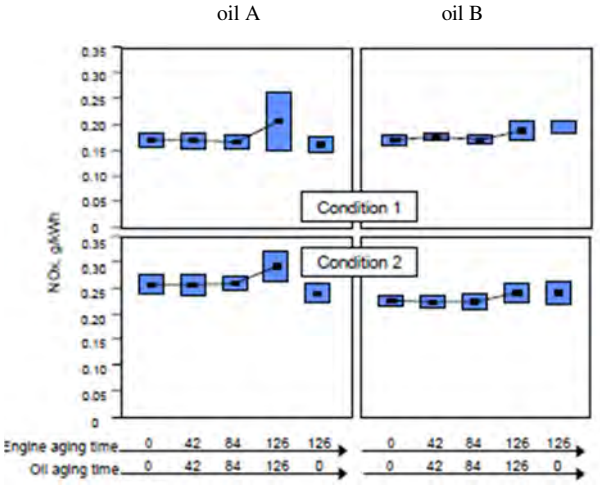

Fig. 5. Influence of oil operation time on the emission of nitrogen oxides

It follows that the use of synthetic oil contributes to the reduction of NO_x and particulate emissions. The emission of nitrogen oxides is related to the content of aromatic hydrocarbons, which also affect the density of the engine oil. Figure 5 shows that the use of mineral oils increases NO_x emissions by about 8%. In addition, the lower number of aromatic hydrocarbons characteristic of synthetic oil contributes to a better oil viscosity index.

4. Research on the influence of oil exploitation time on changes of their viscosity

The aim of the research was to determine the change in viscosity of engine oils depending on the mileage of a passenger car. LongLife oils were used for the tests, with a replacement interval every 30 thousand. km. This type of oil was chosen because of its widespread use in modern internal combustion engines; Synthetic oils are used more and more because of their quality and positive influence on fuel consumption reduction. The issues discussed in the paper concern mainly the variability of viscosity depending on various factors [11, 15]. Moreover, the types, properties and additives of motor oils have been presented quite extensively in order to study their relationship with the oil viscosity. Thanks to this, the obtained results can be considered in a broad aspect.

The test consisted in determining the viscosity of Castrol Edge 5W30 oil samples taken from passenger car engines with various mileage. All samples came from both petrol and diesel engines. Moreover, they were only turbocharged TSI or TDI engines, serviced at an authorized vehicle service station. As the samples come from engines with different powers and capacities, and the cars were driven by different drivers and under different conditions, the test results are indicative.

On the basis of the conducted research, the optimal mileage for LongLife oils used in petrol and diesel engines was determined to an approximate degree. This mileage is indicative, because the oil samples come from the engines of one brand of cars, serviced in authorized service centers, although used by different drivers. As the driving style and the main conditions of car use (urban, extra-urban, mixed traffic) also affect the consumption and parameters of the oil, it is impossible to determine the exact mileage at which an oil change should occur.

In the conducted tests, the kinematic viscosity of the engine oil was measured. The collected oil samples were selected based on similar mileages from petrol and diesel engines. Oils derived from gasoline engines were considered separately. In addition, the new oil was also tested to compare its parameters with the manufacturer's data. In the case where an oil sample was taken from an engine with less than 30,000 service mileage. km, this was only done when the oil change warning light came on. Modern cars are equipped with an on-board computer with special software that keeps track of the car's driving statistics. Information on the number of actuations as well as the time and speed of travel is saved. On this basis, the computer estimates the mileage after which the oil should be changed. In a situation where the car is used primarily in city traffic, with a large number of stops, and the average speed does not exceed 50 km/h, the oil change indicator may light up after 7,000. km. The oil samples were taken after the runs listed in Table 1.

Table 1. The mileage after which samples of engine oils were taken

Type of engine	
Diesel	Petrol
Mileage [km]	
10000	9800
11200	11526
15435	14000
15800	14800
21246	18200
23150	19020
23689	24533
26108	25353
29063	28900
30000	29339

Each sample was tested for kinematic viscosity at 19°C and 45°C, and then the viscosity of the samples was determined at 100°C. The test results with the calculated values are presented in the graphs in Fig. 6 and 7. For a more precise analysis of the viscosity changes for individual samples, the test results, together with the calculated values, are presented in the form of graphs on the above-mentioned drawings showing the kinematic viscosity as a function of temperature [7].

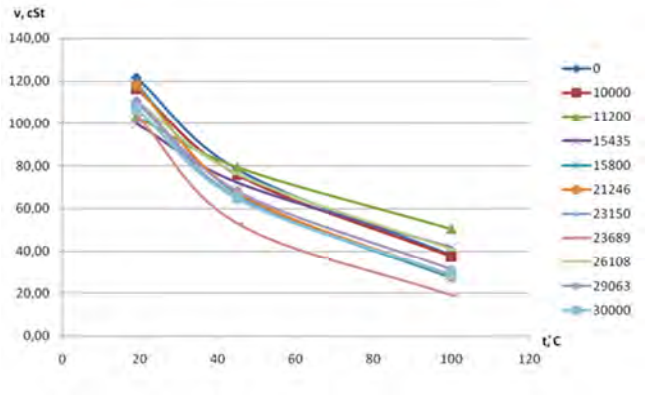

Fig. 6. Change in viscosity of oil samples taken from diesel engines depending on the temperature

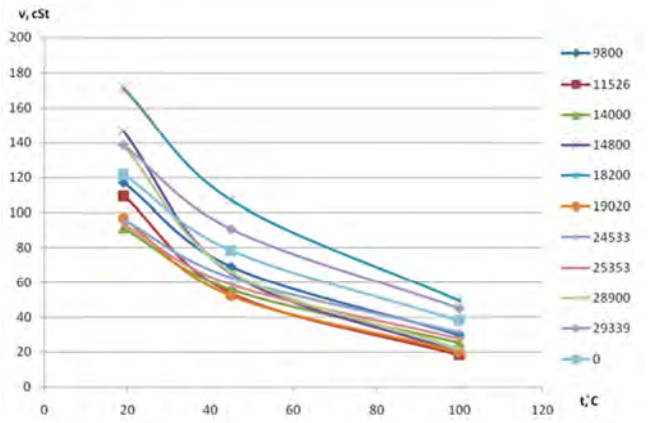

Fig. 7. Change of viscosity of oil samples taken from petrol engines depending on the temperature

When analyzing the above results, it is noticed that more than a twofold increase in temperature from 19°C to 45°C causes a decrease in viscosity by several dozen percent in both diesel and petrol engines. With regard to the maximum and minimum values, in diesel engines they are respectively 119.01 cSt for 15,800 km (19°C) and 18,94 cSt for 23,689 km (100°C), and for petrol engines 171.49 cSt for 18,200 km (19°C) and 18.30 cSt for 11,526 km (100°C). Thus, for the maximum value, the difference between diesel and petrol is as much as 70%, and for the minimum value – less than 4%. Presumably the sample with a viscosity of 171.49 cSt was from contaminated oil as the remaining petrol engine viscosities are much lower.

When looking at the graph for diesel engines (Fig. 6), it can be seen that the curves for individual samples have a very similar shape, so their percentage changes in viscosity are similar. The viscosity of the new oil varies from about 120 cSt to less than 40 cSt. A sample with a mileage of 10,000 km has almost the same mileage. On the other hand, the sample whose mileage is the most different from the new oil curve is the one with a mileage of 23,689 km. In addition, other samples, the viscosity of which at 100°C drops below 31 cSt, are samples with the following runs: 29,036 km, 30,000 km, 23,150 km, 21,246 km, 15,800 km and 23,689 km. Among the samples with a mileage of more than 20,000 km, only one (26,108 km) maintains its viscosity at 100°C at the level of 40 cSt. Moreover, the sample with a mileage of 15,800 km also has a low viscosity. This may indicate the need to change the oil no later than after 15,000 km. On the other hand, the viscosity of the new oil at 100°C was determined by interpolation and not by testing. Hence the difference – according to the manufacturer, the oil viscosity at 100°C is about 13 cSt. However, assuming there is some constant interpolation error, comparisons can be made for all viscosities obtained by this method. It is also worth noting that none of the samples showed increased viscosity at 19°C. This proves that there is a small amount of impurities that may increase the viscosity of the engine oil.

With regard to petrol engines, the samples taken from them have similar characteristics to those taken from diesel engines (Fig. 6). The chart shows that the sample with the mileage of 9800 km is the most similar to the new oil. Only two samples have higher viscosities than the new oil – these are samples with mileage of 18,200 km and 29,339 km. While the increase in viscosity in a sample with a mileage of less than 30,000 km is explained by a large amount of impurities, for a sample with a mileage 18,200 km, justification should be sought in the difficult engine operating conditions. Most likely, the car from which the sample was taken was used mainly in typically urban conditions.

It is also worth mentioning that the sample curve with a mileage of 28,900 km is very steep, which is unfavorable due to large and quite rapid changes in temperature as a function of viscosity. Moreover, the oil with the mileage of 19,020 km, which is not the oil with the highest mileage, has the lowest viscosity at 100°C. It is possible that this oil has been diluted with gasoline that has entered the lubrication system. This can be thought because the viscosity of gasoline is only 1 cSt, so even a small amount of it can

have a big impact on lowering the oil viscosity. This results in a difficult oil film formation and, consequently, even engine seizure.

In order to show how much dirt gets through despite the use of modern filters for engine oil, a photo was taken (Fig. 8) comparing (from left to right) oil from a petrol engine with a mileage of 29,339 km, fresh oil and oil from a diesel engine with a mileage of 29,063 km. You can clearly see how much not only the color of the oil has changed, but also how much sediment there is. The dark, almost black color of the oil is mainly influenced by solid particles, mainly composed of carbon. This is also a problem with modern petrol engines due to the use of direct injection.

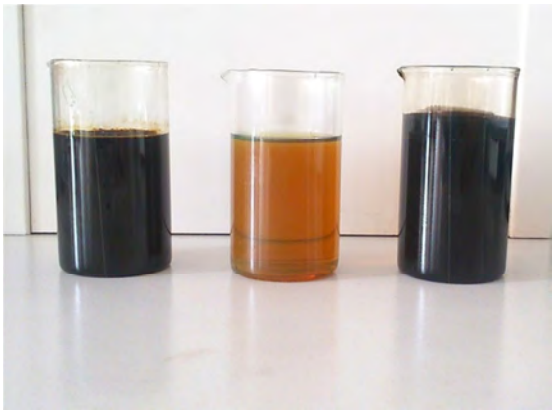

Fig. 7. Beakers containing (from the left) oil from the petrol engine (29,339 km), fresh oil and oil from the diesel engine (29,063 km)

5. Conclusion

Requirements for internal combustion engines are increasing, especially in the face of offensive competition of electric drives. Therefore, engines are expected, above all, to increase their power, fuel consumption and toxic exhaust emissions. Because of this essential is the development of fuels and lubricants used in the operation of vehicles.

A visible trend in changing the properties of engine oils is the introduction of oils of lower and lower viscosity to the market. Lower viscosity results in reduced frictional resistance, but with decreasing viscosity, the ability to form an oil film in the friction junctions decreases. The viscosity of the oil mainly affects fuel consumption and improves the mechanical efficiency of the engine. Preliminary tests of engine oils marked SAE 0W-16, 0W-12 and 0W-8 showed an improvement in the performance of engines intended for the use of these oils. In the case of older engines, too low viscosity leads to boundary friction, and even in extreme situations to seizure of the friction nodes. This is due to the design of the new engines. They are specially designed to operate under less effective hydrodynamic lubrication conditions.

Manufacturers of internal combustion engines try to design them in such a way that they are adapted to oils of relatively low viscosity. On the other hand, such oils are so low in viscosity at high temperatures that in sports, loosely fitting engines, they can enter the cylinder and burn. In this case, the manufacturer provides oil consumption standards of up to 1 dm^3/1000 km, but fuel consumption has a very detrimental effect on the environment. When comparing the test results for petrol and diesel engines, it is noted that while in the case of diesel engines it is possible to establish an approximate mileage at which the oil should be changed, for petrol engines it is practically impossible. For diesel engines, the curve closest to that of fresh oil is that of a sample with a mileage of 10,000 km. In the case of samples from SI engines, the sample with a mileage of 9800 km has the most similar, although not overlapping, curve. However, the viscosity of this sample at 100°C is as much as 7 cSt lower, therefore it is difficult to talk about similar values here. This may indicate how important the driving style of the driver and the area of use of a car with a turbocharged gasoline engine are on the quality of the oil. Probably one of the reasons for the rapid aging of the oil is the high temperatures in the engine. They are much higher than for supercharged diesel engines because the petrol engines achieve much higher RPM. As a result, the turbochargers in the petrol engines also have a higher RPM than in the diesel engines.

The problem of the selection of oils for internal combustion engines is also important in terms of environmental pollution – it is a topic that has been discussed very much and important in the last dozen or so years. The way internal combustion engines will be constructed in the coming years translates into pollution of our planet, therefore all possible solutions are used to meet the applicable exhaust emission standards. Anthropogenic pollution, i.e. man-made in the world, in relation to production processes, the municipal sector, agriculture, waste, energy used in industry, road transport has a significant share, in the case of carbon monoxide (CO) it is 22%, and nitrogen oxides (NO_x) is as much as 39%. When choosing an engine oil, one should therefore follow the recommendations of the vehicle's engine manufacturer – each engine has a different structure, different sizes of channels through which the oil flows to the elements where a continuous oil film must be created so that the engine can operate with the highest possible efficiency. It is also good to use higher quality oils that have a higher purity of the base oil and further better lubrication parameters and a lower impact on exhaust emissions. Oil change in engines operated in intensive city traffic, in off-road conditions or on long and fast motorway routes, should be performed much more frequently than indicated by "average" or "extended" standards. A reasonable solution to this problem are the computer systems for assessing oil suitability for further use introduced by many manufacturers.

Bibliography

[1] AHMED, N., NASSAR, A. Lubricating oil additives. *Egyptian Petroleum Research Institute.* 2011. https://doi.org/10.5772/22923

[2] ANDREWS, G., HALL, J., RAHMAN, A. et al. The influence of an on line heated lubricating oil recycler on emissions from an IDI passenger car diesel as a function of oil age. *SAE*

Technical Paper 2000-01-0232. 2000. https://doi.org/10.4271/2000-01-0232

[3] DEVLIN, M.T. Common properties of lubricants that affect vehicle fuel efficiency: A North American historical perspective. *Lubricants*. 2018, **6**(3), 68. https://doi.org/10.3390/lubricants6030068

[4] ANDREWS, G., ABDELHALIM, S., LI, H. The influence of lubricating oil age on oil quality and emissions from IDI passenger car diesels. *SAE Technical Paper* 1999-01-1135. 1999. https://doi.org/10.4271/1999-01-1135

[5] IDZIOR, M. Nowe metody rozwiązywania problemów współczesnych silników o zapłonie samoczynnym. *Zeszyty Naukowe Instytutu Pojazdów Politechniki Warszawskiej*. 2007, **3**(66), 5-21.

[6] IDZIOR, M. Badanie wpływu przebiegu pojazdów na zmiany właściwości olejów silnikowych, *Autobusy*. 2016, **6**.

[7] IDZIOR, M., WICHTOWSKA, K. Badanie wpływu przebiegu pojazdów na zmiany właściwości olejów silnikowych. *Autobusy*. 2016, **6**.

[8] JEFFERD, K., ROGERSON, J., COPP, D. et al. The impact of lubricants on heavy duty diesel engine fuel economy and exhaust emissions. *SAE Technical Paper* 2000-01-1983. 2000. https://doi.org/10.4271/2000-01-1983

[9] LECHNER, G., KNAFL, A., ASSANIS, D. et al. Engine oil effects on the friction and emissions of a light-duty, 2.2L direct – injection – diesel engine. Part 1 – engine test results. *SAE Technical Paper* 2002-01-2681. 2002. https://doi.org/10.4271/2002-01-2681

[10] MANNI, M., FLORIO, S., GOMMELLINI, C. Impact of fuel and oil quality on deposits, wear and emissions from a light duty diesel engine with high EGR. *SAE Technical Paper* 2000-01-1913. 2000. https://doi.org/10.4271/2000-01-1913

[11] MAMGBI, R., CERNY, J., BARIFAIJO, E. Time of exploitation and detergency properties of low SAPS engine oil. Nafta-Gaz, 2013, **69**(1), 57-65.

[12] SMITH, T., KERSEY, V., BIDWELL, T. The effect of engine age, engine oil age and drain interval on vehicle tailpipe emissions and fuel efficiency. *SAE Technical Paper* 2001-01-3545. 2001. https://doi.org/10.4271/2001-01-3545

[13] TRIPATHI, A., VINU, R. Characterization of thermal stability of synthetic and semi-synthetic engine oils. *Lubricants*. 2015, **3**(1), 54-79. https://doi.org/10.3390/lubricants3010054

[14] SP399-B-Facts about engine oils. *The University of Tennessee Agricultural Extension Service*. SP399B-1M-11/98(Rev)E12-2015-00-066-99. http://trace.tennessee.edu/utk_agexmach/5

[15] ZWIERZYCKI, W. Płyny eksploatacyjne do środków transportu drogowego. *Wydawnictwo Politechniki Poznańskiej*. Poznań 2006.

Prof. Marek Idzior, DSc., DEng. – Faculty of Civil and Transport Engineering, Poznan University of Technology.

e-mail: *marek.idzior@put.poznan.pl*

Article citation info:
GIECHASKIEL, B., MELAS, A. Emissions of a Euro 5 motorcycle over the world harmonized motorcycle test cycle (WMTC). *Combustion Engines*. 2021, **185**(2), 21-25. https://doi.org/10.19206/CE-138701

Barouch GIECHASKIEL
Anastasios MELAS

Emissions of a Euro 5 motorcycle over the world harmonized motorcycle test cycle (WMTC)

The Euro 5 limits for L-category vehicles are applicable since 2020 and for this reason there is lack of studies examining the emissions of this category. In this study we tested a 1000 cm^3 Euro 5 motorcycle over the World Harmonized Motorcycle Test Cycle (WMTC). The gaseous pollutants were approximately half of their respective limits. The cold start (first 2 minutes) contributed to the majority of the emissions. The solid particle number emissions were also 6.5 times below the limit for passenger cars, but the particles not counted with the current methodology were around 2 times higher. High concentrations of volatiles were emitted at the high speed part of the cycle.

Key words: *L-category, motorcycle, particle emissions, fuel consumption, WMTC*

1. Introduction

Registered mopeds (engine displacement < 50 cm^3) and motorcycles, collectively called powered two-wheelers (PTWs) accounted for more than 35 million vehicles in EU-28 in 2017, more than 10% of the passengers' mobility fleet [1, 2]. More than 25% of the PTWs are registered in Italy. In Europe, the share of households holding PTWs in 2015 was 10%–25% [3]. The annual registrations of motorcycles in the EU increased in recent years, exceeding one million both in 2018 and 2019. The registrations of mopeds, which are one third of the motorcycles, on the other hand decreased. The relative contribution of mopeds and motorcycles to air pollution started to increase as the levels from other vehicles started to decrease.

In 2013, Regulation (EU) No 168/2013 and in 2014, supplemental technical Regulation (EU) 134/2014 established implementation dates for Euro 4 (2016) and Euro 5 (2020) L-category vehicles (i.e. 2-, 3-and 4-wheelers such as mopeds, motorcycles, quads and minicar). The Euro 5 emission limits are at the same levels with the limits of passenger cars, but, in contrast to passenger cars, solid particle number (SPN) emissions are not regulated. Due to their recent introduction in the market, to the authors knowledge there are no published data in the literature regarding Euro 5 motorcycles. Speculations for the expected improvements can be found though [4]. The data on Euro 4 motorcycles, which also have to respect strict limits under the same cycle and protocol are also limited [4–6].

The respective laboratory cycle is the WMTC (world harmonized motorcycle test cycle), which is based on actual on-road driving profiles. For this reason, the laboratory emissions are expected to be closer to the real world emissions. The WMTC consists of urban, rural and motorway (highway) parts. Many studies give big emphasis to the urban emissions, where the population exposure is the highest [7]. When laboratory and real-world cycles are compared, it is important to compare the respective parts (e.g. urban real world cycles with the urban parts of the laboratory cycles).

The aim of this paper is to summarize the emissions of a Euro 5 motorcycle giving separately the emissions of the urban, rural and motorway parts. Special emphasis is given to the particle number emissions, which are not regulated for the specific motorcycle.

2. Materials and methods

2.1. Motorcycle

The motorcycle was Euro 5 type approved, with 1 L engine displacement, 115 kW max power at 10,500 rpm and 105 Nm max torque at 9000 rpm, with 5000 km on the odometer. It belonged to the high-performance motorcycles category (L3e-A3) because the power/weight ratio was > 0.2 kW/kg, and the maximum power > 35 kW. It had manual transmission, electronic injection and three-way catalyst.

The empty mass was 200 kg and an inertia of 290 kg was used for testing. Reference gasoline fuel with 5% ethanol content was used with density 0.743 kg/l (15°C).

2.2. Laboratory

The tests were conducted at the Vehicle Emissions Laboratory (VELA 1) of the European Commission - Joint Research Centre (JRC) (Ispra, Italy), at an ambient temperature of 23–25°C and relative humidity of 45%–55%. The exhaust of the motorcycle was diluted in a full dilution tunnel with constant volume sampling (CVS), which was set to 5.5 m^3/min (Fig. 1).

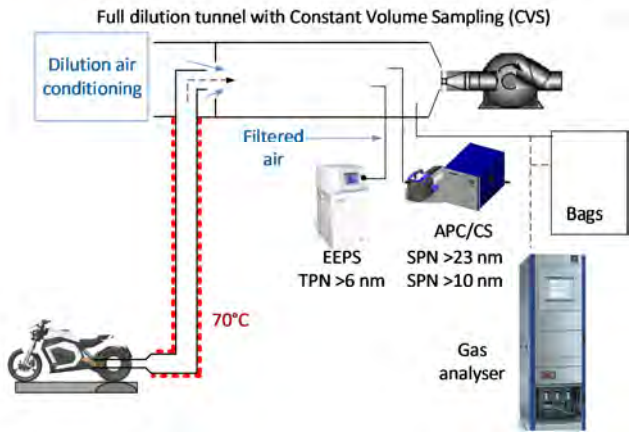

Fig. 1. Experimental setup

Received 28 May 2021; Received in revised form 8 June 2021; Accepted 9 June 2021
Available online 11 June 2021

The gaseous pollutants were measured from the dilution tunnel in real time with analyzers AMA i60 (from AVL, Graz, Austria). Furthermore, a small part of the diluted gas was also collected in bags and was analyzed for the gaseous pollutants at the end of the cycle with the same set of analyzers. The principle of operation of the analyzers was: non-dispersive infrared detection for carbon monoxide (CO) and carbon dioxide (CO_2), chemiluminescence for nitrogen oxides (NO_x), and hot (191°C) flame ionization detection for total hydrocarbons (HC) and methane (CH_4). Non-methane hydrocarbons (NMHC) were calculated from the difference of HC and CH_4.

An AVL particle counter (APC) 489 (AVL, Graz, Austria) [8], compliant with the light-duty vehicle regulations, was connected to the dilution tunnel. The system consisted of a hot diluter at 150°C, a catalytic stripper at 350°C [9], and a final porous diluter operating with room-temperature filtered air. For sub-23 nm, a catalytic stripper is necessary for the removal of volatile particles according to the latest Global Technical Regulation (GTR 15) for light-duty vehicles [10, 11]. The applied particle number concentration reduction factor (PCRF) was 500 (50 × 10). The PCRF was determined by the manufacturer during the calibration of the instrument and combined the dilution and average particle losses at 30, 50 and 100 nm, as required in the light-duty vehicles regulation. Downstream of the second dilution two TSI (Shoreview, MN, USA) butanol condensation particle counters (CPCs) with 50% counting efficiency at 23 nm (model 3790) and 65% efficiency at 10 nm (model 3772) were used to measure the PN concentrations of solid particles > 23 (SPN > 23 nm) and > 10 nm (SPN > 10 nm), respectively. The specific counting efficiencies are defined in GTR 15 [11].

An engine exhaust particle sizer (EEPS) (model 3090 from TSI) was connected to the full dilution tunnel using a simple diluter (dilution ratios 65–75:1). Such high dilution was necessary to avoid saturation at the last part of the cycle. The EEPS measured particle size distributions from 5.6 to 560 nm, based on particle charging and measuring their current at the electrometers where they deposited. As there was no thermal treatment, all particles (i.e., solids and volatiles) were measured (TPN > 6 nm).

2.3. Test cycle

The cycle was the WMTC (World Harmonized Motorcycle Test Cycle) stage 2, class 3, sub-class 3-2. The WMTC was introduced with Euro 4 and is based on actual driving patterns. Some characteristics of the cycle can be found in Table 1.

The cycle consisted of three phases (Fig. 2): Phase 1 or urban part, phase 2 or rural part, and phase 3 or motorway (highway) part (details in Table 1). Each phase was 10 min long (600 s) with a total cycle duration of 30 min (1800 s). The mean speed was 24.4 km/h in the urban phase, 54.7 km/h in the rural, and 94.4 km/h in the motorway phase. For the calculations of the cycle emissions, the weighing factors of phase 1 and phase 3 were 25%, and 50% for phase 2, as prescribed in the regulation.

The motorcycle was soaked at 23°C overnight and the test started with the engine at ambient temperature (cold start).

Table 1. Characteristics of the WMTC and its phases

	Phase 1	Phase 2	Phase 3	WMTC
Duration [s]	600	600	600	1800
Distance [km]	4.1	9.1	15.7	28.9
Mean speed [km/h]	24.4	54.7	94.4	57.8
Weighing factor [-]	0.25	0.5	0.25	-

2.4. Calculations

The emissions E were calculated from the real time signals from the dilution tunnel:

$$E_{j,k} = \left(\sum_k C_{j,i,c}\, \rho_j\, Q_i\right)/D_k \quad (1)$$

where j is the pollutant, k is the phase (urban, rural, motorway). $C_{j,i,c}$ is the background corrected concentration of the pollutant j at time i, ρ_j is the density of the pollutant, Q_i is the dilution tunnel flow rate, D_k is the distance of the phase. The fuel consumption (FC) was given from the equation given in Regulation (EU) No 134/2014:

$$FC = (0.848\ HC + 0.429\ CO + 0.273\ CO2)\ 0.118\ /\ \rho \quad (2)$$

where ρ is the fuel density.

3. Results

Figure 2 plots the speed profile and the exhaust gas temperature at the tailpipe. Figure 3 gives examples of real time emissions of regulated pollutants. The cold start emissions are high because the catalyst has not reached its light-off temperature. After the first two minutes the emissions are low, with relatively higher emissions during the motorway part.

Figure 4 plots the weighed WMTC results for the regulated pollutants. The emission levels were 45–60% of the respective limits.

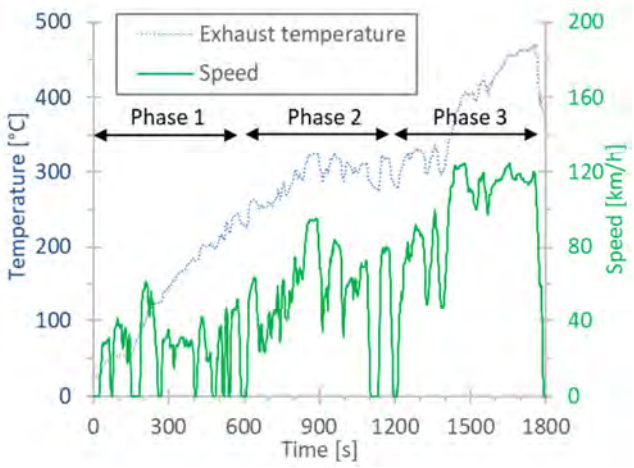

Fig. 2. Speed profile and exhaust gas temperature at the tailpipe

Figure 5 plots the particle number (PN) signals as measured from the dilution tunnel.

The solid particle number (SPN) emissions of particles > 23 nm and > 10 nm followed the speed profile, with high spikes during accelerations. High emissions were noted at the cold start. The motorway part had also high emissions, but there the dilution at the dilution tunnel is lower due to the higher exhaust flow rate. Due to the high speed, the distance specific SPN emissions were relatively low.

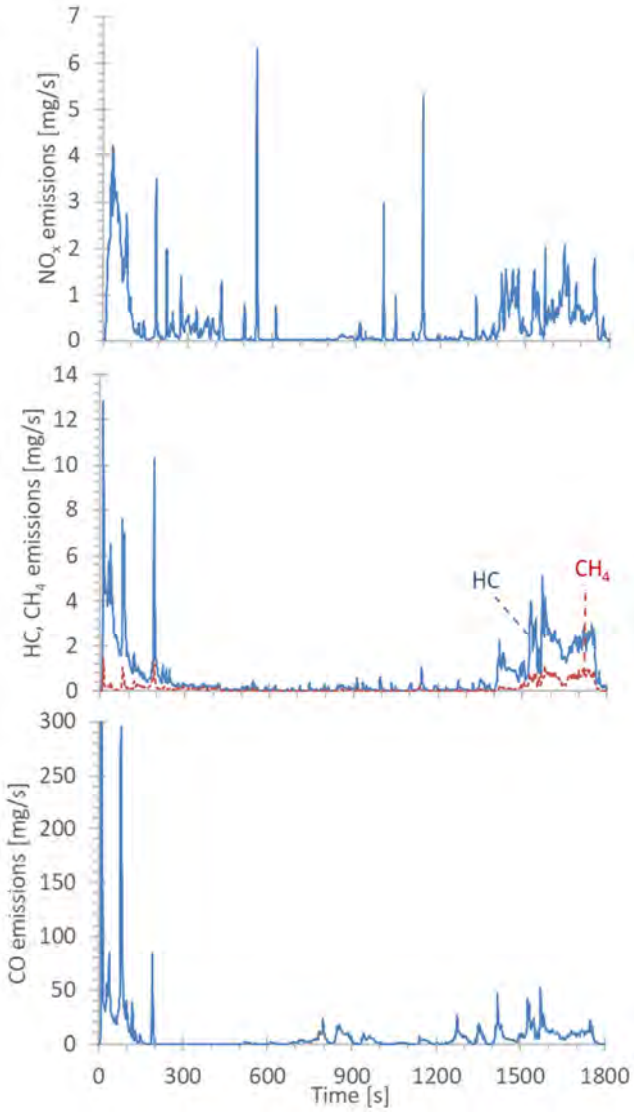

Fig. 3. Real time emissions of NO_x (upper panel), HC and CH_4 (middle panel) and CO (lower panel)

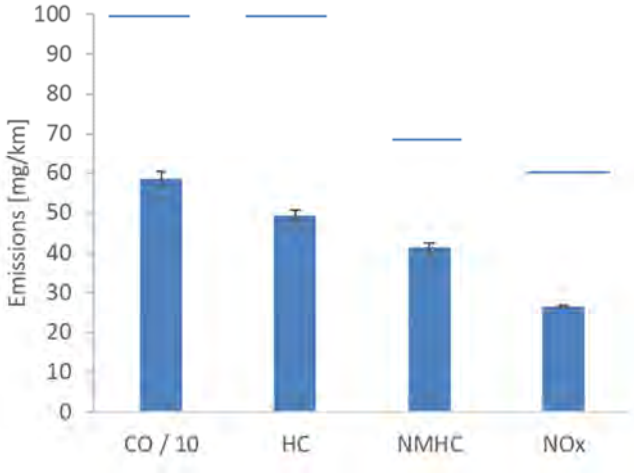

Fig. 4. Emission results of regulated pollutants. Blue bars give the motorcycle Euro 5 limits. Error bars show min-max of two repetitions. CO emissions and emission limit are divided with 10

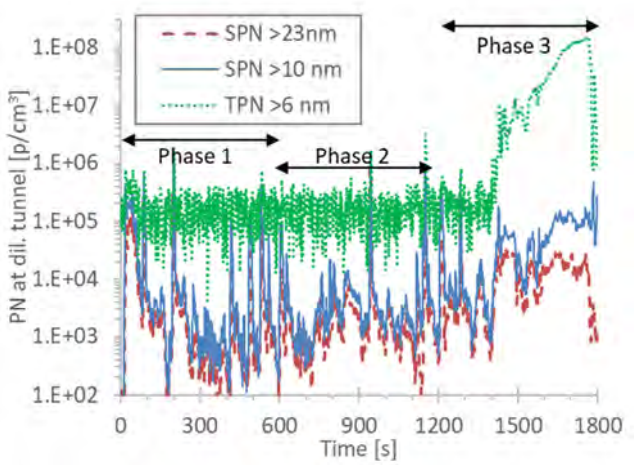

Fig. 5. Particle number (PN) emissions for solid (SPN) or total (TPN) particles as measured from the dilution tunnel. To convert to p/s multiply by 1.0E+05

The total particle number (TPN) emissions were measured with the EEPS without any thermal pre-treatment. Due to the high dilution used (around 70:1) and the high detection limit of the instrument, the background levels were even higher than the spikes of the SPN instruments at the urban and rural parts. At the motorway part a high increase of volatile particles occurred. This coincided with the increase of the exhaust gas temperature > 350°C (see Fig. 1).

The results of the gaseous pollutants, particles, fuel consumption and CO_2 are summarized in Table 2.

Table 2. Emission results for the WMTC and its phases. FC = fuel consumption; SPN = solid particle number; TPN = total particle number

	Phase 1	Phase 2	Phase 3	WMTC
CO [mg/km]	1687	176	302	585
NO_x [mg/km]	77	6	17	27
HC [mg/km]	141	6	44	49
CH_4 [mg/km]	19	1	11	8
NMHC [mg/km]	122	5	33	41
CO_2 [g/km]	197	112	119	135
FC [l/100 km]	8.7	4.9	5.2	5.9
SPN_{10} 10^{11} [p/km]	5.3	0.75	2.5	2.3
SPN_{23} 10^{11} [p/km]	2.2	0.35	0.52	0.87
TPN_6 10^{11} [p/km]	25	11	1560	400

4. Discussion

Emission factors were low but there are a few points that need further investigation. One is how these emissions change over time. There were no durability requirements for Euro 3 or older motorcycles and significant increases of the emissions with mileage accumulation have been reported [12]. Durability mileage, also indicated as useful life values, as determined in Annex VII of Regulation (EU) No 168/2013, is 35,000 km for motorcycles with maximum speed > 130 km/h. The Euro 5 deterioration factors are 1.3 for the regulated pollutants. This would mean that a 30% increase is expected until the end of the useful life of the motorcycle, but the emissions still have to respect the limits.

The second point is how close are the laboratory emissions to the real-world emissions. A few studies have found differences with older (and smaller) motorcycles, type approved with the older cycles [7]. More research is needed as

portable equipment will become available [13], in particular for Euro 5 motorcycles type approved with the WMTC, which is based on actual driving patterns and thus smaller differences are expected [14]. It is important to notice though that any comparison between laboratory and on-road tests needs to compare the real-world emissions with the appropriate part of the laboratory cycle (e.g. city emissions with the urban part). Table 2 gave the emissions of each part of the WMTC, and it is clear that there are big differences in emission levels between the different parts.

Another point is the high increase of volatiles when the exhaust gas temperature exceeded 350°C. At such high temperatures any deposited or desorbed material in the transfer line could be released. It can be assumed that the released material nucleated during cooling and dilution in the full dilution tunnel and resulted in high particle concentrations. Such desorption and high concentration of nucleation mode particles was reported in a dedicated study on the influence of the transfer line on particulate emissions [15]. In our study the geometric mean dimeter of these particles was 17–24 nm. Another study with a Euro 4 motorcycle [16] found also such high volatile particles concentration, but when they repeated with an open configuration (i.e. dilution at the tailpipe) no such volatile particles appeared. It still needs to be understood whether these particles are produced from the motorcycle and due to the desorption they increase in size when they cool down at the dilution tunnel or they are an artefact of the sampling lines [17]. Nevertheless, the solid particle emissions > 23 nm were much lower (6.5 times) than the emission limit of the passenger cars (but 2.5 times when considering solid particles > 10 nm). The CLOVE proposal for Euro 7 for passenger cars is 1×10^{11} p/km (for SPN_{10}). CLOVE (Consortium for ultra Low Vehicle Emissions) is the consortium tasked by the European Commission to give guidelines for the upcoming Euro 7 emission standards. The motorcycle exceeded this limit 2.5 times, indicating that the particle number emissions from L-category vehicles will need to be reconsidered.

5. Conclusions

This is one of the first studies of a Euro 5 motorcycle. The gaseous pollutants were half of their respective limits. The solid particle number emissions were 6.5 (23 nm) and 2.5 (10 nm) times lower than the limits of passenger cars (not applicable to motorcycles). The emissions per phase (urban, rural, motorway) parts were also provided. For all pollutants the cold start had the highest contribution, while the motorway part was a significant source of total particles. More research is needed for total particles to ensure that they are not an artefact of the high exhaust gas temperatures and release of deposited materials in the sampling lines.

Acknowledgements

The authors would like to acknowledge the technical support of A. Bonamin, D. Lesueur, and F. Forloni.

Nomenclature

APC	AVL particle counter
CH_4	methane
CO	carbon monoxide
CO_2	carbon dioxide
CPC	condensation particle counter
CVS	constant volume sampler
EEPS	engine exhaust particle sizer
FC	fuel consumption
GTR	global technical regulation
HC	hydrocarbons
NMHC	non-methane hydrocarbons
NO_x	nitrogen oxides
PCRF	particle concentration reduction factor
PN	particle number
PTW	powered two-wheelers
SPN	solid particle number
TPN	total particle number
WMTC	world harmonized motorcycle test cycle

Bibliography

[1] ACEM Association Des Constructeurs Européens de Motocycles. Market Data. Available at: https://www.acem.eu/Market-Data 2019

[2] EUROPEAN COMMISSION. Directorate General for Mobility and Transport *EU Transport in Figures: Statistical Pocketbook.* 2018. ISBN 978-92-79-73951-4

[3] DOROCKI, S. Changes in the market of two and three-wheeled motor vehicles in Europe at the beginning of the 21st century. *EBER.* 2018, **6**, 175-193. https://doi.org/10.15678/EBER.2018.060110

[4] KONTSES, A., NTZIACHRISTOS, L., ZARDINI, A.A. et al. Particulate emissions from L-category vehicles towards Euro 5. *Environmental Research.* 2020, **182,** 109071. https://doi.org/10.1016/j.envres.2019.109071

[5] NTZIACHRISTOS, L., VONK, W.A., PAPADOPOULOS, G. et al. Effect study of the environmental step Euro 5 for L-category vehicles. *European Commission*. 2017, ISBN 978-92-79-70203-7.

[6] GIECHASKIEL, B., ZARDINI, A.A., LÄHDE, T. et al. Particulate emissions of Euro 4 motorcycles and sampling considerations. *Atmosphere.* 2019, **10,** 421. https://doi.org/10.3390/atmos10070421

[7] CHIANG, H.-L., HUANG, P.-H., LAI, Y.-M. et al. Comparison of the Regulated Air Pollutant Emission Characteristics of Real-World Driving Cycle and ECE cycle for motorcycles. *Atmospheric Environment.* 2014, **87**, 1-9. https://doi.org/10.1016/j.atmosenv.2013.12.031

[8] GIECHASKIEL, B., CRESNOVERH, M., JÖRGL, H. et al. Calibration and accuracy of a particle number measurement system. *Measurement Science and Technology.* 2010, **21**, 045102. https://doi.org/10.1088/0957-0233/21/4/045102

[9] AMANATIDIS, S., NTZIACHRISTOS, L., GIECHASKIEL, B. et al. Evaluation of an oxidation catalyst ("catalytic stripper") in eliminating volatile material from combustion aerosol. *Journal of Aerosol Science.* 2013, **57**, 144-155. https://doi.org/10.1016/j.jaerosci.2012.12.001

[10] GIECHASKIEL, B., MELAS, A.D., LÄHDE, T. et al. Non-volatile particle number emission measurements with catalytic strippers: a review. *Vehicles.* 2020, **2**, 342-364. https://doi.org/10.3390/vehicles2020019

[11] LAHDE, T., GIECHASKIEL, B., MARTINI, G. Development of measurement methodology for sub 23 nm particle number (PN) measurements. *SAE Technical Paper* 2020-01-2211. 2020. https://doi.org//10.4271/2020-01-2211

[12] TSAI, J.-H., HUANG, P.-H., CHIANG, H.-L. Air pollutants and toxic emissions of various mileage motorcycles for ECE driving cycles. *Atmospheric Environment.* 2017, **153,** 126-134. https://doi.org/10.1016/j.atmosenv.2017.01.019

[13] VOJTISEK-LOM, M., ZARDINI, A.A., PECHOUT, M. et al. A miniature portable emissions measurement system (PEMS) for real-driving monitoring of motorcycles. *Atmospheric Measurement Techniques.* 2020, **13**, 5827-5843. https://doi.org/10.5194/amt-13-5827-2020

[14] MURENA, F., PRATI, M.V., COSTAGLIOLA, M.A. Real driving emissions of a scooter and a passenger car in Naples city. *Transportation Research Part D: Transport and Environment* 2019, **73**, 46-55. https://doi.org/10.1016/j.trd.2019.06.002

[15] YANG, J., PHAM, L., JOHNSON, K.C. et al. Impacts of exhaust transfer system contamination on particulate matter measurements. *Emission Control Science and Technology.* 2020, **6**, 163-177. https://doi.org/10.1007/s40825-020-00155-1

[16] GIECHASKIEL, B. Gaseous and particulate Emissions of a Euro 4 motorcycle and effect of driving style and open or closed sampling configuration. *Sustainability.* 2020, **12**, 9122. https://doi.org/10.3390/su12219122

[17] GIECHASKIEL, B. Effect of sampling conditions on the sub-23 nm nonvolatile particle emissions measurements of a moped. *Applied Sciences.* 2019, **9,** 3112. https://doi.org/10.3390/app9153112

Barouch Giechaskiel, PhD – Sustainable Transport Unit, European Commission, Joint Research Centre (JRC), Italy.
e-mail: *barouch.giechaskiel@ec.europa.eu*

Anastasios Melas, PhD – Sustainable Transport Unit, European Commission, Joint Research Centre (JRC), Italy.
e-mail: *anastasios.melas@ec.europa.eu*

Article citation info:
PAZURA, K., ORKISZ, M. Experimental determination of compressor map of the DGEN 380 engine compressor using the WESTT CS/BV turbine engine simulator. *Combustion Engines*. 2021, **185**(2), 26-31. https://doi.org/10.19206/CE-138835

Karolina PAZURA
Marek ORKISZ

Experimental determination of compressor map of the DGEN 380 engine compressor using the WESTT CS/BV turbine engine simulator

Currently aviation focuses mainlly on increasing the economy and ecology of engines. Production of NO_x, CO_2 and SO_2 adversaly impacts the environment. Parallel goal to minimize SFC to achieve both lower: emission and mission costs. The optimization of components is thus very important. One of the ways of optimizing cycle is doing that based on compressor maps. However it is very expensive to plot one since experimental work needs to be done. The aim of this article is to present a methodology of creating compressor map based on ENGINE ANALOGY. There was used the virtual bench WESTT CS/BV for tests to receive pressure ratio and mass flow of DGEN 380 for three different values of flight speed and altitude, while the rotational speed was changed. The construction similarity of CFM 56-5B and APS 3200 gives the opportunity to plotted compressor maps using the engine analogy without the need for an experiment or using the virtual bench.

Key words: *compressor map, engine bench, turbofan jet engine, turbine engine, mass flow rate*

1. Introduction

The aim of this article is to present a methodology of creating compressor map based on engine analogy. This alternative is using given data of any engine to plotted compressor map based on ready to use characteristic of another engine. Before this method will be described first it is worth to mention there is a huge number of methods for obtain compressor map.

In a multi-stage process of turbine engine design the mathematical modeling of its parameters is used. It starts with simply thermo-gas dynamic calculations and ends with 3D analysis of flow through the components. During the design phase of compressor its characteristic is important. Creating compressor map based on test data is costly and time consuming. It is also important to be aware that these characteristics are really error prone. Specific overview of curve fitting methods for a centrifugal compressor and turbine characteristics is presented by Moraal and Kolmanovsky [9].

There are many methods of determining characteristic and one of them is cubic approximation for speed lines from the Moore Greitzer Model used in article of Drummond and Davison [2].

The second possibility is scaling procedure described by Kurzke and Riegler [4]. This method uses the similarity of the pressure ratio value of the existing map and the new one that will be plotted.

Another way to changing the line of characteristic is modification of diffuser geometric or variable guide vanes which is described by Hunzinker, Dickmann and Emmrich [3]. This also gives the inexpensive to manufacture and compact design.

Availability and accuracy of compressor map allowed calculating the loads of turbine. Kurzke [5] mentions that one percent error in calculations in fan or HP compressor efficiency provides to one percent error in specific fuel consumption of a turbofan. The engine manufacturers reveal only a part of information that is why data collection of components, which are necessary to build model of engine to make this kind of simulation, is impossible.

Due to fact that modeling of compressor map is problematic there is a lot of articles and diploma thesis that dealing with this problem. Ismail and Bhinder [6] used tables to preserve the shape of characteristics as linear and Lagrangian interpolation technique to determine the values of the performance parameters for an arbitrarily selected point on the compressor map. El-Gammal in 1991 publicized diploma in which he described, developed by himself, the criteria and algorithm for a compressor characteristic for linear model [7]. For non-linear models Sieros, Stamatis and Mathioudakis [8] used analytical functions to model map of different types of design. They were even used a genetic algorithm to determine the unknown coefficients of third-order equations relating the mass flow, the pressure ratio, and the isentropic efficiency by Kong, Kho and Ki [10, 11]. Gravdahl and Egeland [12] described an analytical method to approximate the compressor characteristic based on energy considerations and geometry of the compressor. Their method modifies the ideal characteristic and including friction losses. Mentioned ideas were presented by Gravdahl, Willems, Jager and Egeland as experimental validation [13].

In this article is described another yet methods of plotted compressor map. Engine analogy is an alternative, which allows in a simply way, to get necessary information about engine components and their operating range.

The turbine engines are used as propulsion of airplane. The main construction with one duct consists of: inlet, compressor, combustion chamber, turbine and nozzle through which air flows. During the development of more efficiency ones, there is a turbofan with high-bypass ratio. This construction has a fan with huge diameter between the inlet and the compressor and divided duct: internal and external one, which allows to get more thrust.

2. Compressor map

2.1. Use of compressor map

Another way to get engine with high efficiency is using the compressor map. It allows finding the best conditions of compressor cooperation with the other components and shows stall margin. During the engine crosses mentioned

Received 1 May 2021; Received in revised form 24 May 2021; Accepted 11 June 2021
Available online 11 June 2021

stall margin, there is dangerous situation, in which the hot flow begin moving in the opposite direction getting through the blade clearance and this results in air is sucked from the combustion chamber.

The parameters using to plotting the characteristic are reduced parameter, which are closely related with compressor performance. Reducing of parameters is necessary, because then the independence of the characteristic from environmental conditions is obtained. The change of ambient temperature causes the change of mass flow, pressure ratio and efficiency.

The compressor maps may be compared with each other only in the case of similar construction. That means map of axial compressor could be compared only with another axial compressor, not with centrifugal one. The characteristic of radial compressor is milder then characteristic of axial compressor. It means that axial compressor is more sensitive to mass flow changing. Especially dangerous is decrease of mass flow compared with the calculated value, because then occurs boundary-layer separation what results the vortex field. In this situation the pressure is starting to be lower in the component and causes the appearance of swirl between blade space in external duct, pressure pulsation and decrease of efficiency which all make up the compressor unstable work.

The characteristic of axial and radial compressor are on Fig. 1 and Fig. 2.

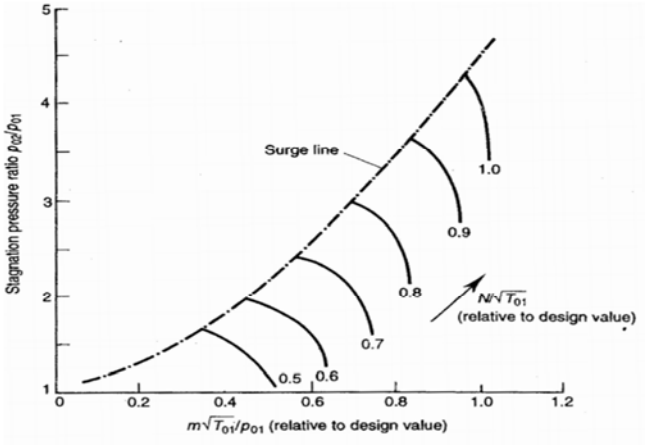

Fig. 1. Axial compressor map with reduced parameters [1]

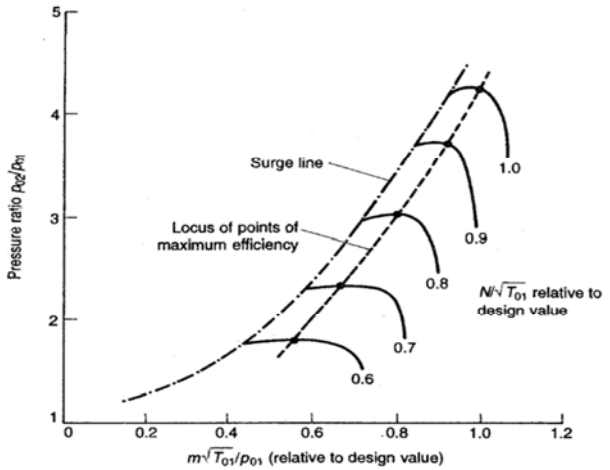

Fig. 2. Centrifugal compressor map with reduced parameters [1]

2.2. Receiving a compressor map

Through the use of virtual engine test bench WESTT CS/BV which is a simulator of DGEN 380 engine, there was the opportunity to get data like: efficiency and pressure ratio for fan and compressor. All parameters were getting for flight velocity V = 0 Ma, V = 0.2 Ma and V = 0.44 Ma and also for flight altitude H = 0 m, H = 2000 m and H = 7000 m.

Virtual test bench allows simulating the work of engine through the change of internal parameters like: pressure and temperature in inlet but the collected parameters had to be reduced.

Another way to get compressor map is apply engine analogy. Plotted characteristic of DGEN 380 may be using for plotting compressor map of another engine provided that the construction of component is similar.

2.3. DGEN 380, APS 3200, CFM 56-5B- data

The choice of DGEN 380 was imposed by virtual engine test bench, which is available in Rzeszow University of Technology in Department of Aircrafts and Aircraft Engines. However the APS 3200 and the CFM 56-5B was not random choice. Mentioned engine analogy to be used correctly requires the preservation of construction similarity. The construction of fan in CFM 56-5B is similar to construction of fan in DGEN 380 and the construction of compressor in APS 3200 is the same in DGEN 380- both are centrifugal one.

Table 1.Parameter of DGEN 380

Engine	Parameter	Unit	Value
DGEN 380	Mass flow	$\frac{kg}{s}$	13
	Pressure ratio	–	5.3
APS 3200	Mass flow	$\frac{kg}{s}$	2.2
	Pressure ratio	–	8
CFM 56-5B	Mass flow	$\frac{kg}{s}$	400
	Pressure ratio	–	1.6

2.4. Preparation of data

As mentioned the compressor map is plotted in reduced parameters. That is way the charts have got reduced mass flow. To get that the equation (1) was used.

$$\dot{m}_r = \dot{m} \cdot \frac{101325}{p_0} \cdot \sqrt{\frac{T_0}{288.15}} \tag{1}$$

Based on reduced mass flow and pressure ratio the points have been plotted on the chart. Both charts are for components of DGEN 380 for three different altitudes (0 m, 2000 m, 7000 m) and velocities (0 Ma, 0.2 Ma, 0.44 Ma) of flight.

Can be observed lines of centrifugal compressor (Fig. 4) of DGEN 380 do not show characteristic division into three groups like the lines of fan of DGEN 380 (Fig. 3). This is due to the fact that flow in the compressor is more stable because of the fan preceding it and stabilizes parameters of flow. The similarity of these lines is caused by the centrifugal compressor show less susceptibility to crossed stall margin.

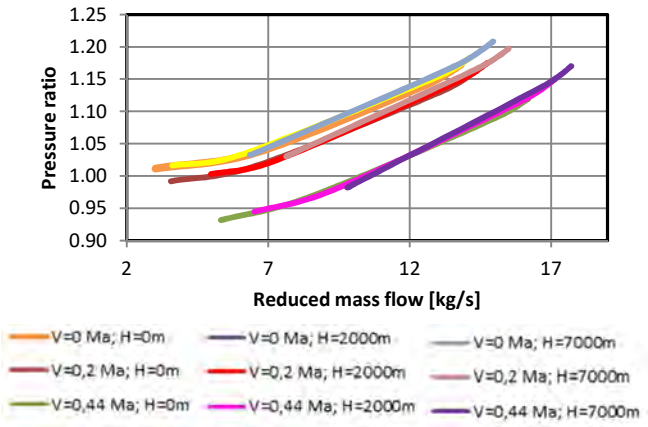

Fig. 3. Compressor map for fan of DGEN 380

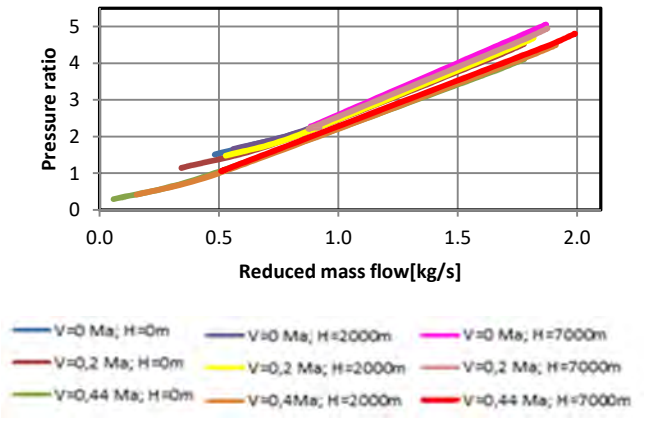

Fig. 4. Compressor map for centrifugal compressor of DGEN 380

2.5. Engine analogy

As was mentioned before, there is possibility to plot compressor map of another engine based on obtained compressor map DGEN 380 only if similarity of construction is preserved. It is called engine analogy.

The first step was determined absolute parameters of pressure ratio and mass flow. Absolute parameter of pressure ratio is value of pressure ratio read when collecting data is divided by maximal value of sea-level pressure ratio. While absolute parameter of mass flow is value of mass flow read when collecting data is divided by maximal value of sea-level mass flow. The equation (2) and (3) was used to carry out such calculation.

$$\pi_{abs} = \frac{\pi}{\pi_{max}} \tag{2}$$

$$\dot{m}_{abs} = \frac{\dot{m}}{\dot{m}_{max}} \tag{3}$$

Each absolute parameter need to be multiply by pressure ratio or mass flow of suitable engine and then may be plotted. To get all of the points to plotted compressor map of fan CFM 56-5B and compressor APS 3200 there was wrote the program on MATLAB.

For CFM 56-5B obtained parameters by using program, are showed in Tables 4-12. All of them are determined for different rotational velocity and it can be seen despite the change of the value of rotational velocity the parameters on the last rows are identical or the same.

Table 4. Parameter of CFM 56-5B V = 0 Ma, H = 0 m

	Pressure ratio	Reduced mass flow	Absolute pressure ratio	CFM 56-5B fan pressure ratio	Absolute mass flow	CFM 56-5B fan mass flow
Idle-0%	1.01	3.03	0.86	1.38	0.22	87.83
30%	1.04	6.64	0.89	1.42	0.48	192.46
Cruise- 43%	1.14	12.52	0.97	1.56	0.91	362.90
Max Cont.- 74%	1.17	13.77	1.00	1.60	1.00	399.13
Top-100%	1.17	13.8	1.00	1.60	1.00	400.00

Table 5. Parameter of CFM 56-5B V = 0.2 Ma, H = 0 m

	Pressure ratio	Reduced mass flow	Absolute pressure ratio	CFM 56-5B fan pressure ratio	Absolute mass flow	CFM 56-5B fan mass flow
Idle-0%	0.99	3.56	0.85	1.35	0.26	103.19
30%	1.02	6.59	0.87	1.39	0.48	191.01
Cruise- 43%	1.13	13.14	0.97	1.55	0.95	380.87
Max Cont.- 74%	1.16	14.37	0.99	1.59	1.04	416.52
Top-100%	1.16	14.37	0.99	1.59	1.04	416.52

Table 6. Parameter of CFM 56-5B V = 0.44 Ma, H = 0 m

	Pressure ratio	Reduced mass flow	Absolute pressure ratio	CFM 56-5B fan pressure ratio	Absolute mass flow	CFM 56-5B fan mass flow
Idle-0%	0.93	5.33	0.79	1.27	0.39	154.49
30%	0.97	8.49	0.83	1.33	0.62	246.09
Cruise- 43%	1.09	15.15	0.9	1.49	1.10	439.13
Max Cont.- 74%	1.12	16.2	0.96	1.53	1.17	469.57
Top-100%	1.12	16.19	0.96	1.53	1.17	469.28

Table 7. Parameter of CFM 56-5B V = 0 Ma, H = 2000 m

	Pressure ratio	Reduced mass flow	Absolute pressure ratio	CFM 56-5B fan pressure ratio	Absolute mass flow	CFM 56-5B fan mass flow
Idle-0%	1.02	3.61	0.87	1.39	0.26	104.64
30%	1.03	6.00	0.88	1.41	0.43	173.91
Cruise- 43%	1.15	13.06	0.98	1.57	0.95	378.55
Max Cont.- 74%	1.18	14.12	1.01	1.61	1.02	409.28
Top-100%	1.18	14.12	1.01	1.61	1.02	409.28

Table 8. Parameter of CFM 56-5B V = 0.2 Ma, H = 2000 m

	Pressure ratio	Reduced mass flow	Absolute pressure ratio	CFM 56-5B fan pressure ratio	Absolute mass flow	CFM 56-5B fan mass flow
Idle-0%	1.00	4.98	0.85	1.37	0.36	144.35
30%	1.02	7.20	0.87	1.39	0.52	208.70
Cruise- 43%	1.15	13.76	0.98	1.57	1.00	398.84
Max Cont.- 74%	1.18	14.76	1.01	1.61	1.07	427.83
Top-100%	1.17	14.75	1.00	1.60	1.07	427.54

Table 9. Parameter of CFM 56-5B V = 0.44 Ma, H = 2000 m

	Pressure ratio	Reduced mass flow	Absolute pressure ratio	CFM 56-5B fan pressure ratio	Absolute mass flow	CFM 56-5B fan mass flow
Idle-0%	0.94	6.52	0.80	1.29	0.47	188.99
30%	0.98	9.29	0.84	1.34	0.67	269.28
Cruise- 43%	1.12	16.03	0.96	1.53	1.16	464.64
Max Cont.- 74%	1.15	17.13	0.98	1.57	1.24	496.52
Top-100%	1.15	17.13	0.98	1.57	1.24	496.52

Table 10. Parameter of CFM 56-5B V = 0 Ma, H = 7000 m

	Pressure ratio	Reduced mass flow	Absolute pressure ratio	CFM 56-5B fan pressure ratio	Absolute mass flow	CFM 56-5B fan mass flow
Idle-0%	1.03	6.37	0.88	1.41	0.46	184.64
30%	1.03	6.43	0.88	1.41	0.47	186.38
Cruise- 43%	1.17	13.58	1.00	1.60	0.98	393.62
Max Cont.- 74%	1.21	14.96	1.03	1.65	1.08	433.62
Top-100%	1.21	14.96	1.03	1.65	1.08	433.62

Table 11. Parameter of CFM 56-5B V = 0.2 Ma, H = 7000 m

	Pressure ratio	Reduced mass flow	Absolute pressure ratio	CFM 56-5B fan pressure ratio	Absolute mass flow	CFM 56-5B fan mass flow
Idle-0%	1.03	7.74	0.80	1.41	0.56	224.35
30%	1.03	7.65	0.80	1.41	0.55	221.74
Cruise- 43%	1.17	14.47	0.86	1.60	1.05	419.42
Max Cont.- 74%	1.20	15.50	0.88	1.64	1.12	449.28
Top-100%	1.20	15.50	0.88	1.64	1.12	449.28

Table 12. Parameter of CFM 56-5B V = 0.44 Ma, H = 7000 m

	Pressure ratio	Reduced mass flow	Absolute pressure ratio	CFM 56-5B fan pressure ratio	Absolute mass flow	CFM 56-5B fan mass flow
Idle-0%	0.98	9.86	0.60	1.34	0.71	285.80
30%	0.98	9.80	0.60	1.34	0.71	284.06
Cruise- 43%	1.14	16.78	0.80	1.56	1.22	486.38
Max Cont.- 74%	1.17	17.72	0.84	1.60	1.28	513.62
Top-100%	1.17	17.72	0.84	1.60	1.28	513.62

All obtained parameters are plotted in Fig. 5.

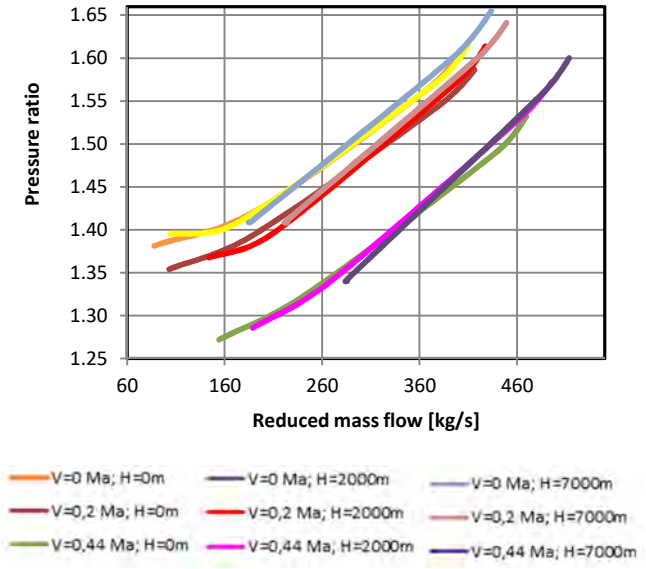

Fig. 5. Compressor map of fan CFM 56-56

The compressor map of fan CFM 56-5B has got the characteristic division into three groups like the lines of fan of DGEN 380 are present. It is caused by unstable parameters of flow, exactly like in the compressor map of DGEN 380 fan.

For APS 3200 obtained parameters by using program, are showed in Tables 13–21. As in the CFM 56-5B the all of them are determined for different rotational velocity. In this case can be seen the parameters on the last two rows are also identical or the same despite the change of value of rotational.

Table 13. Parameter of APS 3200 V = 0 Ma, H = 0 m

	Pressure ratio	Reduced mass flow	Absolute pressure ratio	APS 3200 fan pressure ratio	Absolute mass flow	APS 3200 fan mass flow
Idle-0%	1.51	0.48	0.33	2.63	0.27	0.60
30%	2.38	0.96	0.52	4.15	0.55	1.20
Cruise- 43%	4.18	1.62	0.91	7.29	0.92	2.02
Max Cont.- 74%	4.58	1.76	1.00	7.98	1.00	2.19
Top-100%	4.59	1.76	1.00	8.00	1.00	2.20

Table 14. Parameter of APS 3200 V= 0.2 Ma, H = 0 m

	Presure ratio	Reduced mass flow	Absolute pressure ratio	APS 3200 fan pressure ratio	Absolute mass flow	APS 3200 fan mass flow
Idle-0%	1.14	0.34	0.25	1.99	0.19	0.43
30%	1.84	0.75	0.40	3.21	0.42	0.93
Cruise- 43%	4.11	1.63	0.90	7.17	0.93	2.04
Max Cont.- 74%	4.52	1.78	0.98	7.88	1.01	2.22
Top-100%	4.52	1.78	0.98	7.88	1.01	2.22

Table 15. Parameter of APS 3200 V = 0.44 Ma, H = 0 m

	Pressure ratio	Reduced mass flow	Absolute pressure ratio	APS 3200 fan pressure ratio	Absolute mass flow	APS 3200 fan mass flow
Idle-0%	0.29	0.06	0.06	0.51	0.03	0.07
30%	0.89	0.43	0.19	1.54	0.24	0.54
Cruise- 43%	3.70	1.62	0.81	6.45	0.92	2.02
Max Cont.- 74%	4.11	1.78	0.90	7.16	1.01	2.22
Top-100%	4.11	1.78	0.89	7.16	1.01	2.22

Table 16. Parameter of APS 3200 V = 0 Ma, H = 2000 m

	Pressure ratio	Reduced mass flow	Absolute pressure ratio	APS 3200 fan pressure ratio	Absolute mass flow	APS 3200 fan mass flow
Idle-0%	1.66	0.45	0.36	2.89	0.26	0.56
30%	2.22	0.70	0.48	3.87	0.40	0.88
Cruise- 43%	4.36	1.34	0.95	7.60	0.76	1.67
Max Cont.- 74%	4.71	1.43	1.03	8.21	0.81	1.79
Top-100%	4.71	1.43	1.03	8.21	0.81	1.79

Table 17. Parameter of APS 3200 V = 0.2 Ma, H = 2000 m

	Pressure ratio	Reduced mass flow	Absolute pressure ratio	APS 3200 fan pressure ratio	Absolute mass flow	APS 3200 fan mass flow
Idle-0%	1.48	0.42	0.32	2.57	0.24	0.53
30%	2.03	0.67	0.44	3.54	0.38	0.83
Cruise- 43%	4.35	1.37	0.95	7.58	0.78	1.71
Max Cont.- 74%	4.68	1.46	1.02	8.16	0.83	1.82
Top-100%	4.68	1.46	1.02	8.16	0.83	1.82

Table 18. Parameter of APS 3200 V = 0.44 Ma, H = 2000 m

	Pressure ratio	Reduced mass flow	Absolute pressure ratio	APS 3200 fan pressure ratio	Absolute mass flow	APS 3200 fan mass flow
Idle-0%	0.42	0.12	0.09	0.72	0.07	0.16
30%	1.00	0.40	0.22	1.75	0.23	0.50
Cruise- 43%	4.07	1.41	0.89	7.09	0.80	1.76
Max Cont.- 74%	4.50	1.54	0.98	7.83	0.87	1.92
Top-100%	4.49	1.53	0.98	7.83	0.87	1.92

Table 19. Parameter of APS 3200 V = 0 Ma, H = 7000 m

	Pressure ratio	Reduced mass flow	Absolute pressure ratio	APS 3200 fan pressure ratio	Absolute mass flow	APS 3200 fan mass flow
Idle-0%	2.28	0.39	0.50	3.97	0.22	0.49
30%	2.29	0.39	0.50	4.00	0.22	0.49
Cruise- 43%	4.54	0.75	0.99	7.91	0.42	0.93
Max Cont.- 74%	5.05	0.83	1.10	8.80	0.47	1.03
Top-100%	5.05	0.82	1.10	8.80	0.47	1.03

Table 20. Parameter of APS 3200 V = 0.2 Ma, H = 7000 m

	Pressure ratio	Reduced mass flow	Absolute pressure ratio	APS 3200 fan pressure ratio	Absolute mass flow	APS 3200 fan mass flow
Idle-0%	2.24	0.39	0.49	3.91	0.22	0.49
30%	2.21	0.39	0.48	3.85	0.22	0.48
Cruise- 43%	4.60	0.78	1.00	8.01	0.44	0.97
Max Cont.- 74%	4.94	0.83	1.08	8.62	0.47	1.03
Top-100%	4.94	0.83	1.08	8.61	0.47	1.03

Table 21. Parameter of APS 3200 V = 0.44 Ma, H = 7000 m

	Pressure ratio	Reduced mass flow	Absolute pressure ratio	APS 3200 fan pressure ratio	Absolute mass flow	APS 3200 fan mass flow
Idle-0%	1.10	0.23	0.24	1.91	0.13	0.29
30%	1.06	0.23	0.23	1.85	0.13	0.28
Cruise- 43%	4.44	0.82	0.97	7.73	0.47	1.03
Max Cont.- 74%	4.80	0.88	1.05	8.37	0.50	1.10
Top-100%	4.80	0.88	1.05	8.37	0.50	1.10

All obtained parameters are plotted in Fig.6.

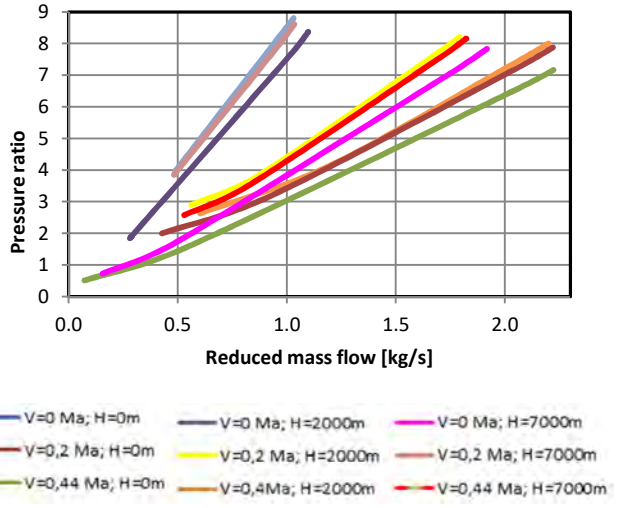

Fig. 6. Compressor map of centrifugal compressor APS 3200

The compressor map of centrifugal compressor of APS 3200 has got characteristic division into three groups like the lines of fan of DGEN 380 and CFM 56-5B. Exactly as in the previous cases it is caused by unstable parameters of flow. Despite the fact this compressor map is plotted based on parameters of compressor in DGEN 380, which is preceded by fan stabilizing the flow, the chart of centrifugal compressor APS 3200 exhibits features of the division into three group, exactly like maps of DGEN 380 fan and CFM 56-5B fan. In fact compressor of APS 3200 is not preceded by any components, which could stabilize the parameters. It means that engine analogy applicable in practice.

3. Conclusion

Obtained data getting by using virtual bench test WESTT CS/BV were tabulated. The mass flow was reduced using equation (1) for data of fan and compressor. Because of that the charts are not dependent on ambient conditions, that were necessary because they have huge impact on parameters of compressor.

Getting data by using virtual bench test allowed plotting characteristic of fan and compressor very accurately. On the compressor map is visible:

– the increase of flight velocity causes: the increase of component mass flow and also when the rotational speed is low it causes low efficiency of both components,
– the increase of altitude flight causes move the lines in stall margin direction,
– stabilized parameters at inlet of components causes greater similarity of lines on the different altitude of flight.

Using MATLAB code and mathematical equations, which are equations of function above lines there is opportunity to plotted compressor map of engines with components with the same construction of compressor or fan. To mapping mentioned characteristic using the engine analogy the reduction of parameters (pressure ratio and mass flow) to Absolute is necessary.

The engine analogy results are correct, what confirms the compressor map of centrifugal compressor of APS 3200. The lines on it are ordered similar to the compressor map of fan DGEN 380. Despite using the equations obtained from the compressor map of DGEN 380, which parameters of flow are stable, the chart of compressor map of centrifugal compressor of APS 3200 do not show characteristics of uniform flow parameters. It is adequate to its construction, because the compressor of APS 3200 is not preceded by any component, which could uniform the parameters.

Obtained functions of lines for the fan and the compressor may be used to preliminary engine design.

Nomenclature

$\dot{m}$	mass flow
$\dot{m}_{max}$	maximal mass flow at sea level
$\dot{m}_{abs}$	absolute mass flow
$\dot{m}_r$	reduced mass flow
π	pressure ratio
π_{max}	maximal pressure ratio an sea-level
π_{abs}	absolute pressure ratio
p_0	ambient pressure
T_0	ambient temperature

Bibliography

[1] SAVARANAMUTTO, H.I.H., ROGERS, G.F.C., COHEN, H. Gas Turbine Theory. 5 edition, *Pearson*, 2013, **178**, 256.

[2] DRUMMOND, C., DAVISON, C.R. Improved compressor maps using approximate solutions to the Moore-Greitzer model. Volume 1: *Aircraft Engine; Ceramics; Coal, Biomass and Alternative Fuels; Controls, Diagnostics and Instrumentation; Education; Electric Power; Awards and Honors*. https://doi.org/10.1115/gt2009-60148

[3] HUNZKIER, R., DICKMANN, H-P., EMMRICH, R. Numerical and experimental investigation of a centrifugal compressor with an inducer casing bleed system. *Proceedings of the Institution of Mechanical Engineers, Part A: Journal of Power and Energy*. 2001, **215**(6), 783-791. https://doi.org/10.1243/0957650011538910

[4] KURZKE, J., RIEGLER, C. A new compressor map scaling procedure for preliminary conceptional design of gas tur-

bines. *Volume 1: Aircraft Engine; Marine; Turbomachinery; Microturbines and Small Turbomachinery*. https://doi.org/10.1115/2000-gt-0006

[5] KURZKE, J. Correlations hidden in compressor maps. *Volume 1: Aircraft Engine; Ceramics; Coal, Biomass and Alternative Fuels; Wind Turbine Technology*. https://doi.org/10.1115/gt2011-45519

[6] ISMAIL, I.H., BHINDER, F.S. Simulation of aircraft gas-turbine engine. ASME, *Journal of Engineering for Gas Turbines and Power*. 1991, 95-99. https://doi.org/10.1115/1.2906536

[7] ELGAMMAL, M.A. An algorithm and criteria for compressor characteristics real time modelling and approximation. ASME. *Journal of Engineering for Gas Turbines and Power.* 1991, 112-117. https://doi.org/10.1115/1.2906517

[8] SIEROS, G., STAMATIS, A., MATHIOUDAKIS, K. Jet engine component maps for performance modelling and diagnosis. AIAA, *Journal of Propulsion and Power*. 1997, **13**(5), 665-674. https://doi.org/10.2514/2.5218

[9] MORAAL, P., KOLMANOSKY, I. Turbocharger modelling for automotive control application. *SAE Technical Paper* 1999-01-0908. 1999. https://doi.org/10.4271/1999-01-0908

[10] KONG, C.D., KHO, S., KI, J.Y. Component map generation of a gas turbine using genetic algorithms. ASME. *Journal of Engineering for Gas Turbines and Power.* 2006, **128**(1), 92-96. https://doi.org/10.1115/1.2032431

[11] KONG, C.D., KI, J.Y. Components map generation of gas turbine engine using genetic algorithms and engine performance deck data. ASME. *Journal of Engineering for Gas Turbines and Power.* 2007, **129**(2), 312-317. https://doi.org/10.1115/1.2436561

[12] GRAVDAHL, J.T., EGELAND, O. Centrifugal compressor surge and speed control. *IEEE Transactions on Control Systems Technology*. 1999, **7**(5), 567-579. https://doi.org/10.1109/87.784420

[13] GRAVDAHL, J.T., EGELAND, O., WILLEMS, F., JAGER B.D.E. Modeling of surge in free-spool centrifugal compressors: Experimental validation. AIAA. *Journal of Propulsion and Power*. 2004, **20**(5), 849-857. https://doi.org/10.2514/1.10052

Karolina Pazura, MEng. – graduate Faculty of Mechanical Engineering and Aeronautics, Rzeszow University of Technology.
e-mail: *k.pazura.kp@gmail.com*

Prof. Marek Orkisz, DSc., DEng. – Faculty of Mechanical Engineering and Aeronautics Rzeszow University of Technology.
e-mail: *mareko@prz.edu.pl*

Article citation info:
BATURA, K.P., WALIGÓRSKI, M. Methodological basis of road acoustic researches. *Combustion Engines*. 2021, **185**(2), 32-38. https://doi.org/10.19206/CE-139159

Karolina Paula BATURA
Marek WALIGÓRSKI

Methodological basis of road acoustic researches

Transport is one of the most burdensome negative sources affecting the natural environment. Long-term exposure of the body to exhaust pollution can cause health problems and, in the worst case, even lead to death. In addition to exhaust emissions, traffic noise is another equally important issue. Due to its nature, variability over time or the design diversity of vehicles in the traffic flow, it is a phenomenon difficult to define. Like exhaust pollution, it affects people's health and quality of life. In addition to its direct impact on the human physical system, it can also cause psychosomatic disorders, which is why a detailed analysis of road noise taking into account the real operation of the vehicle is so important. The paper presents the basic concepts related to the problem of traffic noise in the world, determines the sources of noise in vehicles and the methodology of conducting acoustic road tests. At the final stage of the scientific paper, methods of reducing excessive noise levels in large urban agglomerations were also presented, and the effectiveness of using noise barriers on selected parts of the city road network using proprietary acoustic tests was assessed.

Key words: *acoustic screen, passenger car, combustion engine, health, noise assessment*

1. Introduction

The problem of air pollution by exhaust gases is a global problem that affects all developed countries in economic terms. The development of industry contributes to the increase in the share of road vehicles and thus to the increase of the generated harmful and toxic exhaust components. It is estimated that over 4 million deaths annually are related to the negative impact of exhaust gases on human health [18]. One of the main reasons for excessively high exhaust emission levels is the high proportion of vehicles exceeding the applicable exhaust emission standards. Like exhaust emissions, noise is another source of pollution that has a negative impact on human health. The source of noise with the greatest share in large urban agglomerations is the road noise, which has a negative impact on health, causes deterioration of the functioning of human organs, and affects the mental and emotional state. The impact of noise is a subjective concept, depending on the human sensitivity to noise, age or, for example, gender, it can cause and accelerate fatigue, distraction, headaches, and irritation, which may result in a collision or a serious road accident. Research on traffic noise and noise reduction methods are issues that are taken up by many scientists, both at home and abroad.

The authors of the paper [1] presented measurement methods for the assessment of the acoustic climate and indicated the relationships between urban noise and various aspects of urban planning. On the basis of the obtained results and the conducted analysis, they indicated the possibility of predicting the noise level in a given area depending on the selected urban elements. By modifying these elements, it is possible to reduce noise levels when developing new urban projects.

The negative impact of noise on the human body has been presented in publications [2, 13]. The authors reviewed the literature on the impact of noise on human health, taking into account both direct impact on the hearing organ and non-hearing effects. In the paper [13], a separate chapter was devoted to the impact of noise on the driver's body, focusing on the negative impact of infrasound and vibrations.

In the first part of the paper [3], the authors Bendtsen and Ellebjerg analyzed the relationship between a vehicle speed and generated noise. The analysis was based on the Scandinavian model and the Harmonoise model. In the second part of the publication, the literature was reviewed, and then recommendations for road managers concerning methods of reducing traffic noise in cities were described.

The measurement of traffic noise and the measurement methodology are presented in papers [15, 23]. The publications presented the results of measurements of the obtained measurement points, characterized by the high vehicle intensity, high share of heavy goods vehicles and high noise intensity. Based on the data, the acoustic state was analyzed. The scientific paper [15] presents technical solutions that could reduce the noise level occurring in these areas.

Paszkowski in his work [14] proposed an innovative method of road noise assessment. This method is based on a model representing both quantitative and qualitative noise risk assessment. The basis for noise assessment is the use of the existing quantitative indicators, technology of creating and using acoustic maps. The proposal of noise analysis is also based on the assessment of acoustic sensations by people.

Two mathematical models to determine the sound level were proposed in [17]. Their correctness was checked in the study by comparing the obtained results with the road noise measured directly. The obtained test results were described as relatively consistent. Therefore, the presented models can be used to predict noise on the surface, as their accuracy is in the range of about 1%.

In the discussed works on the problem of traffic noise, the authors took up the above issue by carrying out a literature review, including determining the negative effects of noise on the human and driver's body, determining specific relationships and developing innovative models for determining the noise level. All the authors of the publication noticed the essence of the problem of road noise, thus trying to reduce it to a level that would not adversely affect human health and the life quality.

Received 19 April 2021; Received in revised form 18 June 2021; Accepted 18 June 2021
Available online 19 June 2021

2. Environmental acoustics and sound parameters

Noise is any undesirable sound, which is a subjective feeling of the recipient, which may be perceived in a way that is burdensome or harmful to humans. Two parameters are used to describe the sound: frequency and sound pressure. The *frequency (pitch of the sound)* expressed in hertz [Hz], describes the number of vibrations per unit time – 1 s. The range of sounds received by the human ear is from 20 Hz to 20,000 Hz and is called the *range of audible sounds*. All sounds below 20 Hz (infrasound) and above 20 kHz (ultrasound) are sounds inaudible to humans. The second parameter is the *sound pressure* expressed in Pascals [Pa], which is a small change in the air pressure in which the sound is propagated. Due to the fact that the human ear is able to perceive a very large range of acoustic pressures (from the hearing threshold of 0.00002 Pa up to a pain threshold of 60 Pa), the *acoustic pressure level* is used instead of acoustic pressure, expressed in [dB] – formula (1) [19]. The above relationship is presented on a logarithmic scale, which means that an increase by 3 dB doubles the intensity of the sound.

$$L = 10\log\left(\frac{p^2}{p_0^2}\right) = 20\lg\frac{p}{p_0}\,[\mathrm{dB}] \tag{1}$$

where: p_0 – reference pressure, equal to $2\cdot10^{-5}$ Pa (hearing threshold).

The sounds with frequencies ranging from 1–4 kHz are best perceived by humans. To assess the impact of noise, the frequency correction is implemented by weighting (correction) filters: A (sound level from 20 to 55 dB), B (55–85 dB), C (above 85 dB) and correction D (for aviation noise measurements).

In order to define the intensity of a sound wave – a longitudinal wave propagating in gases, liquids and solids, the concepts of the pitch and loudness of the sound are used. *The sound pitch* is the subjective assessment of the sound frequency. On the other hand, the *loudness of sound*, expressed in sones, is the subjective impression of receiving the sound of a given intensity. It consists in comparing the received sound with the model sound (1000 Hz). The loudness level of a sound is a phenomenon that indicates that the sound has a loudness level of *n* sones when its loudness is equal to a simple sound whose frequency is 1000 Hz and the sound pressure is *n* dB. Another acoustic term is the *acoustic power*, which is the amount of energy emitted by a sound source. The range of the acoustic power is within the range from 10^{-9} W to 10^{7} W. In order to facilitate the comparison of two different noise sources, the concept of a *power level* is used – formula (2), with which the concept of *sound intensity* is related – formula (3), i.e. the direction of acoustic wave propagation (the ratio of the acoustic power of the sound wave to the surface of propagation of this wave) [19].

$$L_{N1} = 10\log\frac{N}{N_0}\,[\mathrm{dB}] \tag{2}$$

where: N_0 – the reference sound power, equal to $1\cdot10^{-12}$ W.

$$L = 10\log\frac{I}{I_0}\,[\mathrm{dB}] \tag{3}$$

where: I_0 – the reference sound intensity, equal to $1\cdot10^{-12}$ W·m^{-2}.

3. Assessment of the traffic noise level

3.1. Noise assessment indicators

Traffic noise, as one of the most annoying types of noise, especially in urban agglomerations, has a negative impact on the shaping of the acoustic climate. Its variability over time is only one of the measurement problems, so it is important to use acoustic assessment indicators that take into account all data, such as the time of day/night, land development, demographic data or quantitative data of the population. The following values are used for the noise assessment (the reference time T can be freely adopted, e.g. 15 min, 1 h, 16 h, 8 h) [14]:

- L_A [dB] – the sound level using the A correction characteristic – formula (1).
- L_{AeqD} – the equivalent sound level for day time from 6 a.m. to 10 p.m.,
- L_{AeqN} – the equivalent sound level for night time from 10 p.m. to 6 a.m. – formula (4).

$$L_{Aeq} = 10\log\left[\frac{1}{t_2-t_1}\int_{t_1}^{t_2}\left(\frac{P_A}{P_0}\right)^2 dt\right],\,[\mathrm{dB}] \tag{4}$$

where: $(t_2–t_1)$ – the reference time interval T, P_A – the instantaneous value of the sound pressure, [Pa], P_0 – the reference sound pressure, equal to $2\cdot10^{-5}$, [Pa].

Directive 2002/49/WE defines the indicators used for the long-term assessment of the noise level [9, 14]:

- L_{DWN} – day-evening-night level, to determine all days of the year, where noise determinations must be specified for the time of day L_D (6 a.m.–6 p.m.), L_W (6 p.m.–10 p.m.) and L_{N2} (10 p.m.–6 a.m.) – formula (5),

$$L_{DWN} = 10\log\frac{1}{24}\left(12\cdot10^{\frac{L_D}{10}} + 4\cdot10^{\frac{L_W+5}{10}} + 8\cdot10^{\frac{L_{N2}+10}{10}}\right)[\mathrm{dB}] \tag{5}$$

- L_{N2} – night level, used to determine all nights of the year.

In addition to the basic noise assessment indicators, there are also complex indicators:

- L_{MZHk} – for the relative percentage of population of an area with high noise levels,
- T_{MZH} – for determining the ratio of the surface with excess noise levels to the total surface,
- M – specifying the amount of exceeding noise standards and the number of people exposed to high noise levels.

Permissible noise standards in Poland are included in the Regulation of the Minister of the Environment on permissible noise levels in the environment (Journal of Laws 2014, item 112). This regulation defines the permissible A-sound levels depending on the purpose of the area, both for the daytime L_{AeqD} and nighttime L_{AeqN}.

3.2. Factors influencing on traffic noise

The problem of road noise is a common phenomenon, to which mainly areas close to communication networks are exposed. A characteristic feature of road noise is the variability of noise sources (different designs, structure and vehicles categories) and the variability of traffic intensity. The main sources of noise generated by vehicles are [5]:

- operation of the drive source and its components (noise dominating during vehicle acceleration, operation at low gears),
- damage and hitting of body parts,

– noise generated at the contact of the tire with the road surface (prevailing at high speeds),
– aerodynamic noise.

Considering the noise generated by vehicles in the traffic flow, the following causes of its formation can be distinguished [5]:
– heavy traffic,
– large share of heavy duty vehicles,
– too high vehicle speeds,
– bad technical condition of vehicles,
– bad condition and wrong type of a road surface,
– lack of prioritization of the road network,
– large share of national roads running through residential areas and cities,
– no clear regulations regarding spatial planning taking into account the noise criterion.

However, in order to assess the noise level caused by the traffic flow on the road, many variables should be taken into account, including [20]:
– the number of vehicles passing in the adopted time unit,
– share of the number of intersections with traffic lights and taking into account the duration of the cycle of light signal change,
– type of vehicles and their technical condition,
– type and technical condition of the road surface,
– speed limits,
– the number of lanes,
– the location distance from the urban agglomeration.

3.3. Methods of traffic noise determination

Three measurement methods are used to determine the acoustic climate that takes into account traffic [11]:
– continuous measurement method, used for road noise tests (the direct method),
– a method of measuring single acoustic events, used in the measurement of the road, rail and air noise, in periodic tests (the indirect method),
– measurement method using sampling (the direct method).

In the method of direct continuous measurements, the measurement is performed for a minimum of 3 consecutive days. In this case, noise indicators should be determined on the basis of at least one continuous measurement for the selected road section. The obtained values are the result of multi-day or many-hour observations, while the values obtained at the moment when the requirements for atmospheric conditions were not met (the average wind speed not greater than 5 m/s, no precipitation) are eliminated from the entire period. The method of single acoustic events is based on measurement of a single event, which may be, for example, one journey of a vehicle, train, or flight of an airplane. The average exposure level is determined, also taking into account the standard deviation. The last method, the sampling method, consists in determining the equivalent sound level. When using this method, the value of traffic intensity on the tested section should not exceed 25% for each hour, and the share of heavy vehicles should not exceed 10%. This method is used when the share of all vehicles on the road does not exceed 300 units in 1 hour [11, 14].

4. Exposure to noise and its negative effects on human health

Noise sensitivity is a subjective feeling for every human being. Due to the harmful effects on the human body, noise can be divided into three areas:
– directly affecting the organ of hearing,
– indirectly affecting the nervous system and psyche,
– affecting other organs by reflex [13].

The harmfulness of noise depends on many factors, such as the intensity and sounds frequency, impact time, the nature of changes in sounds over time and inaudible components [13]. Long-term exposure to noise at the level of 70–80 dB, characterized by the dominance of medium and high frequencies, a short hearing renewal phase and impulse noise are features that may have a harmful effect on the human body.

4.1. Direct impact of noise on the human hearing organ

The hearing organ is the organ most exposed to noise in the human body. Due to its structure, prolonged exposure to noise can lead to irreversible changes in Corti's organ and increasing the hearing threshold. This process is a long-term phenomenon and takes place in a phased manner. The change in the hearing threshold begins after approximately 3–5 years of continuous exposure to noise and applies to higher frequencies at the level of 4 kHz, then until 10 years it covers the frequency at the level of 2 kHz. Complete and advanced deafness can occur after 10–20 years of exposure to excessively high noise levels. The consequence of shifting the hearing threshold may be speech incomprehensibility, caused by shifting understanding beyond the area of audible sounds. Figure 1 presents the area of audible sounds, music and speech of a healthy person as well as the area of audible sounds, music and speech of a person with hearing impairment. Particularly dangerous types of noise that can cause sudden and immediate hearing loss are impulse noises, characterized by a sharp increase to levels above 130 dB. Due to the impact on humans, audible noises can be divided into 5 groups:
– below 35 dB – harmless, sometimes causing nervousness, disrupting during work;
– 35–70 dB – causing nervous system fatigue, lowering the sensitivity of sight, hindering understanding speech and communication, adversely affecting falling asleep and resting;
– 70–85 dB – negatively affecting the work performance, harmful to health, causing hearing damage, headaches and nervous disorders;
– 85–130 dB – causing numerous disturbances, incl. cardiovascular and digestive systems, making it impossible to understand speech even from a distance of 0.5 m;
– over 130 dB – affecting the vibrations of some internal organs of a human being and causing their diseases, imbalance, nausea, changes in the content of components in the blood [13].

a)

b)

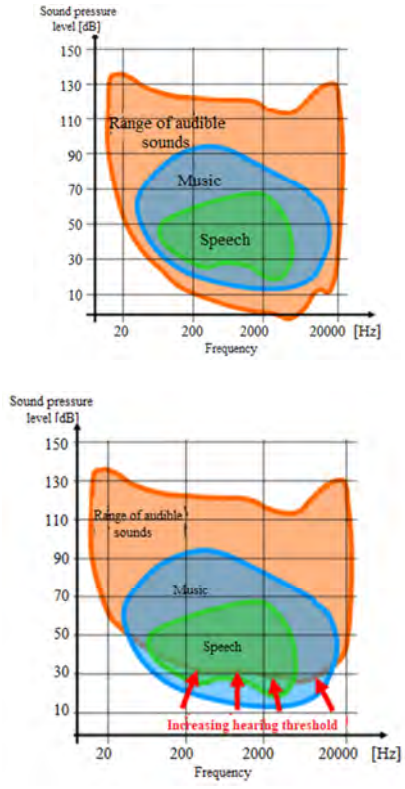

Fig. 1. The range of audible sounds, music and speech: a) a healthy person, b) a person with hearing impairment [24]

4.2. Non-auditory effects of noise on humans

In addition to the direct impact of noise on the hearing organ, there are also non-auditory effects, concerning both human health and well-being. The first group of no-auditory effects are psychological disorders: disturbances in cognitive and memory processes, difficulties in focusing attention, feeling tense, irritability, headaches and difficulties in focusing attention while performing work [2, 6]. The second group are physiological problems related to the proper functioning of the systems: cardiovascular (narrowing of blood vessels, arterial hypertension), digestive (possible ulcer), endocrine (hormonal changes) and nervous system. In addition to the effects described above, exposure to noise also causes psychological problems and early aging. Being in noise at the level above 75 dB triggers motor reflexes, e.g. contractions of: muscle, neck and head. After briefly exceeding this limit (75 dB), the electrical resistance of the skin changes, the rhythm of breathing changes and the circulatory system reacts differently (contraction of blood vessels and the increase in circulatory resistance). On the other hand, being in an acoustic climate of about 120 dB reduces the speed of the eyeballs, narrowing the field of view, and may also cause problems with distinguishing colors, which is especially dangerous when driving a car. The sound pressure level above 115 dB is a particularly dangerous level and there is a risk of hearing loss, even with short-term exposure. The levels of various sound sources and their impact on human health are presented in the Table 1.

Table 1. The sound pressure levels of various sources sound [dB] and their impact on human health [13]

Below 160 [dB]	**DEATH NOISE**
155–160	**NOISE CAUSING CONCUSSION BRAIN**
150–155	**PERMANENT NOISE DAMAGE TO HEARING**
145–150	A jet plane taking off from a distance of 10 m
140–145	Alarm siren from a distance of 1 m
135–140	Propeller plane engine
130–135	Hydraulic press from a distance of 0.5 m
125–120	**PAIN BORDER**
120–115	A machine gun from a distance of 0.5 m
115–110	Air hammer from a distance of 5 m
110–105	Disco
105–100	Metro from a distance of 3 m
100–95	Light music concert
95–90	Car horn from a distance of 5 m
90–95	Pneumatic drill from a distance of 2 m
85–90	The interior of the bus
80–85	A scream from a distance of 1 m
75–80	Phone ringtone from 2 m away
70–75	Passenger car engine from a distance of 6 m
65–70	Homemade sewing machine
60–65	Loud conversation from a distance of 2 m
55–60	The church bell from a distance of 400 m
50–55	A small office room, a small shop
45–50	Peaceful conversation
40–45	Quiet street
35–40	Tearing the paper from a distance of 1 m
30–35	Hospital, church, reading room
25–30	Very quiet room, clock ticking from 1 m away
20–25	Radio or movie studio
15–20	Average whisper from a distance of 2 m
10–15	A quiet whisper from a distance of 2 meters
5–10	Breath from the distance of 0.5 m
0–5	The murmur of leaves on a windless day from a distance of 3 m
0	**AVERAGE THRESHOLD OF HEALTHY HEARING**

4.3. Impact of noise on the driver's body

Excessive fatigue, drowsiness, discomfort, imbalance, psychomotor performance and physiological functions are the dominant effects of infrasonic noise on the driver. In addition to the changes described above, the driver's body is exposed to changes in the respiratory and cardiovascular systems, which is related to the reduction in the amount of adrenaline, cortisol and free fatty acids secreted. The effect of infrasound can be compared to the state after drinking a large amount of alcohol, i.e. decreased visual acuity, difficulties in maintaining balance and concentration, prolonged reaction time, increased symptoms of drowsiness and decreased cognitive functions. Accelerating and deepening sensory fatigue, impediment of speech understanding, audibility of warning sounds, worse vision, delayed reaction or mental fatigue negatively affect the possibility of causing a road accident [13, 22].

Apart from the infrasound noise, the driver is also exposed to the negative impact of vibrations, i.e. the transmission of mechanical shocks from a solid body to individual tissues of the human body or to the entire human body, bypassing the air environment [13]. The negative effect of vibrations is the resonance of human organs, which is manifested by strong irritation of the labyrinth in the form of, for example, jaw vibrations, changes in the tension of the larynx muscle, vibrations of the air column in the nasopharyngeal cavity. Other effects may be breathing problems,

a feeling of pain around the heart, decreased visual acuity, which is also accompanied by a narrowing of the field of vision and a problem with distinguishing colors. A very popular effect of the vibration on the body is the seasickness, manifested by headache, dizziness, tinnitus, shortness of breath, stomach pain and nausea [22].

5. Methods of road noise reduction

One of the main sources of noise is the increased share of traffic flow in urban areas, especially heavy goods vehicles. An effective method to reduce the noise level in urban agglomerations is to transfer transit traffic outside the city. The ability to drive trucks only on city ring roads has a positive effect not only on the level of noise generated by vehicles in cities, but also allows to increase the capacity, especially during peak traffic hours.

The second method of reducing road noise is the design of circular intersections. This solution improves traffic flow, therefore the generated road noise is reduced by approx. 4 dB [16]. The biggest problem with standard intersections is sudden deceleration (braking) and acceleration of the vehicle and queues to enter the intersection. The increase in noise level depending on the acceleration or deceleration of various types of vehicle at 50 km/h is shown in the Table 2.

Table 2. Influence of delayed and accelerated motion on road noise [3]

Acceleration or delay [m/s^2]	Vehicle type	Increase of noise [dB]	Description of the movement
1.0	light	+1.7	medium acceleration
2.0	light	+4.5	hard acceleration
0.5	heavy	+2.1	medium acceleration
1.0	heavy	+4.5	hard acceleration
–1.0	light	–0.8	poor braking
–2.0	light	–1.2	hard braking
–1.5	heavy (two axles)	–4.5	medium braking

When assessing the noise level reduction at a circular intersection, many factors should be taken into account, which are influenced by, for example, the radius of the roundabout, the speed of traffic on the approach and departure from the roundabout, the distance of the observer from the roundabout [16].

Road noise resulting from the rolling of wheels on the road surface can be reduced by using surfaces with reduced noise emissions. This type of surface is called quiet road surfaces, characterized by a large number of pores (air-filled channels), whose task is to suppress noise. The best surface that fulfills the functions described above is a porous surface, with a pore content of about 20% and allowing noise reduction above 3 dB. Other materials with reduced noise levels used for road surfaces include: mastic asphalt and asphalt concrete, whose noise reduction efficiency is up to 3 dB. In addition to reducing rolling noise, another advantage of using the pavements described above is that accumulated water is drained more quickly to the lower layers. However, this is a problem when curbs cannot be reconstructed during road modernization (surface change). The use of the above-mentioned surfaces will not bring the expected result due to difficulties with water drainage and problems with cleaning the road [16].

Other methods of noise reduction are the so-called methods by propagation. The first and most frequently used method is acoustic screens. Their task is to create the so-called an acoustic shadow with a lower sound level than outside it. The condition for achieving the best effectiveness is to place the screen as close as possible to the noise source, taking into account the appropriate height and length.

Depending on the height, the following screens can be distinguished [4]:

– tall and very high above 6–7 m, reducing noise above 10 dB,
– medium, 5 m high, with a noise reduction of 7–10 dB (most often used in Poland),
– low up to 3.5 m, noise reduction up to 8 dB, used in uninhabited areas below the course of communication routes,
– very low with a height of 1 m, reducing the noise by about 3 dB.

Due to the principle of operation, there are two types of noise barriers: reflective and absorbing. The first of them are characterized by the sound absorption up to 4 dB, most often they are made of glass, plastic, wooden boards or concrete. Acoustic waves reaching the reflecting screen are almost reflected completely [16]. The second type of screens – absorbing (4–8 dB), reducing the acoustic energy reflected from the screen surface, are most often made of sawdust concrete or steel cassettes filled with sound absorbing material. In order to assess the effectiveness of the use of an acoustic screen, a quantity informing about the difference in noise levels in front of and behind the acoustic barrier is used – acoustic efficiency of sound – formula (6) [20].

$$\Delta L = L_{Aeq} - L_{AeqE}, \text{ [dB]} \tag{6}$$

where: L_{Aeq} – equivalent sound level in front of the acoustic screen, L_{AeqE} – equivalent sound level behind the acoustic screen.

The other most common methods of reducing exposure to road noise along the propagation path are earth embankments – most often used along expressways or creating the so-called green walls, used mainly in places exposed to reflected waves that amplify noise from the source, e.g. among apartment blocks or in courtyards.

6. Assessment of the effectiveness of the acoustic screen application

To evaluate the effectiveness, an acoustic screen was used, located within the "big" city, due to the high traffic intensity, multi-path nature of the stream and high vehicle speed (Wincentego Witosa Street in Poznan). The road running at Wincentego Witosa Street is a provincial road No. 433, characterized by a high level of noise, within which there are apartment blocks, located approx. 15 m from the acoustic screen. As part of the research, a point measurement of noise generated by road vehicles in front of and behind the noise barrier was performed in two traffic rush hours: at 4:00 p.m. and 7:00 a.m. During these hours,

there is the greatest accumulation of vehicles of people commuting to and returning from work. In addition to the point measurement, a frequency measurement was also performed. A certified Class I digital sound level meter (Bruel & Kjaer 2238) was used to perform the tests. The impact of vehicle traffic on the levels of generated noise in front of and behind the acoustic screen during two measurement hours was presented in Fig. 2. On the basis of the obtained test results, the highest noise level was noticed at the level of 89.5 dB at 4 p.m. and 92.8 dB at 7 a.m. The screen acoustic efficiency was calculated using the formula (6) and the obtained results are presented below:

$$\Delta L_{4\ \text{p.m.}} = 80.9\ \text{dB} - 74.4\ \text{dB} = 6.5\ \text{dB}$$

$$\Delta L_{7\ \text{a.m.}} = 82.6\ \text{dB} - 65.1\ \text{dB} = 17.5\ \text{dB}$$

a)

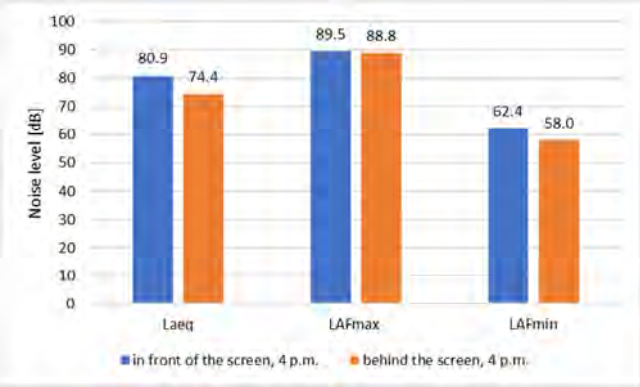

b)

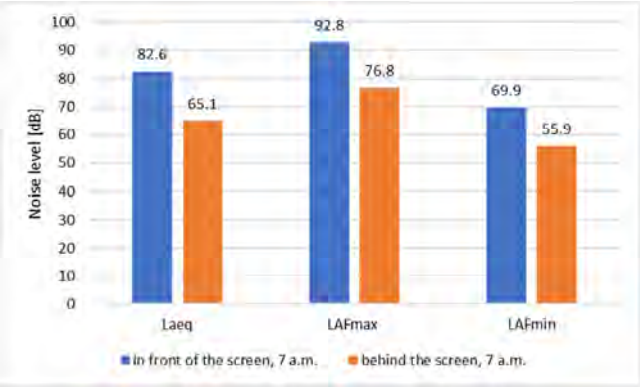

Fig. 2. The impact of vehicle traffic on the noise levels obtained in front of and behind the acoustic screen for the selected measuring section (Wincentego Witosa Street, Poznan) during the traffic rush: a) in the afternoon around 4 p.m., b) in the morning around 7 a.m. [20]

The use of an acoustic screen at Wincentego Witosa Street allowed to reduce the noise level from 6.5 to 17.5 dB. Lowering sound pressure levels has made it possible to reduce the risk of permanent hearing damage. The greatest noise reduction was recorded around 7 a.m. During the traffic rush hours around 4 p.m., exposure to noise is still very high and may have a negative impact on people living in the area near the acoustic screen, causing e.g. irritation, fatigue or e.g. headaches.

7. Conclusion

Traffic noise is a very dangerous civilization problem which, like exhaust emissions, requires a lot of research, analysis and activities aimed at reducing its nuisance. Exposure to noise carries the risk of hearing loss, problems with the proper functioning of many organs in humans, causes mental problems, and has a negative impact on the quality of life of people. It is especially dangerous when driving on the road, because its long-term impact on a person increases the risk of accidents. Noise is a problem that can be tackled at its source through the diagnostics of vehicles and its components, reducing rolling noise by using appropriate road surfaces, turning classic intersections into circular intersections, reducing vehicle speed or reducing noise along the path of propagation. The use of each of the noise reduction methods is extremely important for the natural environment, as there is no physiological adaptation to noise in humans [6]. Human is not able to get used to the acoustic state he is in, so it is necessary to counteract it, because in the worst case the noise can even lead to death. The research on the effectiveness of the use of an acoustic screen at Wincentego Witosa Street showed that the equivalent sound level for the acoustic screen at Wincentego Witosa Street was reduced by 6.5 and 17.5 dB. The differences between the achieved effectiveness of the acoustic screen were related to the variable intensity of vehicle traffic and participation in the traffic of vehicles of various categories. Despite noise reduction, noise exposure is still very high and adversely affects people's health and quality of life. Therefore, it is necessary to reduce noise at its source (in the vehicle) by actively assessing the noise level in traffic and reducing the main design sources and resulting from working processes generated in their propulsion sources (internal combustion engines, hybrid engines) and the drive system (feedback between continuous noise testing and design modifications and assessment of their effectiveness). In further stages of the research, it is possible to eliminate noise sources as a result of their real-time control at the level of a single vehicle. In this process, however, remember to separate the acoustic signal for a single vehicle and define the sound source from a specific component, taking into account external sound sources.

Nomenclature

I	sound intensity value, expressed in $W \cdot m^{-2}$
I_0	reference sound intensity, equal to $1 \cdot 10^{-12}$ $W \cdot m^{-2}$
L	relative measure of sound pressure, sound intensity
L_A	sound level using the A correction characteristic
L_{Aeq}	equivalent sound level
L_{AeqD}	equivalent sound level during the day (6 a.m. to 10 p.m.)
L_{AeqE}	equivalent sound level behind the acoustic screen
L_{AeqN}	equivalent sound level at night (10 p.m. to 6 a.m.)
LAF_{max}	maximum sound level
LAF_{min}	minimum sound level
L_{DWN}	day-evening-night sound level
L_{MZHk}	relative share of the area's population, expressed in %
L_{N1}	sound power level

L_{N2}	Night sound level, to define all the nights of the year
ΔL	the effectiveness of the acoustic screen
M	the amount of noise standards exceeded and the number of people exposed to noise
N	sound sound power value, expressed in W
N_0	reference sound power, equal $1 \cdot 10^{-12}$ W
p	sound pressure
P_0	reference sound pressure equal to $2 \cdot 10^{-5}$ Pa
P_A	instantaneous value of the sound pressure, expressed in Pa
$t_2–t_1$	reference time interval T
T_{MZH}	the ratio of the surface area on which high sound levels occur

Bibliography

[1] BARRIGÓN MORILLAS, J.M., REY GOZALO, G., MONTES GONZÁLEZ, D. et al. Noise pollution and urban planning, *Current Pollution Reports*. 2018, **4**, 208-219. https://doi.org/10.1007/s40726-018-0095-7

[2] BASNER, M., BABISCH, W., DAVIS, A. et al. Auditory and non-auditory effects of noise on health. *Lancet.* 2014, **383(9925)**, 1325-1332. https://doi.org/10.1016/s0140-6736(13)61613-x

[3] BENDTSEN, H., ELLEBJERG, L. Traffic management and noise, *Inter-Noise.* 2006, USA.

[4] BĘBEN, D.N, Hałas wokół szlaków transportowych. *Drogownictwo*. 2010, **9**, 293-304.

[5] BOHATKIEWICZ, J., BIERNACKI, S. Aktualne problemy związane z hałasem drogowym, *Ochrona środowiska i estetyka a rozwój infrastruktury drogowej. Stowarzyszenie Inżynierów i Techników Komunikacji RP*. 2011, 38-47.

[6] BORTKIEWICZ, A., CZAJA, N. Pozasłuchowe skutki działania hałasu ze szczególnym uwzględnieniem chorób układu krążenia. *Forum Medycyny Rodzinnej.* 2018, **2**(12), 41-49.

[7] BRANDT, S., MAENNIG, W. Road noise exposure and residential property prices: Evidence from Hamburg. *Transportation Research Part D: Transport and Environment.* 2011, **16**, 23-30. https://doi.org/10.1016/j.trd.2010.07.008

[8] CEDR Call 2012: Noise; ON-AIR Optimised noise assessment and management guidance for national roads, investigation of noise planning procedures and tools, 2017.

[9] Dyrektywa 2002/49/WE z dnia 25 czerwca 2002 Parlamentu Europejskiego i Rady odnośnie oceny i zarządzania poziomem hałasu w środowisku pracy.

[10] KHAN, J., KETZEL, M., KAKOSIMOS, K. et al. Road traffic air and noise pollution exposure assessment – a review of tools and techniques. *Science of The Total Environment*. 2018, **634**, 661-676. https://doi.org/10.1016/j.scitotenv.2018.03.374

[11] KIRPLUK, M. Badanie hałasu komunikacyjnego. NTL-M.Kirpluk, Warszawa 2013.

[12] LAN, Z., CAI, M. Dynamic traffic noise maps based on noise monitoring and traffic speed data. *Transportation Research Part D: Transport and Environment.* 2021, **94**, 2604-2610. https://doi.org/10.1016/j.trd.2021.102796

[13] LEŚNIKOWSKA-MATUSIAK, I., WNUK, A. Wpływ hałasu komunikacyjnego na stan środowiska akustycznego człowieka. *Transport samochodowy.* 2014, **3**, 37-63.

[14] PASZKOWSKI, W. Innowacyjna metoda oceny hałasu drogowego w środowisku miejskim. *Mechanik.* 2014, 513-522.

[15] PERZYŃSKI, T., PIETRUSZCZAK, D., PONETA, A. The noise analysis of road transport in selected points of the Radom city. *Autobusy.* 2019, **6**, 81-85. https://doi.org/10.24136/atest.2019.130

[16] Program ochrony środowiska przed hałasem dla miasta Poznania 2018, *Akustix, lemitor*. 2018.

[17] RAHMANI, S., MOUSAVI, S.M., KAMALI, M.J. Modeling of road-traffic noise with use of genetic algorithm. *Applied Soft Computting.* 2011, **11**(1), 1008-1013. https://doi.org/10.1016/j.asoc.2010.01.022

[18] RYMANIAK, Ł., KAMIŃSKA, M., SZYMLET, N. et al. Analysis of harmful exhaust gas concentrations in cloud behind a vehicle with a spark ignition engine. *Energies.* 2021, **14**(6), 1769-1-1769-16. https://doi.org/10.3390/en14061769

[19] SERDECKI, W. Badania silników spalinowych. *Wydawnictwo Politechniki Poznańskiej*. Poznań 2012.

[20] SZYNKARUK, K. Ocena akustycznego oddziaływania pojazdów drogowych na ludzi w aglomeracji miejskiej. *Praca dyplomowa inżynierska*. Poznań 2018.

[21] WALIGÓRSKI, M., BATURA, K., KUCAL, K. et al. Research on airplanes engines dynamic processes with modern acoustic methods for fast and accurate diagnostics and safety improvement. *Measurement*. 2020, **154**, 107460-1-107460-15. https://doi.org/10.1016/j.measurement.2019.107460

[22] WĄGROWSKA-KOSKA, E. Zagrożenia zdrowia kierowców pojazdów silnikowych związane ze szkodliwymi i uciążliwymi warunkami środowiska pracy. *Oficyna Wydawnicza Instytutu Medycyny Pracy*. Łódź 2007.

[23] YANG, W., HE, J., HE, C. et al. Evaluation of urban traffic noise pollution based on noise maps. *Transportation Research Part D: Transport and Environment.* 2020, **87**, 102516-1-102516-14. https://doi.org/10.1016/j.trd.2020.102516

[24] Zagrożenie hałasem w środowisku pracy w Polsce, Centralny Instytut Ochrony Pracy – Państwowy Instytut Badawczy, www.ciop.pl

Karolina Paula Batura, MEng. – Faculty of Civil and Transport Engineering, Poznan University of Technology, Poland.
e-mail: *karolina.batura@doctorate.put.poznan.pl*

Prof. Marek Waligórski, DSc., DEng. – Faculty of Civil and Transport Engineering, Poznan University of Technology, Poland.
e-mail: *marek.waligorski@put.poznan.pl*

Article citation info:
SIADKOWSKA, K., CZAJKA, B., ŚCISŁOWSKI, K. et al. Analysis of propulsion units dedicated to test stands for aviation systems. *Combustion Engines*. 2021, **185**(2), 39-43. https://doi.org/10.19206/CE-139405

Ksenia SIADKOWSKA
Błażej CZAJKA
Karol ŚCISŁOWSKI
Mirosław WENDEKER

Analysis of propulsion units dedicated to test stands for aviation systems

This paper presents an analysis of selected propulsion units dedicated to test stands for unmanned aircraft systems. It focuses on engines suitable for aircraft with a maximum take-off mass up to 150 kg. The study includes an analysis of propulsion units that can be used to power systems on stationary test stands dedicated to advanced research and measurement of prototype aerospace technologies intended for use in rotorcraft. The analysis of propulsion units shows that electric units are a better choice for powering UAV rotorcraft test stands. Their main advantages include the possibility to simplify the construction of the device by eliminating gears and to mount the motor in a vertical position, simpler power supply, cooling and control systems and the lack of an exhaust system. Additional advantages are undoubtedly lower vibration generation, cheaper and easier operation as well as better comfort.

Key words: *combustion engine, electric motor, test stand, unmanned aerial vehicle*

1. Introduction

Not so long ago, it seemed that the beginning of the 21st century would be a period of intense aviation development. The transport of people and goods by air has increased its market share every year [10, 16]. Environmental regulations are increasingly influencing the type of transport used [11], but the market for unmanned aerial vehicles is experiencing intensive development, both in terms of the technologies used and the scope of use of unmanned aerial systems [5, 8]. Diverse technologies for enhancing the operational capabilities of UAVs are used and considered.

For propulsion of unmanned aerial vehicles weighing more than 50 kg, propeller power units with two- or four-stroke piston engines are mainly used. It is characteristic that while in UAV with mass between 50 kg and 100 kg engines of various manufacturers are used, whereas in the mass range of 100–500 kg is dominated by rotary piston engines. Internal combustion engines are popularly used to power manned ultralight aircraft, by their high reliability, relatively long overhaul intervals (of the order of several hundred hours), which are at least several times lower than the prices of engines manufactured exclusively for unmanned aerial vehicles.

Regardless of the concept of conducted research, it is essential to test new systems before launching the aircraft onto the market. The first stage is computer-aided design and numerical fluid mechanics testing [15]. The next stage is bench testing [18]. The preparation of a bench and the selection of a suitable power unit determine the success and efficiency of research. The dynamic development of the engine market and the seemingly abundant offer and possibilities of applying selected power units to flying prototype systems make it possible to freely shape test stands. This publication focuses on the analysis of propulsion units that can be used to power systems on stationary test stands dedicated to advanced research and measurement of prototype aircraft technologies for rotorcraft. The paper points out that appropriately selected propulsion units have a decisive influence on the effects of conducted research. Based on commercially available engines and manufacturers' data, the main parameters for analysis are presented. The benefits of using specific solutions are indicated and the risks associated with the use of an inappropriate power unit are defined. Selection of a proper propulsion unit is an example of how to optimise energy consumption and emissions of target flying systems.

This study focuses on the analysis of aircraft with an MTOM of 150 kg, equipped with different propulsion systems. Part of research focuses on the use of alternative fuels in already existing internal combustion engines, e.g. synthetic fuels in a Wankel engine [17] or the modification of engine assistance systems to reduce emissions [6]. The use of a compression ignition engine in light aviation is also being considered and such aircraft are already in service [19]. Research is also underway to develop an aviation diesel engine with opposed pistons [7, 20]. Other concepts to reduce emissions or aircraft power demand are related to interference with aircraft aerodynamics [2] or the use of modern construction materials [22] or even interference with an aircraft shape through the use of smart materials [1, 3].

Thus, it is one thing to select an internal combustion engine for an aircraft and another to select an engine to drive a propeller system test stand. In particular, the following aspects are important: absence of reduction gearbox, ability to operation in any position, vibration, weight and size. These and other aspects will be analyzed in this paper.

2. Materials and methods

The methodology used in this study enables us analyse and evaluate literature resources. In addition, solutions offered on the market are reviewed and their suitability for the test bench is determined.

2.1. Selection of basic engine parameters

Unmanned helicopters with a take-off weight of up to 150 kg are powered by internal combustion or electric engines. An analysis of existing designs has shown that the minimum power demand and engine torque depend on the rotor design, size and operating parameters. According to the calculations carried out, for a 2 m diameter main rotor design with a maximum speed of 1500 rpm, the parameters of the required power and torque are 25 kW and 150 Nm, respectively. An exemplary aircraft with the given take-off mass is the UMS SKELDAR R-350 (Fig. 1) powered by a 25 kW turboshaft engine [26].

Received 31 March 2021; Received in revised form 25 June 2021; Accepted 26 June 2021
Available online 29 June 2021

Fig. 1. UMS SKELDAR R-350 unmanned helicopter [25]

2.2. Combustion engines

Two aircraft combustion power units were analysed. The first is a two cylinder two-stroke inline engine – the F23 Lightweight (Fig. 2) manufactured by Hirth Engines. It is used to power, among others, the Solid Air Diamant LP (ultralight trike) and the Aeronix Airelle (ultralight tandem wing). The second engine is the AR731 from UAV ENGINES. This is a Wankel engine specifically manufactured for use in UAVs.

Fig. 2. View of the F23 Lightweight engine [21]

2.3. Electric motors

Electric motors were also analysed here due to their increasing use in aircraft propulsion and the conditions of use of the test stand. Three types of units were considered here, i.e. an induction motor, a permanent magnet synchronous motor (PMSM), and a brushless direct current motor (BLDC).

The first of these is the industrial solution of TAMEL 4Sg200L-4-IE2 (Fig. 3). It is an induction motor with improved efficiency, the IE2 class according to IEC60034-30:2009.

Fig. 3. View of the 4Sg200L-4-IE2 motor [23]

The other proposed units are permanent magnet motors. The PMSM type motor analysed was a product from VEM with the symbol PE1R200L4, also manufactured for industrial applications.

The last drive unit included in the review was REB 30 from the Czech company MGM COMPRO, representing BLDC type motors. Its parameters are only close to those required. This is due to the low availability of engines of this type on the market which meet the required assumptions. Such motors are not very popular and the full specification of these units is not available. The presented engine is a product used mainly in aviation, for propelling VTOL aircraft and drones. The specific design of the engine is shown in Fig. 4.

Fig. 4. REB30 motor [12]

3. Results

3.1. Combustion engines

Selected internal combustion engine parameters collected during the analysis of existing designs are given in Table 1.

Both of these drive units meet the power requirements of a test rig for rotorcraft with a take-off mass of up to 150 kg. However, it is very important to note that for both engines, mechanical transmissions are required to achieve the desired torque and speed. This complicates the construction of the test stand and, consequently, affects the economic aspect, increasing the cost of the device. This is undoubted-

ly a disadvantage of the use of internal combustion engines, as their operating range covers rotational speeds significantly exceeding the values required on the rotorcraft test stand. The AR731 engine reaches its highest torque at about 7000 rpm and maximum power at 8000 rpm and the F23 at 6500 rpm respectively (Fig. 5).

Table 1. Selected parameters of internal combustion engines [14, 24]

Parameter	Unit	F23 Lightweight	AR731
Engine type	–	Boxer	Wankel
Maximum power	kW	36.7 (6500 rpm)	28.3 (8000 rpm)
Maximum torque	Nm	53.0 (6300 rpm)	35.5 (7000 rpm)
Calculated torque (at 1500 rpm) if a gearbox applied	Nm	231	178
Weight	kg	22	9.9
Power-to-weight ratio	kW/kg	1.67	2.86
Fuel	–	Min. 95 octan fuel with 2-stroke-oil	Mogas regular grade or Avgas 100LL
Cooling	–	Air	Air
Size	mm	591×493.5×366	328×600×262

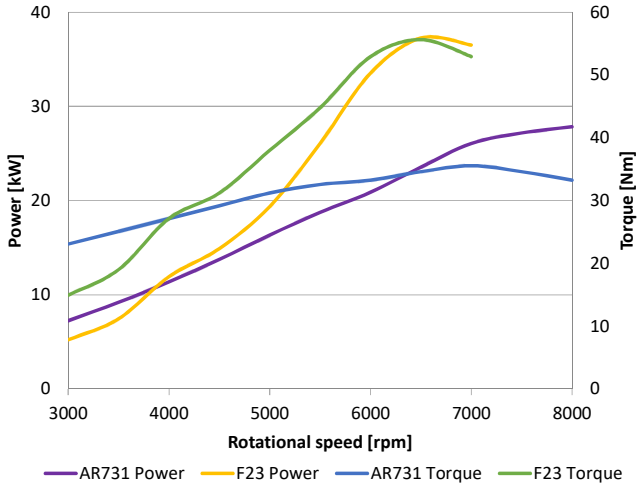

Fig. 5. External characteristics of AR731 and F23 engines [14, 24]

Another disadvantage of using internal combustion units is the need to purchase, store and supply fuel to the engine, and in the case of two-stroke engines, also to prepare a pile-oil mixture such as the F23 Lightweight. This necessitates the construction of an adequate supply system in the laboratory, equipped with apparatus enabling the control and maintenance of fluid parameters such as temperature and pressure. In addition, the use of internal combustion engines requires the use of a fume extraction system for indoor testing. The disadvantages of such a solution also include the need for a special system enabling air cooling of drive units and a complicated system for controlling operating parameters and steering the drive unit.

An undoubted advantage of using a Wankel engine such as the AR731 is the low vibration level declared by the manufacturer [24]. In the case of combustion units with a different layout, there is a need to dampen generated vibrations.

3.2. Electric motors

Considering many disadvantages resulting from the use of internal combustion engines in test stands, electric engines were analysed. They offer a greater choice because of a wider market of units characterised by parameters similar to those required. Selected parameters of the engines under consideration are listed in Table 2.

Table 2. Parameters of selected electric motors [12, 23, 27]

Parameter	Unit	4Sg200L -4-IE2	PE1R200L4	REB 30
Motor type	–	Induction	PMSM	BLDC
Nominal power	kW	30 (1400 rpm)	30 (1500 rpm)	25-30
Indicated torque	Nm	195	191	150
Calculated torque (at 1500 rpm)	Nm	191	191	N/A
Weight	kg	270	220	7.7
Power-to-weight ratio	kW/kg	0.11	0.14	3.90
Supply	V	400 AC	400 AC	63-800 DC
Cooling	–	Fan integrated	Fan integrated	Air/hybrid
Size	mm	400×787 ×501	400×680 ×461	267×101 ×267

The great advantage of electric motors is the existence of units with sufficient power and speeds close to the required one and still generating sufficient torque. Speed control can be performed with an inverter, which is a much simpler method than in the case of internal combustion engines. This allows the relevant parameters (speed and torque) to be achieved without the need for reduction gears. Additionally, they can be used in any position, which allows them to be placed vertically under the rotor and the shafts to be axially aligned without additional bevel gears. An electrical system is required to power the motors, which is generally a simpler solution than a fuel supply system. In the case of DC motors, additional AC-DC converters are required, which somewhat complicates the installation. An alternative is battery power. However, this is less advantageous due to the cost of batteries and the need to recharge them. It must be ensured however that the electrical installation is of sufficient voltage to meet the power requirements of the engine. Moreover, most electric motors do not need additional cooling systems. The BLDC motor presented here is an exception, because it is used in aviation and there is a pursuit to reduce weight, taking into account the possibility of cooling while the aircraft is in motion. The advantage of electric motors is that they generate less vibration than internal combustion ones. A huge advantage is also their simpler and cheaper operation. They do not require periodic servicing, replacement of fluids and consumable parts. They are also less prone to faults due to their less complex construction. They also show higher efficiency, which reduces both operating costs and environmental pollution. The comfort of using electric motors is also higher, as their operation is quieter and their maintenance is cleaner [9]. A significant disadvantage of using electric motors is cables with relatively high voltage. They may adversely affect the indications of measuring devices. A good separation of signal wires and the use of shielding is a necessity.

Induction motors and PMSMs are the largest in size and weight, while the presented BLDC motor is lighter and smaller than both these designs and internal combustion engines. The BLDC motor also has the highest power-to-weight ratio. When used in an aircraft, these parameters would probably eliminate induction motors and PMSMs, but in the case of the test bench this is not a critical parameter. Larger size is not such a key issue, and significantly higher mass can even be an advantage as it adds weight to the bench. A significant disadvantage of BLDC motors is still the small number of products offered with a power of more than 20 kW. In addition, most of the products on offer are only available to order, which increases waiting times and purchase costs. Due to their construction, BLDC motors and PMSMs have a larger speed control range than induction motors while maintaining high efficiency. In addition, they can be significantly overloaded. Higher efficiency of permanent magnet motors translates into smaller size and weight while maintaining similar electromechanical parameters [4].

Electric units generate high torque from the first motor revolutions [13]. Additionally, induction motors generate an even higher starting torque. This makes it easy to set the rotor in motion and removes the need to warm up the motor before testing, which would be the case for internal combustion engines. The induction type motor is also the most popular of electric motors, resulting in the widest choice, easy availability and lowest prices of the solutions considered.

3.3. Comparison of internal combustion and electric motors

Internal combustion engines and electric motors were compared Table 3 in terms of their advantages and disadvantages.

The advantages presented indicate the superiority of electric motors in application to UAV test stands.

4. Conclusions

The analysis of the motors shows that electric units are a better choice for powering UAV rotorcraft test stands. Their main advantages include the possibility to simplify the construction of the device by eliminating gears and to mount the motor in a vertical position, simpler power supply, cooling and control systems and the lack of an exhaust system. Additional advantages are undoubtedly lower vibration generation, cheaper and easier operation as well as better comfort.

Due to the fact that the offer of BLDC motors meeting the power requirements is limited, and the weight and size of the motor during ground tests do not play a key role, induction motors and PMSMs seem to be a better choice. These units are manufactured in many configurations, which allows for a favourable selection of performance parameters to meet demand. When choosing between a PMSM and an induction motor, it is worth remembering about the possibility of more accurate speed control while maintaining high efficiency in the case of a PMSM. Additionally, with similar parameters of operation it should be lighter and smaller than an induction motor. Additionally, an induction motor shows a high starting torque, which helps set the rotor in motion, while a PMSM requires appropriate control.

Table 3. Advantages and disadvantages of selected engines

Aspect	Combustion engines	Electric motor
Reduction gearbox	Necessary	Unnecessary
Bevel gearbox	Necessary	Unnecessary
Operation in any position	No	Yes
Supply system	Sophisticated, extra measurement necessary	Electric installation necessary, system design simpler that in combustion engines
Exhaust gas system	Yes	No
Control system	Sophisticated	Simple
Cooling system	Necessary	Mostly unnecessary
Vibration	Mostly high vibration	Low vibration
Measurement and signal disturbance	None or low	Possible due to high voltage cables
Weight	Low	Higher, except for BLDC motors
Size	Smaller	Larger, except for BLDC motors
Market availability	Single limited series on demand, no ideal operations parameters	Single limited series of BLDC motors, wide offer, serial production of PMSMs and induction motors
Price	High	BLDC/PMSM – moderate Induction – low
Maintenance costs	High	Low
Difficulty of operation	Higher	Lower
Operation comfort	Lower	Higher

It should be remembered however that the final choice of a motor should be guided by the power and torque requirements for the case. In addition, the decision may be influenced by infrastructure and installations already in place, which is an individual matter for users.

Acknowledgements

This work has been financed by the National Centre for Research and Development under the LIDER program. Grant Agreement No. LIDER/45/0177/L-9/17/NCBR/2018.

Nomenclature

PMSM Permanent Magnet Synchronous Motor
BLDC Brushless Direct-Current Motor
VTOL Vertical Take Off and Landing
UAV Unmanned Aerial Vehicle

Bibliography

[1] AMEDURI, S., CONCILIO, A. Morphing wings review: aims, challenges, and current open issues of a technology. *Proceedings of the Institution of Mechanical Engineers, Part C: Journal of Mechanical Engineering Science*. 2020. https://doi.org/10.1177/0954406220944423

[2] BAI, C.-J., WANG, W.-C. Review of computational and experimental approaches to analysis of aerodynamic performance in horizontal-axis wind turbines (HAWTs). *Renewable and Sustainable Energy Reviews*. 2016, **63**, 506-519. https://doi.org/https://doi.org/10.1016/j.rser.2016.05.078

[3] BARBARINO, S., BILGEN, O., AJAJ, R.M. et al. A review of morphing aircraft. *Journal of Intelligent Material Systems and Structures*. 2011, **22**(9), 823-877. https://doi.org/10.1177/1045389X11414084

[4] BERNATT, J., GAWRON, S., KRÓL, E. Nowoczesne silniki z magnesami trwałymi do zastosowań trakcyjnych. *TTS Technika Transportu Szynowego*. 2010, **16**(1-2), 73-76.

[5] COLOMINA, I., MOLINA, P. Unmanned aerial systems for photogrammetry and remote sensing: a review. *ISPRS Journal of Photogrammetry and Remote Sensing*. 2014, **92**, 79-97. https://doi.org/10.1016/j.isprsjprs.2014.02.013

[6] FADHLI, M.H.W., DALI, A.L.A., MARKUS, S. et al. Optimization of charge motions for improving emissions internal combustion 4 stroke ROTAX engines. *SAE Technical Paper* 2007-24-0057. 2007. https://doi.org/10.4271/2007-24-0057

[7] GRABOWSKI, Ł., PIETRYKOWSKI, K., KARPIŃSKI, P. Charging process analysis of an opposed-piston two-stroke aircraft Diesel engine. *ITM Web of Conferences*. 2017, **15**, 03002. https://doi.org/10.1051/itmconf/20171503002

[8] HASSANALIAN, M., ABDELKEFI, A. Classifications, applications, and design challenges of drones: a review. *Progress in Aerospace Sciences*. 2017, **91**, 91-131. https://doi.org/10.1016/j.paerosci.2017.04.003

[9] KRÓL, E. Silniki synchroniczne w napędach pojazdów sportowo-rekreacyjnych. *Zeszyty Problemowe – Maszyny Elektryczne*. 2014, **102**(2), 23-27.

[10] LIU, Y., KREIMEIER, M., STUMPF, E. et al. Overview of recent endeavors on personal aerial vehicles: a focus on the US and Europe led research activities. *Progress in Aerospace Sciences*. 2017, **91**, 53-66. https://doi.org/10.1016/j.paerosci.2017.03.001

[11] MAYOR, K., TOL, R.S.J. Scenarios of carbon dioxide emissions from aviation. *Global Environmental Change*. 2010, **20**(1), 65-73. https://doi.org/10.1016/j.gloenvcha.2009.08.001

[12] MGM COMPRO. *MGM COMPRO 15-30 kW Electric Motors*. 2021. https://www.mgm-compro.com/products/15-30kw-electric-motors/

[13] NEMŚ, A. Niskoemisyjne silniki: elektryczne czy spalinowe? Elektryczne, ale nasz system by tego nie wytrzymał. *Energia Gigawat*, 2012, **8**.

[14] NORTHWEST UAV. *F23 Lighweight 23 Series*. 2021. www.nwuav.com

[15] SARAF, A.K., SINGH, M.P., CHOUHAN, T.S. Aerodynamic analysis of NACA0012 airfoil using CFD. *International Journal of Mechanical and Production Engineering*. 2017, **5**(12), 21-25.

[16] SEHRA, A.K., WHITLOW, W. Propulsion and power for 21st century aviation. *Progress in Aerospace Sciences*. 2004, **40**(4-5), 199-235. https://doi.org/10.1016/j.paerosci.2004.06.003

[17] SIADKOWSKA, K., WENDEKER, M., MAJCZAK, A. et al. The influence of some synthetic fuels on the performance and emissions in a Wankel engine. *SAE Technical Papers* 2014-01-2611. 2014. https://doi.org/10.4271/2014-01-2611

[18] SIADKOWSKA, K. Wind tunnel research on the unmanned aerial vehicle rotor blade setting angle. *Advances in Science and Technology Research Journal*. 2020, **14**(4), 104-114. https://doi.org/10.12913/22998624/126047

[19] SIADKOWSKA, K., MAJCZAK, A., BARAŃSKI, G. Studying a construction of pistons for the aircraft CI engine. *Combustion Engines*. 2017, **168**(1), 161-167. https://doi.org/10.19206/CE-2017-126

[20] SOCHACZEWSKI, R., SZLACHETKA, M. Numerical analysis of a fuel pump for an aircraft Diesel engine. *MATEC Web of Conferences*. 2019, **252**, 01003. https://doi.org/10.1051/matecconf/201925201003

[21] SUAS NEWS – BUSINESS OF DRONES. Northwest UAV, Hirth Engines sign distribution agreement for North and Central America. 2021. https://www.suasnews.com/2020/09/northwest-uav-hirth-engines-sign-distribution-agreement-for-north-and-central-america/

[22] SUROWSKA, B. Functional and hybrid materials in air transport. *Eksploatacja i Niezawodność – Maintenance and Reliability* 2008, **3**, 30-40. http://www.ein.org.pl/sites/default/files/2008-03-04.pdf

[23] TAMEL S.A. Silniki IE2 w obudowie żeliwnej – 4Sg. 2009.

[24] UAV ENGINES. AR731- 38 BHP AV target engine. 2021.

[25] UMS SKELDAR SWEDEN AB. R-350 VTOL Remotely Piloted Aerial System. 2016.

[26] UMS SKELDAR SWEDEN AB. UMS SKELDAR R-350. 2021. https://umsskeldar.aero/our-products/land-solutions/

[27] VEM MOTORS GmbH. Permanent magnet synchronous motors for inverter operation. 2021.

Ksenia Siadkowska, MEng. – Faculty of Mechanical Engineering, Lublin University of Technology, Poland.
e-mail: *k.siadkowska@wp.pl*

Błażej Czajka, MEng. – Faculty of Mechanical Engineering, Lublin University of Technology, Poland.
e-mail: *blazej.czajka@pollub.edu.pl*

Karol Ścisłowski, MEng. – Faculty of Mechanical Engineering, Lublin University of Technology, Poland.
e-mail: *k.scislowski@pollub.pl*

Prof. Mirosław Wendeker, DSc., DEng. – Faculty of Mechanical Engineering, Lublin University of Technology, Poland.
e-mail: *m.wendeker@pollub.pl*

Article citation info:
DZIUBAK, T., BĄKAŁA, L. Problems of selecting filter partition in passenger car engine intake air filters. *Combustion Engines*. 2021, **185**(2), 44-59. https://doi.org/10.19206/CE-139629

Tadeusz DZIUBAK
Leszek BĄKAŁA

Problems of selecting filter partition in passenger car engine intake air filters

The aim of this study was to verify the criteria for selecting pleated filter partitions used in passenger car engine filters. The paper presents the problem of optimizing pleated air filters in the direction of minimizing pressure drop, which is the source of engine energy losses. Two criteria for selection of a paper filter partition for specific operating conditions of the filter and the engine are presented: criterion of permissible separation speed and criterion of permissible pressure drop. The actual filtration area of 44 paper pleated filter elements used in passenger cars and the air stream flowing through the filter were determined, which made it possible to calculate separation speed. In 62% of the analyzed filter inserts, the calculated separation speeds are within the speed range recommended by the constructors, υ_{Fmax} = 0.06–0.12 m/s. Exceeding permissible separation speed υ_{Fmax} = 0.12 m/s was found mainly in supercharged engines. Negative effects of engine operation with an air filter with too small separation area are presented, in the form of increased pressure drop and energy loss of the engine as well as shorter car mileage to reach permissible pressure drop.

Key words: *combustion engines, air filter, pleated filter cartridge, separation speed, pressure drop, dust absorption coefficient*

1. Introduction

Together with the air, internal combustion engines of motor vehicles and working machines suck in significant amounts of pollutants from the environment, the basic component of which is mineral dust (road dust) carried from the ground by moving vehicles or by the wind. The basic components of road dust are: SiO_2 silica and Al_2O_3 alumina, which share in dust reaches 95%, and Fe_2O_3, MgO, CaO. Moreover, the dust contains: K_2O, Na_2O, SO_3 [4, 48]. Chemical composition of dust depends strictly on the composition and type of substrate, climatic factors (winds, rains, snow, frost, droughts, etc.), as well as on industrial dust, forest fire dust and volcanic ash [57].

Airborne dust is highly abrasive and is the most common cause of accelerated wear of two frictionally cooperating parts, such as the P-P-C (piston–piston rings–cylinder walls) connection in engines. On the ten-point Mohs scale, where 10 corresponds to the hardness of diamond, silica has a hardness of 7, and corundum has 9. Dust sucked in with the air gets over the piston, which is the reason why the upper part of the cylinder and piston and the upper piston rings wear the most. Abrasive wear of engine components is caused mainly by particles of 1–40 µm, with the most harmful particles in the range of 1–20 µm [3, 23, 28].

Authors of thesis [28] report that about 30% of pollutants getting into the engine can escape, in principle, unchanged along with the exhaust gases from the cylinders to the exhaust system, thus increasing the emission of solid particles (PM) from the engine. Only 10–20% of the dust that enters into the engine with the air through the intake system settles on the cylinder liner wall. Together with the oil, this part of the dust forms a kind of abrasive paste which, in contact with the mating surfaces of the engine, for example P-PR-C, causes abrasive wear. The most dangerous for two cooperating engine components are dust particles whose diameter dp is equal to the oil film thickness h_{min} between this two surfaces at the moment. In typical combinations of internal combustion engine, oil thickness film depends on the conditions and parameters of the engine as well as the properties of the oil and, therefore, they assume different values in the range of h_{min} = 0–10 µm [55]. Moreover, the value of the minimum oil film thickness and the period of its occurrence in the engine cycle depends on sliding surfaces' shape asymmetry geometry [56]. Rest of the dust is evaporated or oxidized during the combustion of fuel in the cylinder (under high pressure and high temperature conditions).

In order to ensure adequate air purity at the inlet to traction engines and minimize wear of engine components, the intake system is equipped with an air filter, which, depending on the operating conditions of the vehicle, differs in principle, mode of operation, design, type of materials used for filtering partitions and efficiency. For this reason, passenger car engines operated at low dust concentrations are equipped with single-stage (partition) filters, where filter element is a cartridge made of filter paper or non-woven fabric. In order to increase the active surface of the insert, the material is pleated and then formed into a rectangular panel (Fig. 1). Truck engines, special vehicles (tanks, armored personnel carriers, infantry fighting vehicles) and working machines operated in conditions of high dust concentrations in the air are equipped with two-stage filters.

An additional task of the intake system is:

- supplying engine cylinders with air in appropriate amounts and with appropriate parameters in such a way as to ensure the correct course of the fuel combustion process in the engine cylinders [22, 25, 36, 50],
- noise suppression of combustion process in the engine [9],
- forcing the emergence of wave phenomena causing the so-called dynamic boost (resonant) at the desired engine operating ranges, thus increasing the filling and engine power [47].

Other elements of air supply system are: a flow meter, turbocharger, charge air cooler, air throttle on SI engines, intake manifold, inlet channels in the head and intake valves. Air flow meter located behind the air filter continuously registers flowing air mass and delivers this message in the form of a voltage signal to the microprocessor of the car's on-board computer.

Turbocharger (standard equipment in diesel engines) is to increase mass of the working medium supplied to the engine cylinders by increasing the pressure (also increases

Received 16 June 2021; Received in revised form 29 June 2021; Accepted 30 June 2021
Available online 30 June 2021

the temperature) of the air sucked into the system. The air cooler lowers the charge air temperature (its density increases), and thus the air mass flow to the engine cylinders increases. To register permissible resistance of air filters used in sectional and special trucks (exceptionally passenger cars), sensors are used, which are mounted on the outlet pipe from the air filter. Air supply system is linked to the operation of the crankcase ventilation system and the EGR (Exhaust Gas Recirculation) system.

Passenger car air filter is mounted in the engine compartment under the hood (Fig. 1). The shape of the filter is adapted to the limited space of this compartment. It also ensures easy access during service works, simple and easy assembly of the filter cartridge and other replaceable elements, tightness of its connections with the inlet manifold, minimum length of connecting pipes. The air is supplied to the filter by a special hose from the vehicle's surroundings, and the air intake is located in the front of it.

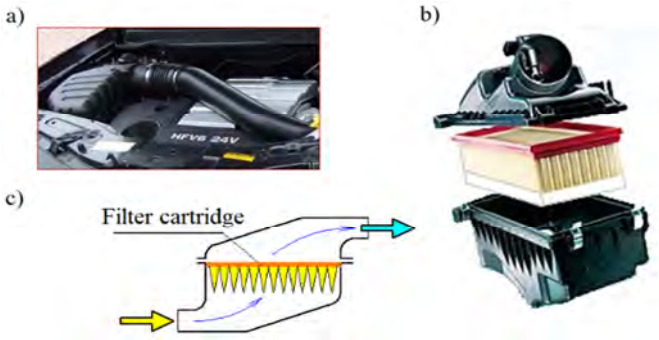

Fig. 1. Air filter in a modern passenger car: a) location of the air filter in the engine compartment, b) filter components, c) functional diagram [18]

A characteristic feature of partition filters is that during operation, as a result of the deposition and accumulation of dust particles in the filter bed, the filter pressure drop Δp_f, defined as a drop in static pressure behind the filter, systematically increases its value (Fig. 2).

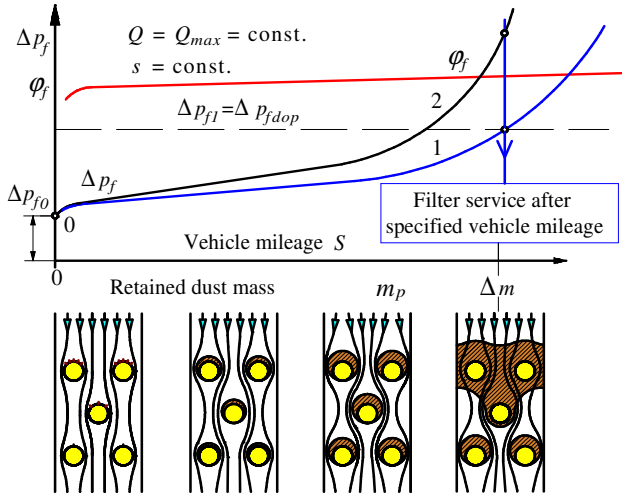

Fig. 2. Changes in separation efficiency and pressure drop of the partition air filter during operation: 1 – low air dustiness, 2 – large air dustiness

This causes additional engine energy losses. Intensity of increase in pressure drop depends on the conditions in which the vehicle is operated, mainly on the dust concentration in the air and the vehicle (engine) operating time. It is assumed that during operation, the air filter pressure drop should not exceed the permissible value Δp_{fdop}, which is determined from the condition of a 3% decrease in engine power and is at the level of 2.5–4.0 kPa – passenger car engines, 4–7 kPa – truck engines [3] and 9–12 kPa – special purpose vehicles [6]. From a technical point of view, service life of an air filter is commonly defined as the restriction level that causes the pressure on the passenger car filter to drop by about 2.5 kPa above pressure drop of the new (clean) filter. For trucks and special vehicles, the Δp_{fdop} values are assumed to be approximately 6.25–7.5 kPa above pressure drop of clean air filter [37]. Therefore, efforts are made to minimize pressure drop of clean air filters, which will reduce engine energy losses and extend the vehicle's mileage.

Dominant filter material used for operating fluids separation in vehicles, and in particular for intake air filtration of modern motor vehicle engines, are filter papers. They combine work of the way nets and nonwovens.

Filter papers are characterized by the following basic parameters: weight, paper thickness, average pore size, fiber diameter, dirt absorption, air permeability [5, 11].

As a result of continuous technological development of car engines, they are equipped with newer and newer systems and devices, for example an air conditioning system, a turbocharger, as a result of which the space available for the air filter is reduced. This results in a reduction in the filter area that can be used and an increase in separation speed and pressure drop, resulting in a loss of engine energy. For filter paper used in car air filters, maximum separation speed should not exceed the permissible value (0.08–0.12 m/s) [12, 21]. Exceeding this value is not only related to energy losses, it may also result in a decrease in separation efficiency due to bouncing and re-entrainment of particles [31].

Separation speed is defined as the average speed of the air stream flowing through the surface of the filter medium and it is determined from:

$$\upsilon_{Fmax} = \frac{Q_{Fmax}}{A_c \cdot 3600} \text{ [m/s]} \tag{1}$$

where: Q_{Fmax} – maximum air stream flowing through the filter element, equal to the air demand by the engine Q_{Silmax} [m^3/h] at the rotational speed of maximum power and 100% of the mixture throttle opening (engines with SI), A_c – active filtering area of the cartridge [m^2].

Due to limited available space for mounting the filter in the space around car engine, filter paper or non-woven filter cartridges are made in a pleated form (Fig. 3), from which the filter cartridge can then be assembled in various ways. Most often they are panel inserts (Fig. 3d).

Filter cartridge is shaped so as to obtain the largest filter surface of the paper with the minimum volume of the cartridge and at the same time maintaining the condition of the maximum permissible air flow velocity through the filter bed – separation speed υ_{Fmax}. This goal is achieved through the appropriate selection of the main design dimensions of the insert (Fig. 4) [16, 51]:

– pleat height b_p,

– pleat width a_w,
– spacing between pleats t_p (most often t_p = 2.2 mm),
– insert length L_p.

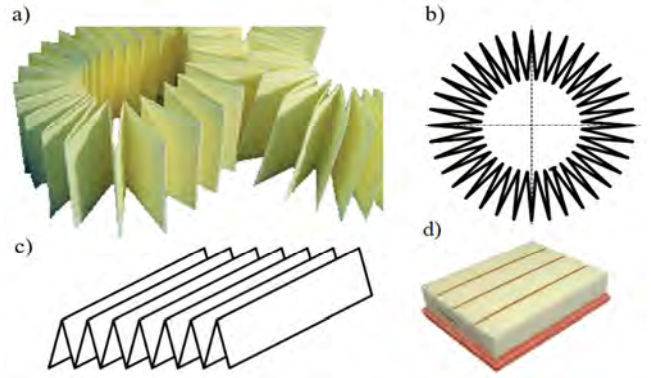

Fig. 3. Shaping the filter paper: a) paper after pleating, b) shaping into a multi-arm star, c) shaping into a panel, d) panel filter cartridge

At the same time, pleated paper filter elements should be constructed in such way that, with given design dimensions of the element and the required surface of the filter paper, they have maximum separation efficiency, minimum pressure drop and maximum durability.

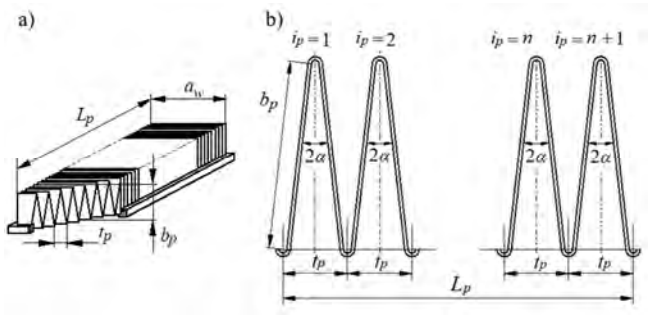

Fig. 4. Filter bed geometry: a) pleat geometry, b) i_p – number of pleats, L_p – insert length, a_w – pleat width, b_p – pleat side height, t_p – pleat width, α – half pleat inclination angle

Number and height of pleats and the spacing between the pleats (half-pleat angle) are the main parameters determining the surface of the filter paper, which is determined by:

$$A_c = 2h_p \cdot a_w \cdot t_p \cdot i_p [m^2] \quad (2)$$

Insert width a_w and its length L_p are limited by the size of the filter. A limited number of pleats can be placed at a given length L_p and with a fixed spacing of the pleats t_p. Separation area can be increased by extending the side of the pleat b_p, which will lower separation speed value and pressure drop, but only to a certain value, because too high pleats are unstable, they warp and touch each other, causing separation surface loss. Separation area can be increased by increasing the number of pleats on a given section, which will reduce the flow velocity and lower the pressure drop, but also here there is a certain limit number of pleats, exceeding which will increase pressure drop. In the available literature, there is a significant number of works presenting the results of air filters optimization mainly in the direction of minimizing the pressure drop, which determines the engine energy losses. In the process of optimizing pleated engine air filters, separation efficiency is also taken into account.

Pleated air filters have been studied both numerically and experimentally by many researchers. It turned out that each pleated filter had the optimal number of pleats at which it showed a minimal pressure drop [1, 7, 10, 40, 41, 49, 53].

For example, the numerical studies performed by Fotovati et al. [20] showed that there is an optimal number of pleats for clean filters for which the pressure drop reaches a minimum, regardless of the orientation of the fibers in the surface. The triangular pleats result in a lower pressure drop. After allowing for particle deposition, the intensity of the pressure drop increase decreases as the number of pleats increases. Greater number of pleats results in a greater flow velocity inside the pleat channels, which results in a greater heterogeneity in the deposition of dust on the pleat. It has been observed that this effect is less visible when the pleats are triangular in shape. The authors [10], on the other hand, optimized the geometry of car filter pleats using the developed dimensionless model. The pressure drop on clean pleated filters was determined taking into account the geometric characteristics of the pleats (distance between pleats 1–3.5 mm, pleat heights 27, 32, 40, 48 mm and separation speed in the range of 0.01–0.1 m/s. that for a given pleat height and constant air stream, there is such a width between the pleats for which the pressure drop reaches the lowest value. Park et al. [38] conducted research and various samples optimization of pleated filter elements by changing the angle between the pleat sides, the pleat length and the number of pleats. Highest separation efficiency was obtained when the dimensionless pleat coefficient defined as the quotient of pleat height (vertical distance from the top of the pleat to the base) and the pleat pitch (the distance between pleat apexes) was 1.48. Above this value, a systematic increase in the filter pressure drop was noted. Jinrui et al. [24] built a three-dimensional model of a pleated air filter on the basis of a real meltblown fiber, taking into account different filter parameters: pleat angle, layer thickness, diameter and number of fibers and curvature. It was found that at the stage of simulating pleated material separation characteristics, pressure drop increases nonlinearly with the increase of the deposited particles at the same gas inlet velocity. Maddineni et al. [31] numerically analyzed the phenomenon of particles permeating through a pleated panel-type air filter bed with a fleece height of 26 mm, pleat spacing of 4.5 mm and an angle between the pleat sides of 2.5 degrees. A series of ISO 12103 A2 fine dust tests were carried out. An increase in particles penetration was found as a result of their rebound and retention at speeds above 0.5 m/s. Li et al. [27] investigated the influence of pleat geometry and their dust load on the pressure drop of pleated air filters. Six types of test chambers were designed with different pleat ratio with the same pleat side length. Analysis of experimental data showed that the effective separation area was mainly influenced by the pleat ratio, therefore it should be kept below 1.59. Chen et al. [8] carried out the simultaneous optimization of pressure drop

and separation efficiency of pleated bed, adopting filter quality factor as the filter optimization and evaluation criterion, which combines separation efficiency and the pressure drop with:

$$q = \frac{-\ln(1-\varphi_c)}{\Delta p} \text{ [1/kPa]} \quad (3)$$

where: φ_c – cyclone separation efficiency, Δp – pressure drop for the nominal air stream [kPa].

They found that with the increase in the number of pleats, the value of the quality factor q initially increased and then decreased. It was established that two parameters are decisive for this: number of pleats and their height. It has been shown during the research that the effectiveness of pleated filters depends not only on the particle size, but also on the number of pleats in the filter. Based on the filter quality factor, it has been found that the optimal number of pleats is always higher (about 0.3–0.5 pleats per 10 mm) than the one based on the pressure drop. The filter with the highest quality factor of the filter was obtained by the filter having a pleat number of 2.65 per 10 mm with a particle diameter of 122 nm. Whereas Théron et al. [52] performed a numerical and experimental evaluation of the influence of pleat geometric features on the properties of fibrous filters in the deep separation phase of submicron aerosols. Wiegmann et al. [54] simulated a pleated air filter with various pleat shapes and different filter materials and assessed their impact on pressure drop. In [1], an experimentally and numerically tested pleated air filter with different parameters was carried out and its optimization aimed at improving the performance of a compression-ignition engine was carried out. A number of parameters were investigated including; pleat height, pleat spacing, pleat shape, filter medium thickness, air flow speed, engine speed, engine torque, fuel consumption and dust load. Three different shapes of pleats were considered: flat pleats, V-shaped pleats and sinusoidal pleats. Lowest pressure drop was obtained for a filter with a sinusoidal pleat shape, and the highest for a filter with a flat pleat shape. Reduced spacing of the pleats additionally resulted in a greater pressure drop of about 18%, while an increased height of the pleats or the thickness of the pleat led to a reduction in pressure drop of about 43% and 10%, respectively. Filter loaded with dust resulted in greater pressure drop and greater fuel consumption for the same engine torque and rotational speed. Engine with optimized filter achieved the lowest exhaust gas temperature of 218°C, while the exhaust gas temperature with the standard filter reached 233°C, but the highest exhaust temperature of 250°C was achieved by the engine with a dirty air filter. Mahesh [29] performed an analysis of fluid flow through the pleated air filter of a four-cylinder spark ignition engine by performing experimental and computational fluid dynamics (CFD) analysis to reduce pressure drop. It was found that a filter with triangular pleats achieves greater separation efficiency and lower pressure drop than a filter with rectangular pleats. Saleh and Tafreshi [43] carried out numerical studies in the field of pressure drop and separation efficiency of an air filter having a different number of rectangular and triangular pleats, both in depth and surface separation regimes with particles with a diameter of 1.5 and 10 μm and in the range of separation speed 0.5–5 m/s. It has been shown that filters with rectangular pleats have the potential to provide better performance than their triangular counterparts under high dust loads. Rebai et al. [41] found that the optimal number of pleats resulting from the clean-state filter pressure drop tests was significantly lower than that based on dust mass retained in the filter. Fotovati et al. [19] investigated pleated bed geometry influence on dust deposition mechanism in pleats, as well as the pressure drop and separation efficiency related to it. They conducted numerical tests keeping the pleat height constant. Feng and Long [17] developed a macro-scale CFD simulation to investigate the optimal design of a pleated air filter under dust load conditions. It has been found that the optimal pleat density in a clean state can lead to a higher pressure drop and energy consumption during the dust separation process. It has been observed that the optimal dust deposition due to the pleat density depends on pleat height and is lower with higher height of the pleat. Maddineni et al. [30] numerically analyzed penetration phenomenon and particles penetration on a pleated, panel-type air filter with a pleat height of 26 mm, pleat spacing of 4.5 mm and a pleat angle of 2.5 degrees. ISO 12103 A2 fine-grained dust was used, the concentration of which was 0.2 g/m^3 and different separation speeds in the range of 0.05–0.5 m/s. It was found that at low speed, i.e. 0.1 m/s, all particle sizes showed better separation. At high speed, i.e. 0.5 m/s, all particles showed minimal particle penetration. At velocities above 0.5 m/s, the amount of particles downstream of the filter material was found to increase, which meant very high particles penetration. For example, [32] presents the numerical methodology of forecasting the pressure drop in air filter with a pleated filter element. The pleat geometry and inlet velocity have been found to be the key parameters for the optimization of filter elements. The optimal pleats pitch was determined to obtain a minimum pressure drop and found to be largely dependent on pleat height. In [33] pleated air filter made of cellulose fibers has been analyzed in terms of optimal pleat geometry taking into account separation efficiency and pressure drop. The following pleat spacings were tested: 2.5, 3.0, 3.5, 4.5 and 5.5 mm and three levels of their height: 10, 20 and 30 mm. The optimal pleat geometry was found at a pleat height of 30 mm and with a spacing of 4.5 mm. After soaking with oil, the pleated filter element with optimal pleat geometry showed a significant increase in separation efficiency at the expense of a slight increase in pressure drop. Compared to the contaminated pleated filter element, the oil-soaked filter exhibited higher separation efficiency at a higher air flow rate. The research [26] focused on examining the effect of pleated filters' properties and pleat geometry on pressure drop and separation efficiency, but also on air velocity distributions. It was found that both the geometry of the pleats and the pleat stabilization technique, which is commonly used in pleated filters, to maintain the shape of the pleat and the distance between the pleats, were influenced. Results suggest that in addition to the pleated filter geometry described by the shape of the pleat and its height, pleat density, geometric effects of blocking the pleats or their stabilization techniques should also be considered to estimate the flow effects in a more realistic way. The authors

[35] assessed the optimal pleating geometry on the basis of separation quality coefficient q, taking into account separation efficiency and the filter pressure drop. One flat filter and eight pleated filters (4, 6, 8, 10, 15, 21, 25, 30 pleats) with pleat height of 29 mm and pleat width of 105 mm were prepared, and their separation efficiency and pressure drop were determined. It was found that the pressure drop of pleated filters with the number of folds above 21, at the same air flow rate, increased with the number of pleats, which resulted from the increased separation speed due to the reduction of the effective separation area. On the other hand, pleated filter separation efficiency for particles (30, 50, 100, 200 nm) increased with the increase in the number of pleats. Moreover, the highest filter quality factor q = 5.8 with a pleat height of 29 mm was found for the number of pleats of 21, which translated into the optimal pleat geometry.

From above considerations we found out that the problem of selecting pleated filter elements for an internal combustion engine is actual. Presented research shows that the effectiveness of a filter is determined by its geometry. The aim of this study was to verify the basic criterion for selecting a pleated air filter for an engine, which is separation speed υ_F. Research was carried out by analyzing the geometry of pleated filter cartridges from several passenger car engines. Actual filter paper area of the panel inserts was determined as well as separation speed, which was compared with the permissible value of υ_{Fmax} applicable in the automotive industry.

It follows from above considerations that the problem of selecting pleated filter elements for internal combustion engine is actual. Presented research shows that the effectiveness of the filter (efficiency and pressure drop) is largely determined by the geometry of the pleated filter element and its surface. Characteristic parameter of the partition filter is permissible separation speed υ_{Fmax}, which is the basic criterion for selecting a pleated filter element for a car engine air filter. Aim of this study was to verify this criterion and to analyze the factors determining the value of the distance traveled by the car until the filter obtains permissible pressure drop. In order to achieve the goal, the geometry of 44 pleated filter inserts for car engine filters was analyzed. Actual area of filter paper of the panel inserts was determined and separation speed was calculated for the rated engine operating conditions, and then compared with the permissible value of υ_{Fmax} applicable in the automotive industry. Theoretical relationship was used to analyze the factors determining the value of the distance traveled by the car until the filter obtained permissible pressure drop, which takes into account several experimentally determined factors.

2. Model methodology and experimental research

2.1. Model research purpose and subject

The aim of the research was to determine separation speed in dozens filter elements used in passenger car filters of various brands. Car engines differed mainly in the displacement and engine power as well as maximum power rotational speed–rated speed.

Research subject were panel-shaped, flat, cuboid-shaped filter elements made of pleated filter paper. These are typical passenger car filter elements, differing in main external dimensions, pleats number, and thus filter paper surface (Fig. 5).

Fig. 5. Types of air filter elements: a) paper filter element, b) non-woven filter inserts

Basic criterion for selecting an active filtering surface A_c for a car air filter is the maximum separation speed υ_{Fmax}, which for filter paper should be within the range [20, 44–46]:

– 0.06–0.12 m/s – passenger car filter elements,
– 0.03–0.06 m/s – trucks and special vehicles filter inserts.

For a given maximum separation speed υ_{Fmax}, the active separation area is then determined from:

$$A_c = \frac{Q_\upsilon(Q_N)}{3600 \cdot \upsilon_{F\,max}} [m^2] \tag{4}$$

This is the minimum required surface area of the filter paper. The use of a larger surface of the paper in the air filter automatically reduces separation speed, which will have a positive effect on the separation process (increase in efficiency and decrease in pressure drop) and extend the time to achieve the permissible pressure drop of the filter.

In order to obtain knowledge about the actual separation speeds in air filters used in car engines, it is necessary to know the active surface area of the filter material A_c and the maximum value of the air stream flowing through this element Q_{Fmax}, which is equal to the air demand of the engine during its operation under rated conditions. For this purpose, measurements of the geometry of 44 pleated filter inserts from passenger car engine filters were performed, and then their actual filter paper surface was determined from relation 2.

The maximum air demand of the Q_{Silmax} motor can be determined experimentally under laboratory conditions. It is the most reliable method, but also expensive and time-consuming. For the comparative analyzes carried out in this study, the maximum air demand by the engine $Q_{Silmax} = Q_\eta$ was determined using the theoretical relationship [39]:

$$Q_{Sil\,max} = Q_\eta = \frac{V_{ss} \cdot n_N \cdot \eta_\upsilon \cdot 60}{1000 \cdot \kappa} [m^3/h] \tag{5}$$

where: V_{ss} – engine cubic capacity [dm^3], n_N – maximum power rotation speed [rpm], κ – stroke number factor (2- for four-stroke engines, 1 – for two-stroke engines), η_υ – filling factor, the value of which depends on the type of engine.

According to data from company Donaldson, when calculating the air demand of the engine, the filling factor η_υ of engine cylinders can be assumed as follows [15]:

– 0.85 – four-stroke diesel and SI naturally aspirated engines;
– 1.60 – four-stroke turbocharged diesel engines;
– 1.85 – four-stroke turbocharged diesel engines with an intake air cooler;

Maximum air stream Q_{Silmax} flowing through the filter element can also be determined on the basis of the rated engine power using the following equations [15]:

$$Q_{Silmax} = Q_N = N_e \cdot Q_{js} \text{ [m}^3\text{/min]} \quad (6)$$

where: N_e – maximum engine power [HP], Q_{js} – air flow [m^3/min] per 1 HP of engine power.

Value of the air stream Q_{js} per 1 HP of engine power is recommended to be assumed as follows [15]:

- 0.057 m³/min for 4-stroke naturally aspirated diesel engine,
- 0.065 m³/min for 4-stroke turbocharged and cooled engine,
- 0.093 m³/min for 2-stroke diesel engine with dust extraction by blower.

2.2. Test results and calculations

Figure 6 shows values of the nominal air stream flowing through 44 filter inserts from passenger car engine filters. Air stream Q_η and Q_N values were calculated using the filling degree criterion (relationship 2) and the power criterion (relationship 3).

Data for diesel and SI, naturally aspirated and turbocharged engines with and without charge air cooling were used for the calculations. Hence, the values of air flows obtained as a result of calculations for different engines with the same displacement V_{ss} differ significantly. Moreover, values of nominal air demand by passenger car engines calculated with the filling criterion Q_η reach values on average 5% lower than those calculated with the power criterion Q_N.

For example, the nominal air demand of a four-stroke engine with SI (V_{ss} = 1.598 dm^3 – No. 13 Fig. 6) of Opel Astra F Sedan 1.6 l has values Q_η = 211.9 m^3/h and Q_N = 231.6 m^3/h, respectively. The difference between the two values is insignificant and is R_Q = 8.6%. For a four-stroke engine with SI of the same displacement (V_{ss} = 1.598 dm^3 – No. 12 Fig. 6) with a turbocharged Ford Fiesta III Hatchback 1.6 l Turbo, the air demand is Q_η = 487.8 m^3/h and Q_N = 528.1 m^3/h. The difference between the two values R_Q = 7.8%. For the Ford Fiesta III Hatchback 1.6 l Turbo engine, the air flow rates Q_η and Q_N are 50% higher than for the Opel Astra F Sedan 1.6 l with the same V_{ss} engine but without turbocharging.

Engine air demand Q_η, determined according to the engine filling criterion, is calculated on the basis of the engine design parameters and the filling degree η_υ. Value of η_υ is assumed depending on the engine type (diesel and SI): naturally aspirated, turbo charged or turbo charged with an intercooler. The recommendations say nothing about a drop in the fill level value in case of excessive wear of cylinders, which also affects power loss. Engine power is determined not only by the mass and type of fuel burned, but also by the process of preparing the combustible mixture, including air turbulence, injection, fuel fragmentation and evaporation, as well as the course of combustion of the mixture and fuel-air mixture. Air flow meter in the intake system is one of many sensors that provide signals on the basis of which the on-board computer selects the optimal operating conditions for the engine. In engines with the same cubic capacity and the same degree of cylinder filling, these processes may occur with different intensity, and thus the power obtained may have a different value. Therefore, the method of determining the air flow from the obtained engine power gives higher values than the method using the degree of filling. For analyzes in the further part of the thesis, the air stream was used, determined on the basis of the effective power of new engine, provided by the manufacturer.

Figure 7 shows, for comparison, the actual surface area A_R of the filter inserts paper in passenger cars and the calculated area A_N for the air stream Q_N resulting from the maximum power and permissible separation speed υ_{Fmax} = 0.12 m/s. Figure 7 shows that in most cases the actual (active) filtering surface A_R of the cartridges is greater than the calculated A_N surface from the Q_N stream and the permissible separation velocity condition υ_{Fmax} = 0.12 m/s. This indicates the correct selection of the filter surface and air filters for the vehicle.

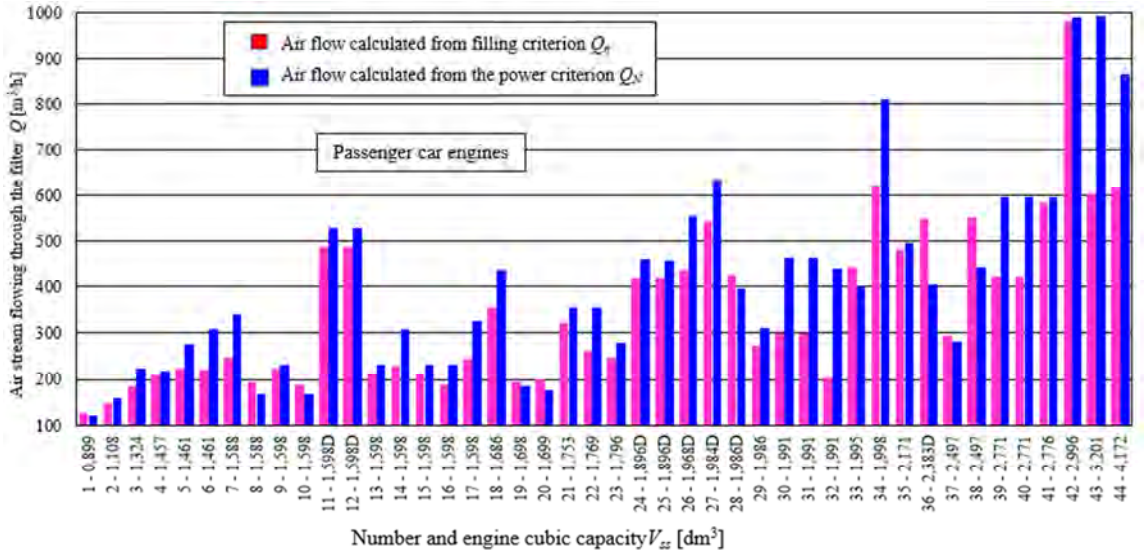

Fig. 6. Nominal air stream Q_η, Q_N values flowing through the filter elements in engine filters of different capacity

Figure 7 shows, for comparison, the actual surface area A_R of the filter inserts paper in passenger cars and the calculated area A_N for the air stream Q_N resulting from the maximum power and permissible separation speed υ_{Fmax} = 0.12 m/s. Figure 7 shows that in most cases the actual (active) filtering surface A_R of the cartridges is greater than the calculated A_N surface from the Q_N stream and the permissible separation velocity condition υ_{Fmax} = 0.12 m/s. This indicates the correct selection of the filter surface and air filters for the vehicle.

The air filter elements of engines No. 8, No. 16, No. 25 and No. 26 (Fig. 7) have actual separation surface A_R significantly (2–3 times, and the engine air filter element No. 8 – four times) larger than the surface of A_N. Thus, the actual separation speed in these filter elements has a much lower value, respectively: υ_{FR} = 0.028 m/s, υ_{FR} = 0.041 m/s, υ_{FR} = 0.079 m/s, υ_{FR} = 0.075 m/s. Lower air flow velocity through the filter paper means lower pressure drop (lower engine energy losses) in the engine intake system and higher cylinder filling. Larger filter surface of the cartridge means its greater dust capacity, which will ensure a longer service interval of the car. In the case of the cars we discuss, there is a place nearby the engine that allows for placing an air filter with an element with such a large filter surface. On the other hand, in the case of engine filters No. 11, No. 12, No. 34, No. 42 and No. 43 (Fig. 7), the actual separation area A_R is much smaller than the A_N area resulting from the condition of the permissible separation speed υ_{Fmax} = 0.12 m/s. Engines mentioned are supercharged engines which have significantly more power than similar naturally aspirated engines with the same cubic capacity. In the case of the filters mentioned, the designer did not take care of the proper selection of engine filter. This will result in increased pressure drop in the engine intake system and additional energy losses, especially in case of loading filter bed with dust.

Figure 8 shows values of separation speed υ_N calculated on the basis of the power criterion and the actual (active) separation surface A_R in passenger car filter inserts.

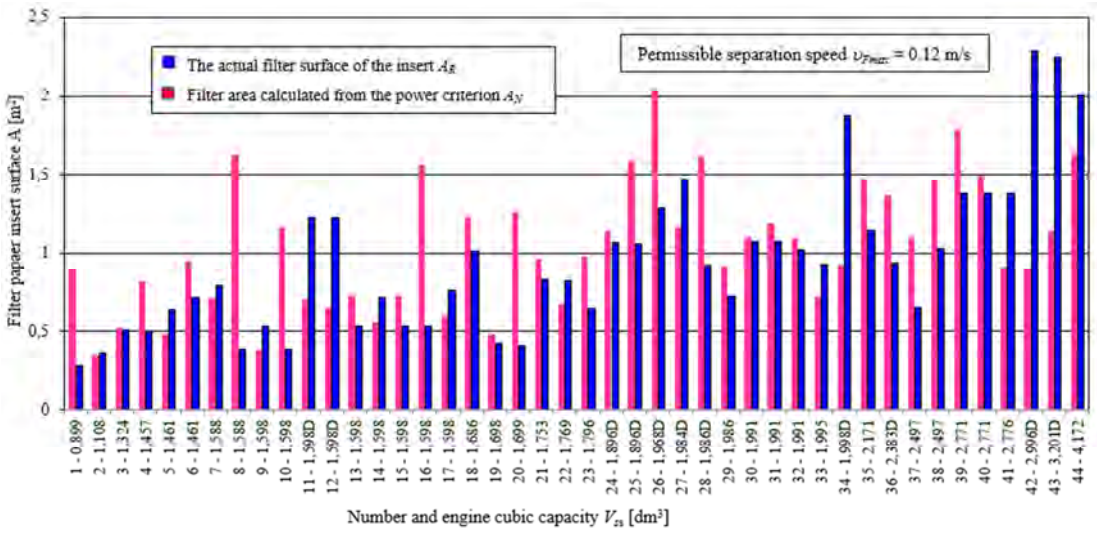

Fig. 7. Comparison of the paper surface used in passenger car engine filter inserts: the actual A_{rz} and the calculated A_N for the separation speed υ_{Fmax} = 0.12 m/s

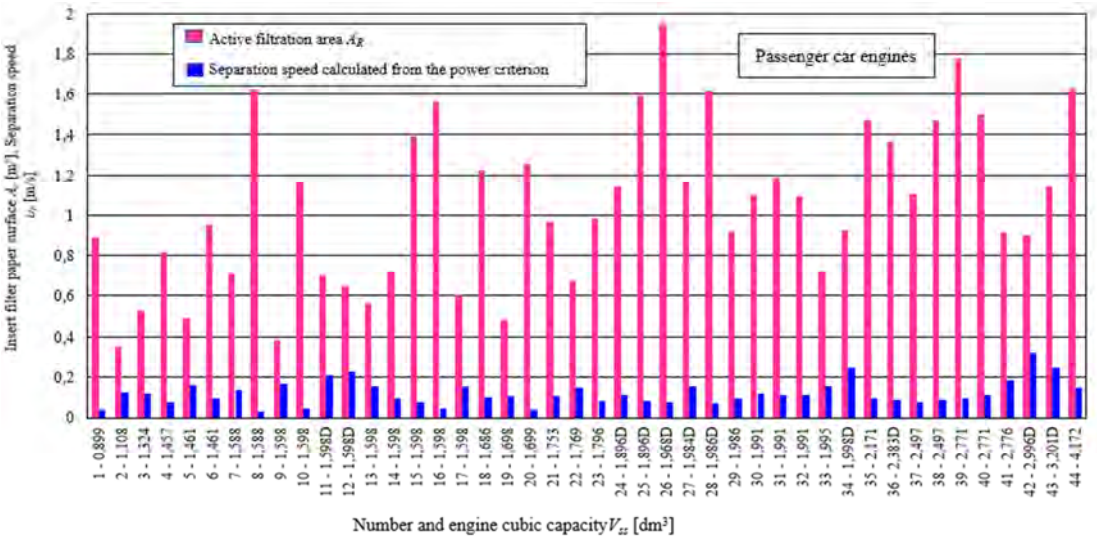

Fig. 8. Separation speed υ_N calculated on the basis of power criterion and active filtering surface A_R in passenger car filter inserts

In most cases (62%) of analyzed filter inserts, the calculated separation speeds are within the range of υ_{Fmax} = 0.06–0.12 m/s recommended by the designers. The highest separation speed υ_F = 0.324 m/s is characteristic for the BMW Z4 E85 3.0 SI passenger car insert (No. 42). It is a sport car with a power of 194 kW, a cubic capacity V_{ss} = 2.996 dm^3 and an active filter area A_c = 0.901 m^2. In order that separation speed for this element did to exceed the permissible value υ_{Fmax} = 0.12 m/s, the active separation area should be increased to A_c = 0.901 m^2, i.e. almost three times. The actual filter surface used is likely to depend on the space available in the engine compartment to accommodate the air filter with the appropriate paper surface value.

Permissible speed value (υ_{Fmax} = 0.12 m/s) was also exceeded in the Opel Calibra I 2.0i Turbo 4×4 passenger car filter (No. 34). It is a vehicle with lower power (150 kW) and a smaller engine cubic capacity (V_{ss} = 1.998 dm^3) compared to the engine from previous vehicle, but the active separation area is only A_c = 0.928 m^2, which results in separation speed of υ_F = 0.243 m/s. Similar significant excess of permissible speed value occurs in air filters in supercharged engines No. 11, 12 (Fig. 8).

On the other hand, air filter from Audi A4 B7 Sedan 2.0 TDI passenger car (No. 26), despite significant power (103 kW) and cubic capacity (V_{ss} = 1.968 dm^3) similar to the engine of the previous vehicle, reaches separation speed of υ_F = 0.0753 m/s, within the required range υ_{Fmax} = 0.06–0.12 m/s, which results from significant filter paper surface area (A_c = 1.95 m^2) used in this filter. Probably in the case of this car, nearby the engine, there is a place for placing an air filter with an element with such a large filter surface. A similar situation occurs in the case of Fiat Seicento 0.8 (No. 1), Volkswagen Golf II 1.6 (No. 8), Opel Kadett D (No. 10), Seat Cordoba II 1.6 (No. 16) and Opel Kadett E Estate (No. 20), where separation velocities are significantly lower than 0.06 m/s. Engines of the above-mentioned cars have much lower power, which is in the range of 28.68–55.15 kW, than the engines from previous vehicles. It follows that an important factor determining the surface of the filter paper is the free space around the engine where it is possible to locate the air filter. Analysis shows that there is more of this free space in cars where the power unit is low-power engine.

Figure 9 shows values of separation speed in naturally aspirated engines with the same cubic capacity V_{ss} = 1.598 dm^3 in following cars: Volkswagen Jetta II (No. 9), Opel Corsa A (No. 13), Opel Astra F (No. 14), Opel Zafira B (No. 15) and Seat Cordoba II (No. 16). Car engines 9, 14 and 16 also have the same power 55.15 kW, and thus the value of the stream, but due to the different value of the active surface of filter paper of the cartridge, the separation speeds reach various values, respectively υ_F = 0.167, 0.89, 0.041 m/s.

Similarly, in the case of car engines No. 13 and 15. Despite the same cubic capacity V_{ss} = 1.598 dm^3 and slight differences in power, the separation speeds differ twice (Fig. 9). In the air filters in engines 9 and 13, the separation speeds significantly exceed the permissible value υ_{Fmax} = 0.12 m/s. This is a clear proof that the rules for selecting air filters are not followed. For the vehicle user, these are energy losses in the form of power loss, increased fuel consumption and reduced vehicle acceleration.

2.3. Factors determining distance value traveled by a car

Selection of active separation surface A_c according to the criterion of maximum separation speed υ_{Fmax} is not a sufficient condition. It is necessary to check whether the A_c surface selected in this way will ensure the required operating time of the air filter corresponding to the assumed vehicle mileage until the service is performed – filter insert replacement. It is assumed that this is the time when the filter reaches the permissible resistance Δp_{fdop}, which results from the assumed 3% decrease in engine power.

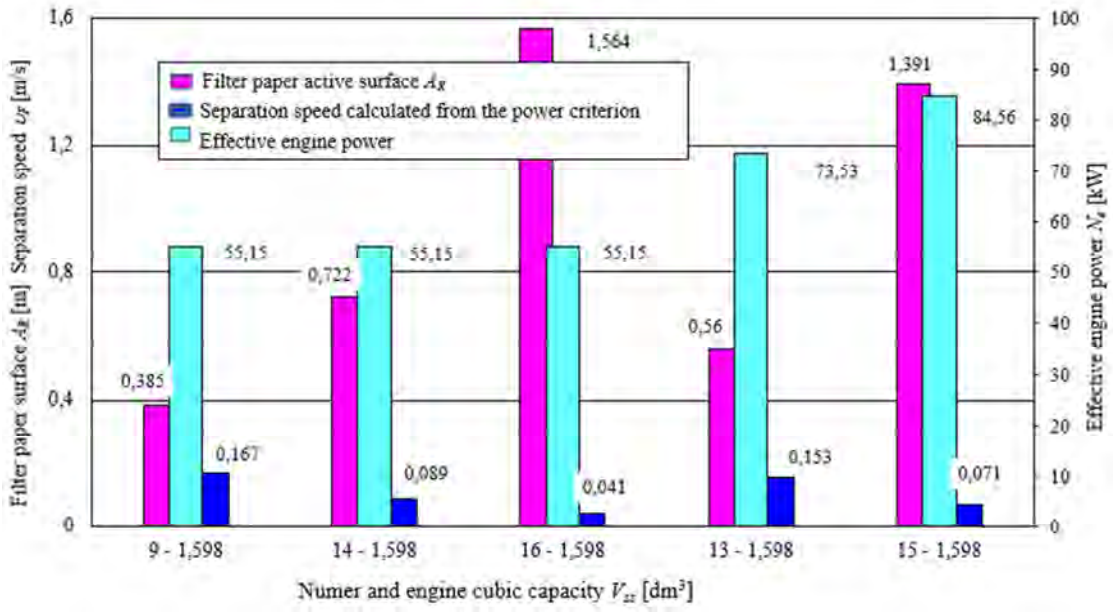

Fig. 9. Separation speed υ_N calculated from the power criterion and the actual separation area A_R for passenger cars with cubic capacity V_{ss} = 1.598 dm^3

The distance traveled by the car until the filter reaches the assumed value of permissible resistance Δp_{fdop} is determined by:

$$S_p = \upsilon_p \, \tau_p \, [km] \tag{7}$$

where: υ_p – average vehicle speed [km/h], τ_p – air filter operation time until the filter reaches the accepted value of permissible resistance Δp_{fdop}.

Operation time τ_{pI} of a single-stage air filter can be determined from [7]:

$$\tau_{cpI} = \frac{A_c \cdot k_m \cdot k_c}{Q_{sil\,max} \cdot s \cdot \varphi_p} [h] \tag{8}$$

where: k_m – filter paper absorbency coefficient [g/m^2], k_c – coefficient taking into account the difference between the parameters of test pollutants and actual pollutants, Q_{Silmax} – nominal air demand by the engine [m^3/h], s – average dust concentration in the air sucked in by the filter [g/m^3], φ_P – filter element efficiency.

After taking into account the above dependence, the distance traveled by the car until the one-stage filter reaches the permissible resistance Δp_{fdop} is determined by:

$$S_p = V_p \frac{A_c \cdot k_m \cdot k_c}{Q_{sil\,max} \cdot s \cdot \varphi_p} [km] \tag{9}$$

Vehicle mileage calculation from the above dependence requires a lot of experimental data that characterizes a specific filter material under specific operating conditions, the most important of which are: absorption coefficient k_m, material separation efficiency φ_P, correction factor k_c, dust concentration s, chemical and duct particle size composition, air flow speed (air stream).

Factor k_c takes into account mainly the influence of soot on the durability of the paper element, and it is determined by the ratio of filter operation time in real conditions to the filter operation time with test dust [34]. The significance of this coefficient, which assumes the value of $k_c < 1$ (the higher the soot content, the lower the k_c coefficient value, and the filter's working time is shorter), is large in the case of air filters with a paper element, which are equipped with vehicles operated in urban conditions, where soot is the predominant component of the engine intake air pollutants. In the case of vehicle engines operated in off-road conditions, the basic pollutant component is mineral dust, so taking into account the k_c coefficient when determining the operating time of a two-stage filter can be omitted, because the test dust is similar to mineral dust in both chemical and particle size composition. Therefore, it should not have a significant impact on the results of calculations, which are estimates.

According to the authors [14, 20], the k_m factor presented in the above equations is defined as: the quotient of the total dust mass m_{PF} retained and evenly distributed over the surface of the filter material until the permissible resistance value Δp_{fdop} and the active surface of the filter paper A_c is reached:

$$k_m = \frac{m_{PF}}{A_c} [g/m^2] \tag{10}$$

Values of dust absorption coefficient k_m for conventional filter materials based on cellulose and standard dusts, the grain size of which usually does not exceed 80–100 μm (dust with such grain size goes directly to the filter element of a single-stage filter) were determined by the authors based on experimental studies [12, 28, 32] and assume maximum values in the range of k_m = 190–220 g/m^2.

Modern filtering materials for engine intake air separation are also made of other materials, e.g. polyester, cellulose with an additional layer of polyester or nanofibers, cellulose with a layer of polyester and nanofibers. These materials are characterized by much greater efficiency and accuracy, but also by lower values of the absorption coefficient k_m. According to the research of the authors of the work [12, 13], filter materials with a pressure drop of Δp = 3 kPa obtained the following absorption coefficients: polyester k_m = 135 g/m^2, cellulose with an additional layer of polyester k_m = 120 g/m^2, cellulose with a layer of polyester and nanofibers k_m = 102 g/m^2.

According to the authors [28] who tested the two-layer filter medium, the absorption coefficient reached the value of k_m = 84 g/m^2 with a pressure drop of 2 kPa, when the microfiber layer was placed as an inlet. On the other hand, when there was a sub-microfiber layer at the inlet, the dust holding capacity was 95 g/m^2, so it was 13% higher.

For filtering nonwovens used as filter elements for passenger car engines, the dust absorption coefficient k_m assumes much higher values (k_m = 350–500 g/m^2) than the filter paper, which may result from the greater thickness (2–5 mm) of the filter bed. For example, in [42] it is stated that the value of the absorbency coefficient of non-calendered nonwoven fabric with a thickness of 3.2 mm, determined at pressure drop of 0.3 kPa, is k_m = (54.5–89.3) g/m^2. The same non-woven calendered fabric has the absorption coefficient k_m = (85.5–112.3) g/m^2, and therefore it is much higher. The authors [11] state that the dust absorption coefficient of filtering nonwovens with a gradient structure has the value of k_m = (900–1100) g/m^2. However, the value of the pressure drop at which the k_m value was determined was not given. According to [58], the dust absorption coefficients of nonwovens fabrics exceed the value of (400–480) g/m^2.

Modern filtering materials for filtering engine intake air are also made of other materials, e.g. polyester, cellulose with an additional layer of polyester or nanofibers, cellulose with a layer of polyester and nanofibers.

2.4. Dust absorption coefficient experimental studies

Research purpose and subject

The aim of the research was to determine filter cartridges dust absorption coefficient k_m made of various filter materials (cellulose, polyester, cellulose and polyester, cellulose and polyester with a nanofiber layer by determining the following separation characteristics:

- separation accuracy $d_{zmax} = f(k_m)$,
- separation efficiency $\varphi_w = f(k_m)$,
- pressure drop $\Delta p_w = f(k_m)$.

and flow (aerodynamic) characteristics $\Delta p_w = f(Q_w)$, where: Q_w – air stream flowing through filter element.

Research subject were filter inserts (Fig. 10) of the same type, with the same dimensions, same filtration area A_w = 0.1534 m^2, but with different filter material. To facili-

tate test results analysis, filter materials (cartridges) have been designated A, B, C, and D.

Fig. 10. Filter cartridge

Characteristic parameters and values of the selected filter materials are summarized in Table 1. A large variation in the parameter values can be seen. Filter material D (cellulose + polyester + nanofibers) is characterized by five times less air permeability than material A and two times smaller than materials A and B in thickness. There is a nanofiber layer on the inlet side of the filter material D.

Table 1. Tested filtration materials parameters according to the manufacturer's data [12]

No.	Filtration material	Permeability q_p [dm^3/m^2/s]	Grammage g_m [g/m^2]	Thickness g_z [µm]	Max. pore size d_p [µm]
A	Cellulose	838	121	610	79
B	Polyester	150	180	550	–
C	Cellulose + polyester	150	130	350	58
D	Cellulose + polyester + nanofibers	185	120	300	48

Research methodology and conditions

Tests were carried out on the stand (Fig. 11), which was equipped with Pamas – 2132 particle counter. counter records dust grains number and size in the air stream Q_w after the tested filter cartridge in the range of 0.7–100 µm in i = 32 measuring intervals, limited by diameters ($d_{zimin} \div d_{zimax}$).

PTC-D test dust, which in Poland is a substitute for the AC fine test dust, the chemical and fractional composition of which is presented [39], is dosed into the housing, where the tested cylindrical filter cartridge is located. Dust grains mass fraction with a size of 0-5 µm in total dust mass is almost 40%. Due to their very small size, these dust grains are difficult to retain by porous filter materials. More than 67% of these grains are SiO_2 grains, a mineral characterized by high hardness (7 on the 10-degree Mohs scale), thus causing accelerated engine components wear.

At the appropriate distance behind the tested filter, the tip of the measuring probe is placed centrally along the axis of the conductor, which is used to suck air into the particle counter sensor. Measuring cable ends with a special filter that prevents dust from getting into the rotameter.

Filter inserts flow characteristics $\Delta p_w = f(Q_w)$ before the tests were determined for 8 measuring points in air stream range $Q_w = Q_{wmin}–Q_{wmax}$. Maximum stream value Q_{wmax} = 56 m^3/h was determined for maximum filtration speed υ_{Fw} = 0.1 m/s. For passenger car filters, maximum paper filtration speed value is within the range υ_{Fw} = 0.07–0.12 m/s [18, 20, 53–56].

Filter cartridge flow characteristics test results $\Delta p_w = f(Q_w)$ (before testing with dust) are shown on Fig. 12. As the air stream increases, flow resistance increases parabolic $\Delta p_w = f(k_m)$, which is consistent with the literature .

Highest flow resistance values in the entire range of the test air stream Q_w were recorded for the B insert. For Q_{wmax} = 56 m^3/h pressure drop of insert B has value Δp_w = 439.9 Pa (Fig. 12). Filter materials B and C achieve slightly lower pressure drop. Filter element made of material A, which is only a cellulose filter material, achieves the lowest pressure drop (Δp_w = 312 Pa) which results from material high permeability(838 dm^3/m^2/s).

Separation efficiency φ_w and pressure drop Δp_w characteristics depending on dust absorption coefficient k_m of tested filter inserts A, B, C and D are shown on Fig. 13. Observing change in separation efficiency φ_w in tested filter inserts, the work of the element can be conventionally divided into two stages. It was assumed that the first (I), initial operation stage of each filter cartridges, lasts until they achieve separation efficiency at the level of φ_w = 99.9%. This stage is characterized by a low initial efficiency and separation accuracy and low flow resistance.

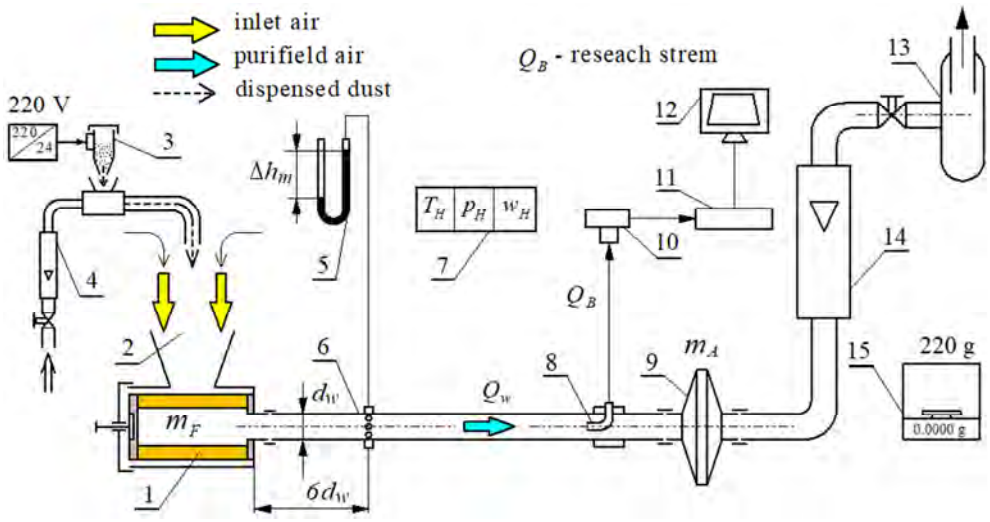

Fig. 11. Filter cartridge test stand functional diagram: 1 – filter cartridge, 2 – dust chamber, 3 – dust dispenser, 4 – rotameter, 5 – U-type manometer tube, 6 – measuring tube, 7 – humidity measurement set, ambient air temperature and pressure, 8 – measuring probe, 9 – absolute filter, 10 – sensor, 11 – particle counter, 12 – measuring computer, 13 – suction fan, 14 – rotameter, 15 – analytical balance

First (I) stage duration of operation varies and depends on filter material type. Step (I) takes longer the lower the initial separation efficiency is. Lowest initial separation efficiency ($\varphi_{w0A} = 96.3\%$) was recorded for filter cartridge made of A filter material (cellulose). The B, C and D cartridges have higher separation efficiency initial values, respectively: $\varphi_{w0B} = 98.9\%$, $\varphi_{w0C} = 98.2\%$, $\varphi_{w0D} = 99.8\%$ (Fig. 13).

As dust mass retained in filtration layer increases (k_m coefficient increases) separation efficiency in tested inserts assumes higher and higher values. Determined separation efficiency value ($\varphi_w = 99.9\%$ – end of period I) filter cartridges operating under same conditions (same dust concentration and air stream value) obtain after different time. Insert A achieves efficiency of $\varphi_w = 99.9\%$ after obtaining dust absorption coefficient $k_{mA} = 110.7$ g/m^2. For B, C and D cartridges made of other filter materials, the first stage lasts much shorter. Insert D, whose filter material is a bed (cellulose + polyester + nanofibers), achieves efficiency of $\varphi_w = 99.9\%$ with dust absorption coefficient value $k_{mD} = 7.22$ g/m^2.

In the second (II) stage of work, filter cartridges separation efficiency is maintained at a stabilized level $\varphi_w = 99.9\%$. For the A cartridge, at the end of its work, a slight but systematic decrease in separation efficiency is noticeable. In the last measurement, the effectiveness is $\varphi_w = 99.7\%$. This can be explained by the fact that a considerable dust mass in the form of expanded tree-like dendrites is accumulated on filter material fibers [57]. Dust grains at the very top of the dendrites are entrained and carried to filter material outlet side, from where they are entrained by the air stream flowing into the engine cylinders. Separation efficiency decrease phenomenon is related to dust particles maximum size, which assume larger values. After last measurement, value is $d_{zmaxA} = 16.7$ µm. For the remaining cartridges, maximum dust grain sizes d_{zmax} stabilize at much lower level. Behind insert D, where there is nanofiber layer, these are grains with sizes $d_{zmaxD} = 3.1$–5.1 µm.

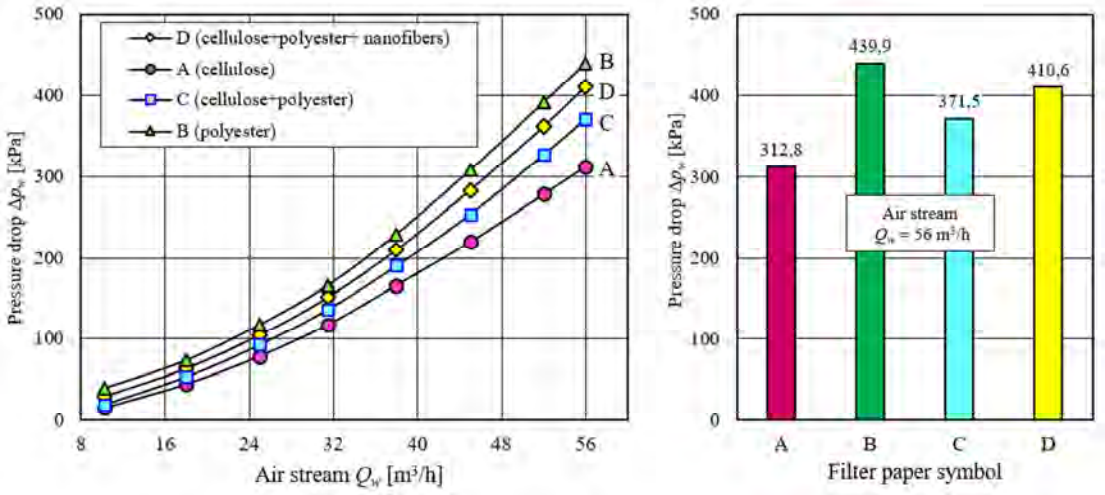

Fig. 12. Flow characteristics $\Delta p_w = f(Q_w)$ of tested filter cartridges A, B, C, D

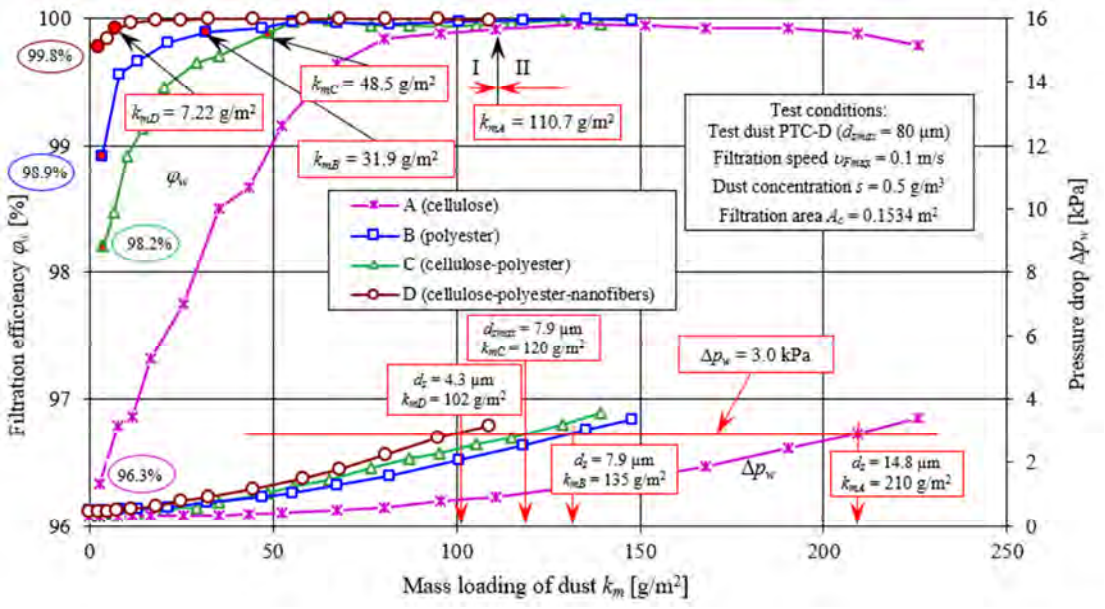

Fig. 13. Performance φ_w and pressure drop Δp_w characteristics depending on dust absorption coefficient k_m of tested filter cartridges A, B, C, D

Dust retention characteristic feature by filter materials is continuous increase in pressure drop. Due to its negative impact on the engine operation, its limitation in the form of permissible resistance is applied. For passenger car engines, the value is 3 kPa. Figure 13 shows that for this permissible resistance value, dust absorption coefficient k_m in tested filter materials assumes various values. The lowest value was obtained for the cartridge D – k_{mD} = 102 g/m^2, and the highest for cartridge k_{mA} = 210 g/m^2, which is related to different material separation properties.

Forecasting vehicle mileage

Forecasting the distance traveled by the car depending on one of the parameters appearing in eq. (7) is possible while establishing the remaining parameters at a constant level. The equation (7) shows that the parameters that determine the value of the distance travelled are: filter surface A_c of the cartridge and dust concentration s in the air sucked in by the filter, which is a variable value, the filter paper absorption coefficient k_m, which depends on the type of paper used. Separation efficiency of modern filter papers can be assumed constant at the minimum level of 99.5%. As a rule, the nominal air demand of the engine is taken as the maximum Q_{Silmax}.

Figure 14 shows an example of mileage changes calculation until the permissible resistance depending on the dust concentration in the air of two passenger cars Audi 80 B2 1.6 GLE and VW Golf II with naturally aspirated engines of the cubic capacity V_{ss} = 1.558 dm^3 but with different power and area filter paper surface. The analysis was performed in the range of air dust concentration s = 0.0004–0.1 g/m^3, which may occur on motorways [2] and assuming the filter paper absorption coefficient k_m = 220 g/m^2.

As dust concentration in the air increases, the car mileage until reaching the permissible resistance decreases, while the car mileage with an Audi engine are five times shorter, which is because of the active surface of the A_c filter paper (by over 50%) smaller than that of the VW car filter and thus dust absorption. The smaller surface of the filter paper means not only high separation speed and increased pressure drop, but also shorter car mileage with an efficient air filter. Audi engine air filter with the surface of the filter paper A_c = 0.708 m^2 and absorbency k_m = 220 g/m^2 is able to retain dust until the permissible resistance of 156 g. A VW car engine air filter with a filter paper area of A_c = 1.63 m^2 will retain 359 g of dust.

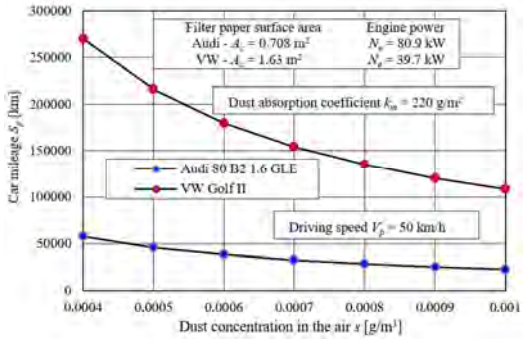

Fig. 14. Vehicle mileage until the filter reaches the permissible resistance depending on dust concentration in the air and different filter paper surfaces from two different filters

After the filter insert reaches permissible resistance, the cartridge should be replaced with a new one. In passenger cars, this operation is performed after a specified mileage set by the car manufacturer (Table 2).

When selecting the filter material for the air filter, its absorbency is also important. Fig. 11 shows an example of mileage calculation changes until the permissible resistance depending on dust concentration in the air is reached for passenger cars Audi 80 B2 1.6 GLE VW Golf II with different values of the filter material absorption coefficient, respectively: k_{m1} = 220 g/m^2, k_{m2} = 135 g/m^2, k_{m3} = 102 g/m^2.

Table 2. Car mileage to replace the filter insert

No.	Car	Type of filter insert	Car mileage to replace the filter insert S_w [km]
1	Skoda Octavia 1.6	panel	60 000
2	Honda Civic	panel	40 000
3	Ford Fiesta	panel	40 000
4	Citroen ZX	panel	30 000
5	Land Rover Defender	panel	20 000
6	Opel Corsa	panel	10 000

Graphs in Fig. 15 show that the use of filter materials with lower absorbency shortens the distance traveled by the car until permissible resistance by the filter is reached, and thus the insert is replaced with a new one. In the case of air filters having a smaller surface of the filter paper than that resulting from the correct selection, this phenomenon increases.

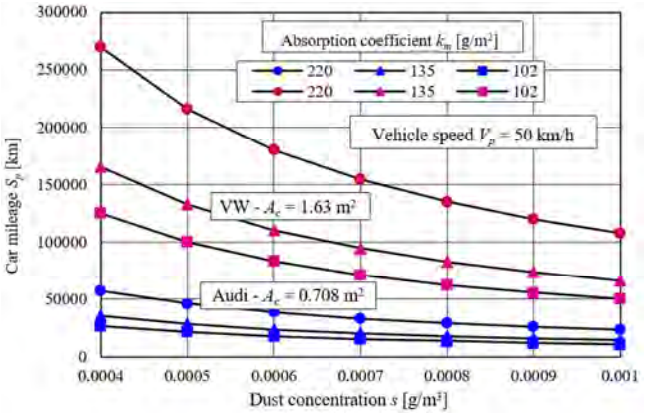

Fig. 15. Vehicle mileage until the filter reaches the permissible resistance depending on air dust concentration and various dust absorption coefficients of the filter material

3. Summary

The aim of this thesis was to experimentally verify the basic criterion (permissible separation speed υ_{Fmax}) for the separation surface selection of a pleated insert for a passenger car engine air filter. Geometry of 44 pleated filter inserts used in passenger car engine air filters, differing in cubic capacity, power, and degree of filling, was analyzed, and then the actual filter paper area of each air filter was determined. Using the theoretical dependence, the nominal air stream flowing through the filter was calculated, and then the separation speed for the analyzed filter inserts was calculated, which was compared with the permissible value

of υ_{Fmax} applicable in the automotive industry. In the second stage, the influence of paper surface and other factors determining the value of the distance traveled by a passenger car until the filter obtained a permissible pressure drop was analyzed. For this purpose, the theoretical dependence was used, which takes into account many experimentally determined factors, which makes the forecast more reliable. The theoretical and experimental analysis shows that:

1. in most cases, the actual (active) inserts filtering surface A_R is greater than the calculated surface A_N from the condition of the permissible separation velocity υ_{Fmax} = 0.12 m/s. This indicates the correct selection of filter surface and air filters for the vehicle.
2. In most cases (62%) of analyzed filter inserts, calculated separation speeds are within the permissible speed range recommended by the designers υ_{Fmax} = 0.06–0.12 m/s.
3. Exceeding the maximum permissible separation speed υ_{Fmax} = 0.12 m/s was seen mainly in filter elements of supercharged and high-power engines. It follows that an important factor determining the surface of the filter paper, and then separation speed, is the free space around the engine where it is possible to place the air filter with filter paper of required surface. The analysis shows that this free space is missing in cars where high-power engines are installed.
4. Active insert filtering surface A_c determines not only the separation speed, but also the value of the distance travelled until the permissible filter resistance is reached, and thus the replacement of the filter cartridge.
5. When selecting a filter material for a car engine air filter, it should be known that modern filter materials used in the production of engine filter elements are more efficient and accurate than conventional cellulose-based materials, but dust absorption is lower by half. It has very big importance when forecasting vehicle mileage, because for the same paper surface, the absorptive capacity of the insert and the vehicle mileage are proportionally lower.

It is possible to run the engine with an air filter with a smaller filter material surface area. Separation process then takes place at a higher speed, which causes a decrease in separation efficiency and increased pressure drop. Along with dust accumulation in filter bed, the process of pressure drop increases. This has negative effects in the form of engine energy losses. A much higher than the permissible flow resistance may cause paper insert destruction, and then contaminants flow into the engine cylinders, causing accelerated abrasive wear of the mating surfaces, clearances enlargement, decreased tightness of the "piston-cylinder" connection and a decrease in engine power.

Acknowledgements

This work was financed by Military University of Technology under research project UGB 881/2021.

Nomenclature

A_c	cartridge active filtering area
CFD	computational fluid dynamics
d_{zmax}	maximum dust grains size after the filter
EGR	Exhaust Gas Recirculation
k_m	filter paper absorbency coefficient
P-P-C	piston–piston rings–cylinder walls
q	air filter quality factor
Q_{Silmax}	maximum air requirement for the engine
Q_w	air stream flowing through the filter element
SI	spark ignition
TDI	Turbo Direct Injection
Δp_{fdop}	air filter permissible resistance
φ_w	cartridge separation efficiency
υ_{Fmax}	maximum separation speed
υ_{FR}	actual separation speed

Bibliography

[1] ALLAM, S., ELSAID, A.M. Parametric study on vehicle fuel economy and optimization criteria of the pleated air filter designs to improve the performance of an I.C diesel engine: experimental and CFD approaches. *Separation and Purification Technology*. 2020, **241**, 116680. https://doi.org/10.1016/j.seppur.2020.116680

[2] BARBOLINI, M., DI PAULI, F., TRAINA, M. Simulation der Luftfiltration zur Auslegung von Filterelementen. *MTZ-Motortechnische Zeitschrift*. 2014, **75**(11), 52-57.

[3] BARRIS, M.A. Total Filtration^{TM}. The influence of filter selection on engine wear. Emissions and performance. *SAE Technical Paper* 952557. 1995. https://doi.org/10.4271/952557

[4] BOJDO, N., FILIPPONE, A. Effect of desert particulate composition on helicopter engine degradation rate. *40th European Rotorcraft Forum*. Southampton. 2014. https://doi.org/10.13140/2.1.2959.8086

[5] BRAUN, R., SAUTER, H., SEGGERN, J. et al. Motorluftfiltration. *MTZ-Motortechnische Zeitschrift.* 2006, **67**(12), 974-980. https://doi.org/10.1007/bf03225436

[6] BUGLI, N.J., GREEN, G.S. Performance and benefits of zero maintenance air induction systems. *SAE Technical Paper* 2005-01-1139. 2005. https://doi.org/10.4271/2005-01-1139

[7] CHEN, D.R., PUI, D.Y.H., LIU, B.Y.H. Optimization of pleated filter designs using a finite-element numerical model. *Aerosol Science and Technology*. 1995, **23**(4), 579-590. https://doi.org/10.1080/02786829508965339

[8] CHEN, C.W., HUANG, S.H., CHIANG, C.M. et al. Filter quality of pleated filter cartridges. *Annals of Occupational Hygiene*. 2008, **52**(3), 207-212. https://doi.org/10.1093/annhyg/men008

[9] DAHLAN, A.A., MUHAMMAD SAID M.F., ABDUL LATIFF, Z. et al. Acoustic study of an air intake system of SI engine using 1-dimensional approach. *International Journal of Automotive and Mechanical Engineering* (IJAME). 2019, **16**(1), 6281-6300. https://doi.org/10.15282/ijame.16.1.2019.14.0476

[10] DEL FABBRO, L., LABORDE, J.C., MERLIN, P. et al. Air flows and pressure drop modelling for different pleated industrial filters. *Filtration & Separation*. 2002, **39**(1), 35-40. https://doi.org/10.1016/S0015-1882(02)80055-6

[11] DURST, M., KLEIN, G., MOSER, N. Filtration in Fahrzeugen. *Mann+Hummel GMBH*. Ludwigsburg 2005.

[12] DZIUBAK, T., DZIUBAK, S.D. Experimental study of filtration materials used in the car air intake. *Materials*. 2020, **13**(16), 3498. https://doi.org/10.3390/ma13163498

[13] DZIUBAK, T., BĄKAŁA, L. Experimental research of the material filtration characteristics with nanofibers addition. *Journal of KONES Powertrain and Transport*. 2018, **25**(4), 83-94. https://doi.org/10.5604/01.3001.0012.4779

[14] DZIUBAK, T., SZWEDKOWICZ, S. Operating properties of non-woven fabric panel filters for internal combustion engine inlet air in single and two-stage filtration systems. *Eksploatacja i Niezawodność – Maintenance and Reliability*. 2015, **17**(4), 519-527. https://doi.org/10.17531/ein.2015.4.6

[15] Engine air cleaners, service parts and accessories. https://www.donaldson.com/content/dam/donaldson/engine-hydraulics-bulk/catalogs/air-intake/emea/f116005/Air-Intake-Product-Guide.pdf

[16] ERDMANNSDÖRFER, H. Lesttingmoglichkeiten von Papierfiltern zur Reinigung der Ansaugluft von Diselmotoren. *MTZ-Motortechnische Zeitschrift*. 1971, **32**, 123-131.

[17] FENG, Z., LONG, Z. Modeling unsteady filtration performance of pleated filter. *Aerosol Science and Technology*. 2016, **50**(6), 626-637. https://doi.org/10.1080/02786826.2016.1172058

[18] FLECK, S., HEIM, M., BECK, A. et al. Realitätsnahe Prüfung von Motoransaugluftfiltern, *MTZ-Motortechnische Zeitschrift*. 2009, **70**, 414-418. https://doi.org/10.1007/BF03225494

[19] FOTOVATI, S., HOSSEINI, S., TAFRESHI, H. et al. Modeling instantaneous pressure drop of pleated thin filter media during dust loading, *Chemical Engineering Science*. 2011, **66**(18), 4036-4046. https://doi.org/10.1016/j.ces.2011.05.038

[20] FOTOVATI, S., TAFRESHI, H.V., POURDEYHIMI, B. A macroscopic model for simulating pressure drop and collection efficiency of pleated filters over time. *Separation and Purification Technology*. 2012, **98**, 344-355. https://doi.org/10.1016/j.seppur.2012.07.009

[21] GERVAIS, P.C., POUSSIER, S., BARDIN-MONNIER, N. et al. Combination of single-photon emission and X-Ray computed tomography to visualize aerosol deposition in pleated filter. *Separation and Purification Technology*. 2014, **126**, 52-61. https://doi.org/10.1016/j.seppur.2014.02.011

[22] HALIM, M.A.A., MOHD, N.A.R., NASIR, M.N.M. et al. Experimental and numerical analysis of a motorcycle air intake system aerodynamics and performance. *International Journal of Automotive and Mechanical Engineering* (IJAME). 2020, **17**(1), 7607-7617. https://doi.org/10.15282/ijame

[23] JAROSZCZYK, T., FALLON, S.L., LIU, Z.G. et al. Development of a method to measure engine air cleaner fractional efficiency. *SAE Technical Paper* 1999-01-0002. 1999. https://doi.org/10.4271/1999-01-0002

[24] JIN-RUI, X., FU-PING, Q., JIN-LI, L. et al. Three-dimensional microstructure reconstruction of pleated air filter media and simulation of its performance in dust filtration stage. *Chinese Journal of Process Engineering*. 2017, **17**(1) 170-177. https://doi.org/10.12034/j.issn.1009-606X.216190

[25] KAHRSTEDT, J., ZÜLCH, S., STRENG, CH. et al. Neue Generation des 3.0-L-Tdi-Motors von Audi. *MTZ-Motortechnische Zeitschrift.* 2010, **11**(71), 800-807. https://doi.org/10.1007/BF03225625

[26] KANG, S., BOCK, N., SWANSON, J. et al. Characterization of pleated filter media using particle image velocimetry. *Separation and Purification Technology*. 2020, **237**, 116333. 116333. https://doi.org/10.1016/j.seppur.2019.116333

[27] LI, S., HU, S., XIE, B. et al. Influence of pleat geometry on the filtration and cleaning characteristics of filter media. *Separation and Purification Technology*. 2019, **210**, 38-47. https://doi.org/10.1016/j.seppur.2018.05.002

[28] LONG, J., TANG, M., SUN, Z. et al. Dust loading performance of a novel submicro-fiber composite filter medium for engine. *Materials*. 2018, **11**, 2038. https://doi.org/10.3390/ma11102038.

[29] MAHESH, J. Parametric study and CFD analysis of air filter. *Asian Journal of Convergence in Technology* (AJCT). 2019, **5**(1), 1-9. www.asianssr.org

[30] MADDINENI, A.K., DAS, D, DAMODARAN, R.M. Experimental and numerical study on automotive pleated air filters. *SAE Technical Paper* 2016-28-0100. 2016. https://doi.org/10.4271/2016-28-0100

[31] MADDINENI, A.K., DAS, D., DAMODARAN, R.M. Airborne particle by fibrous filter media under collision effect: a CFD-based approach. *Separation and Purification Technology*. 2018, **193**, 1-10. https://doi.org/10.1016/j.seppur.2017.10.065

[32] MADDINENI, A.K., DAS, D., DAMODARAN, R.M. Numerical investigation of pressure and flow characteristics of pleated air filter system for automotive engine intake application. *Separation and Purification Technology*. 2019, **212**, 126-134. https://doi.org/10.1016/j.seppur.2018.11.014

[33] MADDINENI, A.K., DAS, D., DAMODARAN, R.M. Oil-treated pleated fibrous air filters for motor vehicle engine intake application. *Proceedings of the Institution of Mechanical Engineers, Part D: Journal of Automobile Engineering*, 2019, **234**(2-3), 702-713. https://doi.org/10.1177/0954407019850379

[34] MELZER, H.H., BROX, W. Ansauggerauschdampfer und Luftfilter für BMW 524 td, *MTZ-Motortechnische Zeitschrift*. 1984, **45**, 223-227.

[35] KWON, M-S., KIM Y-L., KIM, M-S. et al. Effect of pleating ratio on quality factor of pleated filter in air purifier. *Journal of Korean Society for Atmospheric Environment*. 2020, **36**(1), 119-127. https://doi.org/10.5572/KOSAE.2020.36.1.119

[36] MUSTAFA, N.S., NGADIMAN, N.H.A., ABAS, M.A. et al. Application of box-behnken analysis on the optimisation of air intake system for a naturally aspirated engine. *International Journal of Automotive and Mechanical Engineering* (IJAME). 2020, **17**(2), 7607-7617. https://doi.org/10.15282/ijame.17.2.2020.21.0602

[37] NORMAN, K., HUFF, S., WEST, B. Effect of intake air filter condition on vehicle fuel economy. *U.S. Department of Energy (DOE) Information Bridge*. 2009. http://www.osti.gov/bridge

[38] PARK, B., LEE, M., JO, Y. et al. Influence of pleat geometry on filter cleaning in a PTFE/glass composite filter. *Journal of the Air & Waste Management Association*. 2012, **62**, 1257-1263. https://doi.org/10.1080/10962247.2012.696530

[39] PN-S-34040, Filtry powietrza. Wymagania i badania, *PKN* 1996.

[40] REBAI, M., PRAT, M., MEIRELES, M. et al. A semi-analytical model for gas flow in pleated filters. *Chemical Engineering Science*. 2010, **65**, 2835-2846. https://doi.org/10.1016/j.ces.2010.01.014

[41] REBAI, M., PRAT, M., MEIRELES, M. et al. Clogging modeling in pleated filters for gas filtration. *Chemical Engineering Research and Design*. 2010, **88**, 476-486. https://doi.org/10.1016/j.cherd.2009.08.014

[42] SAKTHIVEL, S., EHZIL ANBAN, J.J., RAMACHANDRAN, T. Development of needle-punched nonwoven fab-

rics from reclaimed fibers for air filtration applications. *Journal of Engineered Fibers and Fabrics*. 2014, **9**, 149-154. https://doi.org/10.1177/155892501400900117

[43] SALEH, A., TAFRESHI, H. A simple semi-numerical model for designing pleated air filters under dust loading. *Separation and Purification Technology*. 2014, **137**, 94-108. https://doi.org/10.1016/j.seppur.2014.09.029

[44] SALEH, A.M., HOSSEINI, S.A., TAFRESHI, H.V. et al. 3-D microscale simulation of dust-loading in thin flat-sheet filters: a comparison with 1-D macroscale simulations. *Chemical Engineering Science.* 2013, **99**, 284-291. https://doi.org/10.1016/j.ces.2013.06.007

[45] SALEH, A.M., FOTOVATI, S., TAFRESHI, H.V. et al. Modeling service life of pleated filters exposed to poly-dispersed aerosols. *Powder Technology*. 2014, **266**, 79-89. https://doi.org/10.1016/j.powtec.2014.06.011

[46] SALEH, A.M., TAFRESHI, H.V., POURDEYHIMI, B. Service life of circular pleated filters vs. that of their flat counterpart. *Separation and Purification Technology*. 2015, **156**, 881-888. https://doi.org/10.1016/j.seppur.2015.09.041

[47] SAWANT, P., BARI, S. Effects of variable intake valve timings and valve lift on the performance and fuel efficiency of an internal combustion engine. *SAE Technical Paper* 2018-01-0376. 2018. https://doi.org/10.4271/2018-01-0376

[48] SMIALEK, J.L., ARCHER, F.A., GARLICK, R.G. Turbine airfoil degradation in the persian gulf war. *The Journal of The Minerals, Metals & Materials Society* (TMS). 1994, **46**(12), 39-41. https://doi.org/10.1007/BF03222663

[49] SUBRENAT, A., BELLETRE, J., LE CLOIREC, P. 3-D numerical simulations of flows in a cylindrical pleated filter packed with activated carbon cloth. *Chemical Engineering Science*. 2003, **58**, 4965-4973. https://doi.org/10.1016/j.ces.2003.07.012

[50] TANG, R-J., HU, B-F., ZHANG, M. et al. Study on separation characteristics of dust and droplet on air intake pre-filtration systems of CV based on CFD simulation and test. *International Conference on Artificial Intelligence and Computing Science* (ICAICS 2019). https://doi.org/10.12783/dtcse/ icaic2019/29462

[51] TAUFKIRCH, G., MAYR, G. Papierluftfilter für Motoren in Nutzfahrzeugen. *MTZ-Motortechnische Zeitschrift*. 1984, **45**(3), 95-105.

[52] THÉRON, F., JOUBERT, A., COQ, L. Numerical and experimental investigations of the influence of the pleat geometry on the pressure drop and velocity field of a pleated fibrous filter. *Separation and Purification Technology*. 2017, **182**, 69-77. https://doi.org/10.1016/j.seppur.2017.02.034

[53] TRONVILLE, P., SALA, R. Minimization of resistance in pleated-media air filter designs: empirical and CFD approaches. *HVAC&R Research*. 2003, **9**, 95-106. https://doi.org/10.1080/10789669.2003.10391058

[54] WIEGMANN, A., RIEF, S., KEHRWALD, D. Computational study of pressure drop dependence on pleat shape and filter media. *Filtech 2007 International Conference for Filtration and Separation Technology* 2007, **1**, 79-86. http://publica.fraunhofer.de/documents/N-470488.html

[55] WRÓBLEWSKI, P., KOSZAŁKA, G. An experimental study on frictional losses of coated piston rings with symmetric and asymmetric geometry. *SAE International Journal of Engines*. 2021, **14**(6). https://doi.org/10.4271/03-14-06-0051

[56] WRÓBLEWSKI, P. Technology for obtaining asymmetries of stereometric shapes of the sealing rings sliding surfaces for selected anti-wear coatings. *SAE Technical Paper* 2020-01-2229. 2020. https://doi.org/10.4271/2020-01-2229

[57] VOGEL, A., DURANT, A.J., CASSIANI, M. et al. Simulation of volcanic ash ingestion into a large aero engine: particle–fan interactions. *ASME Journal of Turbomachinery*. 2019, **141**(1), 011010. https://doi.org/10.1038/srep25620

[58] www.retopfibre.en.alibaba

Tadeusz Dziubak, DSc., DEng. – Faculty of Mechanical Engineering, Military University of Technology, Warsaw, Poland.

e-mail: *tadeusz.dziubak@wat.edu.pl*

Leszek Bąkała MEng., Ph.D. student – Faculty of Mechanical Engineering, Military University of Technology, Warsaw, Poland.

e-mail: *leszekbakala@gmail.com*

Division of Automotive Engineering

Polish Scientific Society of Combustion Engines

Institute of Combustion Engines and Powertrains

V Young Scientists Academy

www.ptnss.pl

15-17 November 2021

Czocha Castle, Sucha, 59-820 Leśna; zamekczocha.com

IX INTERNATIONAL CONGRESS ON COMBUSTION ENGINES

POLISH SCIENTIFIC SOCIETY OF COMBUSTION ENGINES

27th-28th September 2021

Photo courtesy of the Lublin City

Lublin University of Technology
Faculty of Mechanical Engineering
Nadbystrzycka 36, 20-618 Lublin, Poland

IX INTERNATIONAL CONGRESS ON COMBUSTION ENGINES

POLISH SCIENTIFIC SOCIETY OF COMBUSTION ENGINES

congress.ptnss.pl

27th-28th September 2021

The Polish Scientific Society of Combustion Engines and the Mechanical Engineering Faculty of the Lublin University of Technology cordially invite engineers and researchers to the 9th International Congress on Combustion Engines that will be held on September 27-28, 2021 in Lublin, Poland. This biennial event is a forum for the exchange of experiences between experts from science and industry, promoting and supporting the development of ICE science and engineering. The aim of the event is to present the latest achievements and state of the art in ICEs, also in a holistic and interdisciplinary context. Special attention will be given to new research results creating global trends that are important from the applicability perspective.

The Congress will host presentations and an exhibition, being a source of information and ensuring the dissemination of technical achievements and ideas related to ICEs. More and more frequently we observe that interdisciplinary teams, cooperating in various areas, participate in research works. Therefore, we invite participants not only from the field of ICE but also from related fields to share their experience and knowledge.

We encourage the ICE community to actively participate in thematic, interactive, problem and interdisciplinary sessions, and to attend meetings with experts and exhibitors. Participants will have an excellent opportunity to meet engineers and researchers from around the world and discuss current trends in the engine technology, share innovative ideas and promote collaboration.

CONGRESS TOPICS

- New engines and engine components
- Hybrid and electric powertrains
- Engine combustion
- Engine testing and modelling
- Fuels and lubricants
- Exhaust emissions and aftertreatment
- Sustainability and global trends in powertrain technology

RESEARCH PAPERS

- All papers after positive review will be published in **Combustion Engines** journal (MEiN: 20 pts).
- Top 10 papers will be recommended for publication in a Congress special issue of the **International Journal of Engine Research** (IF: 2.382, MEiN: 100 pts).
- There is also possibility to publish a paper in a special issue Energy Transfer in Alternative Vehicles of the journal **Energies** (MDPI) with 20% discount (IF: 2.702, MEiN: 140 pts).

Lublin University of Technology
Faculty of Mechanical Engineering
Nadbystrzycka 36, 20-618 Lublin, Poland

Publisher:

Polish Scientific Society of Combustion Engines

ISSN: 2300-9896
eISSN: 2658-1442

Combustion Engines

Polskie Towarzystwo Naukowe Silników Spalinowych

www.combustion-engines.eu